

学位論文

Search for Sub-GeV WIMP dark
matter by annual modulation using
XMASS-I detector

(XMASS-I検出器を用いたSub-GeV
暗黒物質に由来する季節変動の探索)

平成29年12月博士(理学)申請

東京大学理学系研究科

物理学専攻

小林 雅俊

Abstract

According to recent observations, it is revealed that the fraction occupied by ordinary matter such as hydrogen or helium is only about 5% of the energy density of our universe. About 25% of remaining energy densities is considered to belong to unidentified matter, called dark matter. Weakly Interactive Massive Particles (WIMPs) are able to explain the observational results. Targets of this thesis is to search for Sub-GeV WIMPs by annual modulation caused by bremsstrahlung photon emission using XMASS-I detector. The XMASS-I detector is a large and low radioactive background detector using 832 kg of liquid xenon in its sensitive volume. It has been operating more than 3 years (2.38 ton year exposure). In addition to this, lower threshold data has been taken more than 1 year (0.63 ton year exposure). A search for Sub-GeV WIMPs was conducted with an energy threshold 1 keVee and 24% of signal efficiency for 0.5 GeV WIMPs. As a result, no significant signal is observed and a 90% confidence level upper limit on the cross section between WIMPs and nucleon at $1.6 \times 10^{-33} \text{ cm}^2$ at 0.5 GeV is obtained. Similar searches for annual modulation directly caused by nuclear recoil with Multi-GeV WIMPs and other particles give upper limits on modulation signal. This is the first experimental search for Sub-GeV WIMPs exploiting annual modulation and bremsstrahlung in a liquid xenon detector.

Acknowledgements

First of all, I would like to express my gratitude to my supervisor, Prof. Shigetaka Moriyama for guiding me and giving a lot of advises throughout my graduate course. I would also like to express my gratitude to M. Yamashita, K. Hiraide and B. Yang for kindly supporting me about modulation analysis and bremsstrahlung analysis. I would also like to express my gratitude to the previous and current member of XMASS collaboration who worked with me, Prof. Y. Suzuki, Prof. M. Nakahata, Prof. Y. Kishimoto, Prof. H. Sekiya, K. Abe, K. Ichimura, Kazuyoshi Kobayashi, H. Ogawa, K. Sato, A. Takeda, O. Takachio, K. Nakagawa, T. Norita, Prof. K. Martens, J. liu, B. Xu, M. Alexander, Prof. S. Tasaka, Prof. Y. Itow, H. Uchida, H. Takiya, Koichi Kobayashi, R. Kegasa, K. Kanzawa, K. Masuda, Prof. Y. Takeuchi, Prof. K. Miuchi, K. Hosokawa, N. Oka, Y. Onishi, R. Fujita, Prof. Y. D. Kim, Y. H. Kim, N. Y. Kim, K. B. Lee, M. K. Lee, Prof. Y. Fukuda, Prof. K. Nishijima, M. Miyasaka, Prof. K. Fushimi, G. Kanzaki, and Prof. S. Nakamura. I would like to thank to the member of Kamioka observatory, Y. Nakano, A. Orii, Y. Okajima, R. Akutsu, Y. Sonoda, and A. Takenaka and all other people who supported me during my graduate course. Finally, I would like to express my gratitude to my friends and family.

Contents

1	Introduction	10
1.1	Observational evidence of Dark Matter	10
1.1.1	Velocity dispersion and luminosity in cluster	10
1.1.2	Rotation curves of galaxies	11
1.1.3	Gravitational lensing effect	12
1.1.4	The Bullet cluster	13
1.1.5	Cosmic Microwave Background	14
1.1.6	N-body simulation for large scale structure of the uni- verse	15
1.2	Candidates of dark matter	16
1.2.1	MACHOs	17
1.2.2	Neutrinos	17
1.2.3	axions	17
1.2.4	WIMPs	18
1.3	Detection of dark matter	18
1.3.1	Interaction between the dark matter particle and nuclei	19
1.3.2	Direct detection of dark matter	19
1.3.3	Other types of detection	21
1.3.4	Accelerator detection	21
1.3.5	Indirect detection	21
1.4	Current situation of direct dark matter search	22
2	Dark matter search by annual modulation of event rate	24
2.1	Kinematics of elastic scattering between dark matter and nucleus	24
2.1.1	Energy spectrum of nuclear recoil	24
2.1.2	Nuclear bremsstrahlung caused by sub-GeV WIMP . .	26
2.2	Annual modulation of the event rate of nuclear recoil	30
2.3	Experimental detection of annual modulation	32

2.3.1	DAMA/LIBRA	34
2.3.2	XENON100	35
2.3.3	XMASS	35
2.4	Physics targets based on annual modulation search in this thesis	36
2.4.1	Sub-GeV WIMPs search by annual modulation of nuclear bremsstrahlung	36
2.4.2	Enhancement of sensitivity for nuclear recoil by lowering the energy threshold	40
3	XMASS experiment	41
3.1	Purpose of the experiment	41
3.2	XMASS-I detector	41
3.2.1	Liquid xenon	43
3.2.2	Inner Detector	46
3.2.3	Outer detector	46
3.2.4	DAQ system	47
3.3	Calibration system	50
3.3.1	Inner calibration system	50
3.3.2	Calibration source	50
3.4	Simulation	51
3.4.1	Al seal modeling	52
3.4.2	Scintillation yield of LXe	53
4	Developments toward high sensitivity	57
4.1	Key ingredients to achieve high sensitivity	57
4.2	Modification of electronics toward lower mass WIMP search .	57
4.3	Identification of noise events in the low threshold data	59
4.3.1	Weak flashing of PMTs	59
4.3.2	Properties of flasher events and event selection	60
4.4	Energy scale calibration at low energy	61
5	Data set and reduction	65
5.1	Summary of the data set	65
5.2	Run selection and binning	65
5.2.1	Run selection for the normal threshold runs	65
5.2.2	Run selection for the low threshold runs	66
5.2.3	Time binning	66
5.2.4	Energy binning	67

5.3	Data reduction	70
5.3.1	Noise cut	70
5.3.2	Afterpulse cut	70
5.3.3	flasher cut	71
5.3.4	cherenkov cut	71
5.3.5	likelihood cut	72
6	Systematic errors and error estimation	76
6.1	Systematic errors in the real data analysis	76
6.1.1	Stability of Light Yield of the detector	76
6.1.2	Stability of Electronics	84
6.1.3	Event rate fluctuation caused by weak flashing of PMTs	84
6.1.4	Internal gain instability of FADC	89
6.2	Systematic errors in evaluation of expected signal	91
6.2.1	Nuclear recoil energy spectrum of WIMPs	91
6.2.2	Bremsstrahlung photons energy spectrum	91
6.3	Other Systematic errors	91
6.3.1	Muon induced events	91
6.3.2	Rn in the water tank	93
7	Analysis method for annual modulation	95
7.1	Minimum χ^2 fitting	95
7.1.1	Definition of χ^2	95
7.2	Expected event rate	96
7.2.1	Bremsstrahlung and Nuclear recoil of standard WIMPs	96
7.2.2	Model independent analysis	97
7.3	Sensitivity estimation	97
7.3.1	Generation of the dummy sample	97
7.3.2	Calculation of sensitivity for the case of bremsstrahlung and nuclear recoil of WIMPs	98
7.3.3	Demonstration of analysis using sample with signifi- cant amplitude	100
8	Result of modulation analysis	102
8.1	Result of the sub-GeV WIMP search	102
8.2	Result of the light WIMP search	107
8.3	Result of the Model-independent modulation search	109

8.3.1	Comparison with the result of WIMP analysis and model independent analysis	110
9	Conclusion	116
9.1	Summary of the results of the WIMPs search	116
9.2	Discussion for future analysis	118

List of Figures

1.1	Structures of spiral galaxies	11
1.2	Observed rotational speed of the spiral galaxy	12
1.3	Observation of the gravitational lensing effect.	13
1.4	Bullet cluster 1e657	14
1.5	Distribution of the temperature fluctuation in universe	15
1.6	Power spectrum obtained by the temperature fluctuation . . .	16
1.7	Current constraints for WIMP-nucleon cross section and its mass.	23
2.1	Energy spectrum of nuclear recoil caused by WIMPs	27
2.2	Atomic scattering factor f of a xenon atom	30
2.3	Energy spectrum of emitted photons from nuclear bremsstrahlung for mass of 0.5 and 1.0 GeV WIMPs	31
2.4	Annual energy spectrum A_0 for 10 GeV WIMPs	33
2.5	Modulation part, A_{annual} for 10 GeV WIMPs	33
2.6	Time valuation of event rate for 10 GeV WIMPs at 1-2keV . .	34
2.7	Observation by DAMA/LIBRA experiment	35
2.8	Observation by XENON100 experiment	36
2.9	Observation by XMASS experiment, for WIMP result	37
2.10	Observation by XMASS experiment, for Model independent result	38
2.11	Energy spectra of bremsstrahlung for 1 GeV WIMPs	38
2.12	Difference between the blue and red curves in Fig. 2.11	39
2.13	Time variation of event rate of bremsstrahlung photon for 1 GeV WIMPs at 1-2 keV	39
2.14	Expected sensitivity using low threshold data	40
3.1	The whole view of the XMASS-I detector	42
3.2	LXe scintillation decay time constant	45

3.3	Inner detector	47
3.4	Simplified trigger flow of the XMASS-I detector	49
3.5	FADC V1751	50
3.6	Calibration system of XMASS detector	51
3.7	4π (needle) calibration source	51
3.8	2π (flat) calibration source	52
3.9	Geometry of XMASS-I detector simulation	53
3.10	The photos around Al seal for one PMT	54
3.11	Two models of a gap around the Al seal of PMT	54
3.12	Energy spectrum caused by the RIs in the bulk of the Al seal	55
3.13	Leff measurement above 3 keVnr	56
3.14	Leff measurement by the LUX group including points below 3 keVnr	56
4.1	Low threshold trigger flow	58
4.2	A schematic view of the timing delay of low threshold trigger for the HITSUM waveform	59
4.3	Schematic view of PMT flashing	60
4.4	Time and angle distribution	61
4.5	PE distribution for the escape peak	63
4.6	Comparison between data and MC for each calibration point	63
4.7	Comparison between data and MC for each calibration source with correction	64
5.1	(a):Livetime, (b): single rate of total detector, (c): number of PMTs with single rate more than 100 Hz, (d): the single rate of typical unstable PMTs, and (e): the single rate of typical stable yPMTs.	68
5.2	Year and month for each period	69
5.3	The non-linear energy conversion function	70
5.4	Dt and trms distribution observed in a dark matter run	71
5.5	Probability density function of Sphericity, Aplanarity and Max-to-total ratio parameters around 2 keVee	73
5.6	Log likelihood distribution for uniform electron MC	74
5.7	Energy spectrum of the data	75
6.1	Number of PE spectrum of the ^{57}Co source	77
6.2	Change of light yield of 122 keV γ rays	78

6.3	Optical parameters obtained through a fitting with MC samples	80
6.4	Relative efficiency curves with their uncertainties	82
6.5	Relative efficiency	83
6.6	Change of relative efficiencies as the function of time with their uncertainties	85
6.7	Distribution of HITSUM baseline during one run	86
6.8	HITSUM mean for each run	87
6.9	Distribution of HITSUM mean	87
6.10	HITSUM height	88
6.11	Relationship between the difference of single rate and differ- ence of three hit event rate before the flasher cut	89
6.12	Relationship between the difference of single rate and differ- ence of three hit event rate after the flasher cut	90
6.13	Impact on the three hit event rate and its systematic errors . .	90
6.14	Expected spectrum from 10 GeV WIMPs	92
6.15	Expected bremsstrahlung spectrum from 0.5 GeV WIMPs . .	93
7.1	Example of Dummy sample	99
7.2	Distribution of the best fit position of cross section for each mass of WIMPs	100
8.1	The result of fit with bremsstrahlung signal of 0.5 GeV WIMPs	103
8.2	The result of fit with bremsstrahlung signal of 0.5 GeV WIMPs	104
8.3	The result of fit with bremsstrahlung signal of 0.5 GeV WIMPs	105
8.4	The result of fit with bremsstrahlung signal of 0.5 GeV WIMPs	106
8.5	90 % C.L. upper limits of data and the sensitivity band for null amplitude utilizing the bremsstrahlung effect	106
8.6	The distribution of $\Delta\chi^2$ for 0.5 GeV WIMPs	107
8.7	90 % upper limits of Data and the sensitivity band for null amplitude utilizing the nuclear recoi.	109
8.8	Distribution of data with correction of efficiency for each en- ergies.	111
8.9	Distribution of data with correction of efficiency for each en- ergies.	112
8.10	Distribution of data with correction of efficiency for each en- ergies.	113
8.11	Distribution of data with correction of efficiency for each en- ergies.	114

8.12	Result of the model independent analysis.	114
8.13	Efficiency curve for signal evaluated by uniform electron MC .	115
8.14	Comparison of the model independent result and bremsstrahlung analysis	115
9.1	Time variation for 0.5 GeV WIMPs	117
9.2	Time variation for 8 GeV WIMPs	118
9.3	Summary of WIMP searches.	119

List of Tables

1.1	Direct dark matter experiment using noble gas.	20
3.1	List of calibration sources for XMASS	52
5.1	Summary of the data set	65
6.1	Summary of the terms for the calculation of flasher effect . . .	89
8.1	Summary of the fit result for bremsstrahlung analysis	108
8.2	Summary of the fit result for nuclear recoil analysis	108

Chapter 1

Introduction

According to recent observations, it is revealed that the fraction occupied by "ordinary" matter such as hydrogen or helium is only about 5% of the energy density of our universe. Approximately 70% of the remaining energy densities belong to the energy of cosmic expansion, and about 25% is considered to belong to unidentified matter, called dark matter. In this chapter we will introduce the history of observation of dark matter, observational evidence, and candidates for dark matter. Experiments trying to discover dark matter particles are also introduced.

1.1 Observational evidence of Dark Matter

1.1.1 Velocity dispersion and luminosity in cluster

The word "dark matter" was used by F. Zwicky for the first time in his article about the observation of missing mass in the Coma cluster [1], [2]. He suggested several methods to evaluate the mass of Coma cluster, such as the light - mass relationship and the virial theorem applied to the motion of galaxies. Then he tried to compare the results of the evaluation on its mass. He found that the mass evaluated based on virial theorem gave about 500 times larger than that evaluated by the light-mass relationship. He named this missing mass "dark matter". Recent observation indicates the difference of the mass evaluated for the Coma cluster is a factor of 50, which is smaller than the Twicky's calculation. However there still exists the missing mass.

1.1.2 Rotation curves of galaxies

Spiral galaxies, for example, the Milky Way, have the structure depicted in Fig. 1.1. The center of a galaxy, called as a bulge, contains the most of the

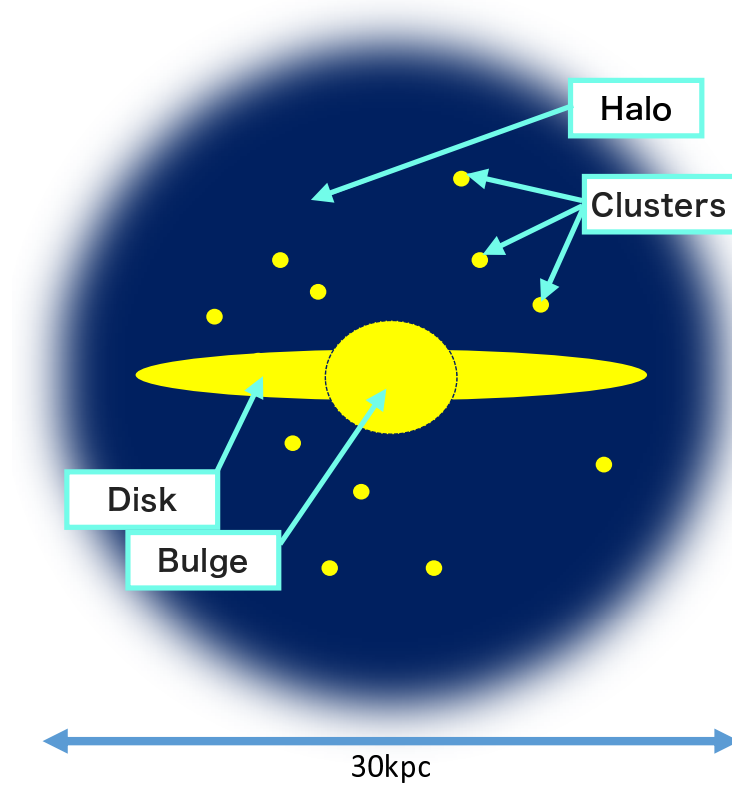


Figure 1.1: Structures of spiral galaxies, such as the Milky Way.

luminous matter. The other parts, a disk has rotational structure of stars and gas. Rotational speed of the disk can be observed by the 21 cm line of neutral hydrogen. The Doppler shift of this line is a good measure of the speed of rotating stars and gas. According to the Newtonian mechanics, the rotational speed is described as

$$\begin{aligned} F = \frac{GMm}{r^2} &= \frac{mv^2}{r} \\ \Longleftrightarrow v &= \sqrt{\frac{GM}{r}}, \end{aligned} \quad (1.1)$$

where G is the gravitational constant, v is the velocity, r is the distance from the center of galaxy, m is the mass of the star, and M is the mass of a galaxy

inside r . Since most of luminous stars are concentrated in the bulge of a galaxy, velocity of the rotational stars in the disk should decrease with the distance r from the center if matter of the spiral galaxy mainly consists of luminous matter. Figure 1.2 [3] shows a rotation curve of a spiral galaxy.

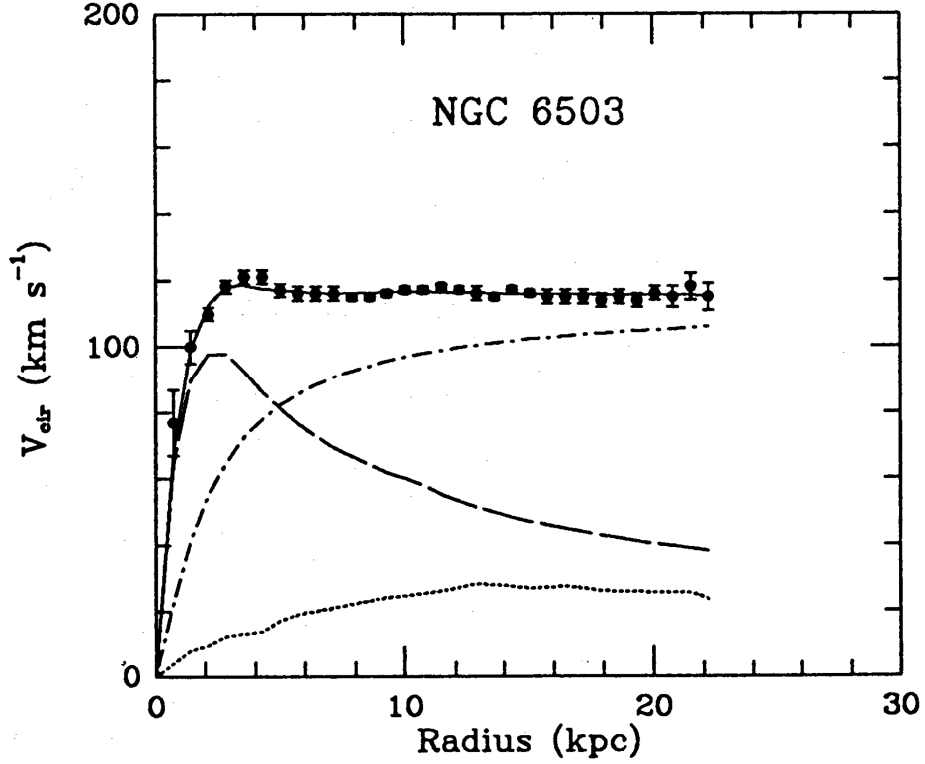


Figure 1.2: Observed rotational speed of a spiral galaxy [3].

This figure shows the fact that the rotation speed of the spiral galaxy is constant at the end of the disk. To explain this rotation curve, much more mass outside the bulge is necessary, but there are no observable luminous matter in the space. This indicates that there is massive matter in addition to luminous matter.

1.1.3 Gravitational lensing effect

Other probe to confirm the presence of dark matter is gravitational lensing effect. Though the nature of dark matter is not yet known, we know that they interact through gravity. Gravitational lensing effect is explained by the general relativity. If there is dark matter between a light source and an

observer, path of the light is bent. In Fig. 1.3, light from galaxies behind the cluster is bent and appears in circular shape [4]. By comparing the mass estimated by kinematics and the mass estimated by light intensity of the clusters, most of galaxies of the clusters have larger mass than that estimated by light.

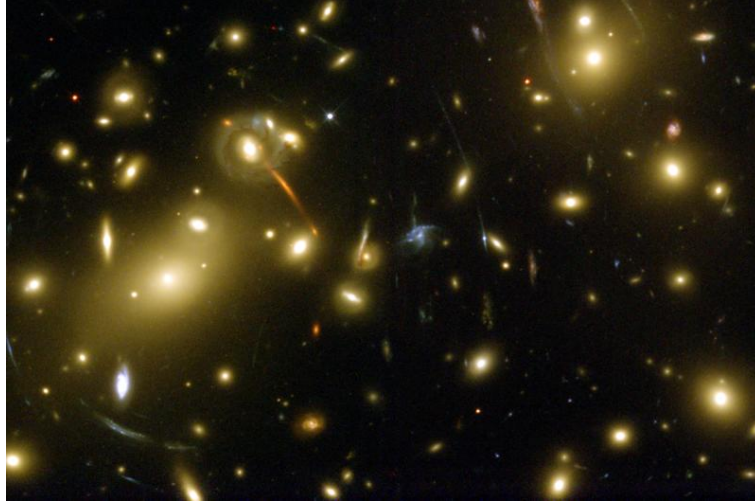


Figure 1.3: Observation of the gravitational lensing effect at Abell2218. Credit: NASA, ESA, Richard Ellis (Caltech) and Jean-Paul Kneib (Observatoire Midi-Pyrenees, France); Acknowledgment: NASA, A. Fruchter and the ERO Team (STScI and ST-ECF)

1.1.4 The Bullet cluster

The Bullet cluster consists of two colliding clusters of galaxies. Figure 1.4 shows the famous example of this type of a cluster, called 1E-0657-56, observed by Chandra observatory using X ray [5]. In Fig. 1.4, hot interstellar gas shown in red clearly shows the structure of the shock wave of the collision. Also, distribution of mass was evaluated by using gravity lensing effect shown in blue in Fig. 1.4. The distribution of mass does not overlap the distribution of gas emitting X rays. It means that observed luminous matter cannot explain the mass of the cluster. This inconsistency of the distribution suggests an important fact. Visible mass interacts strongly, but dominant component of mass does not. This situation can be explained by weakly interacting massive particle (WIMPs) dark matter models.

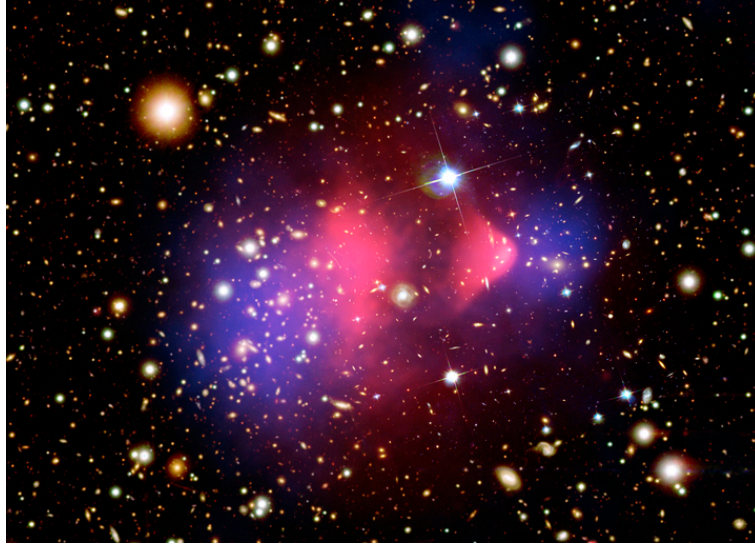


Figure 1.4: Bullet cluster 1E-0657-56, observed by Chandra observatory using X ray [5] (Credit: X-ray: NASA/CXC/CfA/M.Markevitch et al.; Optical: NASA/STScI; Magellan/U.Arizona/D.Clowe et al.; Lensing Map: NASA/STScI; ESO WFI; Magellan/U.Arizona/D.Clowe et al.)

1.1.5 Cosmic Microwave Background

Cosmic microwave background (CMB) has been precisely measured using satellites. Observation by COBE enabled us to map the distribution of temperature fluctuation of the whole universe. This fluctuation of temperature is reflecting the gravitational potential. Before the recombination, photons were interacting with baryons and electrons each other through Thomson scattering. Because of that, variation of energy density of baryon leads to the fluctuation of observed photon. On the other hand, dark matter does not directly interact with photon. But the energy density of the dark matter also affects the fluctuation through the gravitational interaction with baryons. Observational results show the distribution of the spacial distance scale of temperature fluctuation have some peaks. These peaks reflect the fraction of energy density and the flatness of the universe. The first precise measurement by COBE showed that the best fit of the fraction of dark matter was about 30%. It was found that dark matter density is more than five times larger than that of baryon. According to the result of Planck [6], dark matter energy density was found to be 26% of total energy of the universe.

Figure 1.5 and 1.5[6] show the distribution of the temperature fluctuation in universe by the Planck satellite and power spectrum obtained by the temperature fluctuation, respectively.

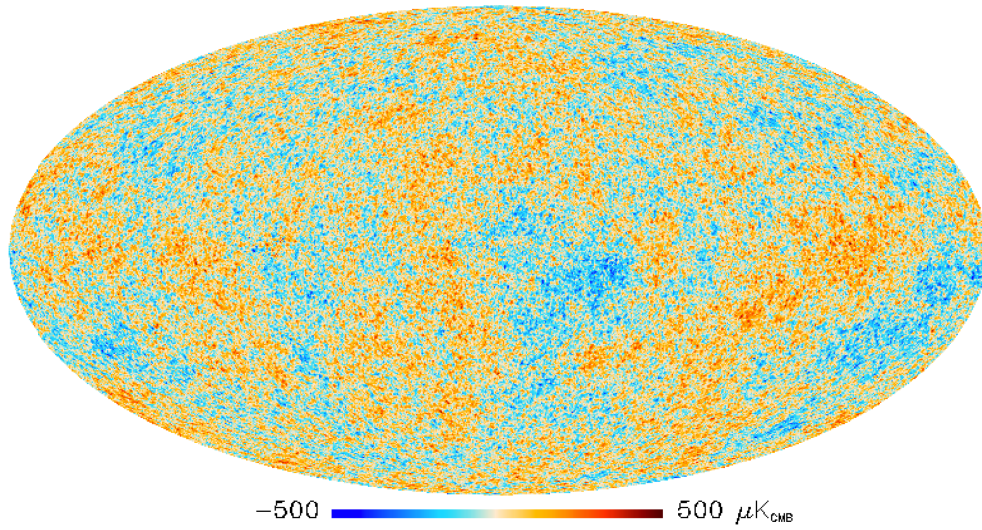


Figure 1.5: Distribution of the temperature fluctuation in universe measured by the Planck satellite [6] .

1.1.6 N-body simulation for large scale structure of the universe

In our universe, galaxies and clusters don't distribute homogeneously and isotropically. Some of the space have much high density of galaxies called as filaments, but others do not have and called as void. The structure consisted the filaments and voids is called as the large scale structure of universe. To understand the large scale structure, N-body simulation has been performed [7]. Between each particle of N-body simulation, gravitational interaction is calculated with initial fluctuation. Recent evolution of power of computing, a particle for N-body simulation becomes larger and the time for simulation

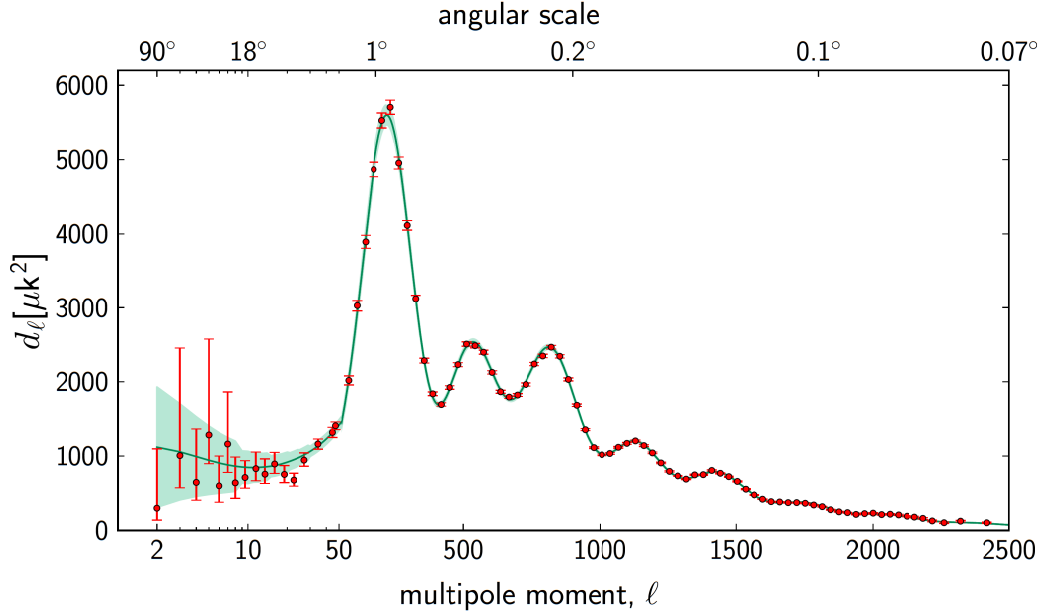


Figure 1.6: Power spectrum obtained by the temperature fluctuation.[6]

become shorter. Current result of N-body simulations indicate the existence of dark matter. By comparing the simulations with and without dark matter, structures have difference density of filaments. With dark matter, the initial fluctuation of the density of dark matter have larger effect to construct the large scale structure, because of the high number of energy density of dark matter. The result of simulation with dark matter is well matched with the observed large scale structure of galaxies. Without dark matter, filaments are more faded than observed one.

1.2 Candidates of dark matter

Candidates of dark matter can be roughly categorized into two groups. One is the celestial bodies, such as black holes, neutron stars, and brown dwarfs. These kind of celestial stars cannot be observed with photons.

The other is elementary particles. To explain dark matter by the elementary particles, particles in the standard model were examined so far. However

particles of beyond standard model are also become considered, since some of observational results cannot be explained by the particles in the standard model.

1.2.1 MACHOs

As already discussed, celestial bodies which don't emit and reflects photons, being called as MACHO (MASSive Compact Halo Object), cannot be observed by telescopes directly. If there are much amount of these celestial bodies, they can explain the dark matter. Though they cannot be observed directly, they can be observed through the "micro-lensing effect". When MACHOs across to some light sources, gravitational lensing effect gathers the diffused photons. This process makes the increase of light from the source at moment. Since the observational probability of the micro-lensing effect is quite small, an observation needed to record the data for long time, and see the increase of light. The MACHO experiment [8], EROS experiment [9] observed MACHOs. They found the candidate of MACHOs, but they are not enough (only 5-30%) to explain all of dark matter in a galaxy.

1.2.2 Neutrinos

Neutrinos, which are observed by various detectors were also candidate of the dark matter. Much amount of neutrinos are produced thermally at the first of the universe, and they are expected to remain as CMB and called $C\nu B$. The temperature of $C\nu B$ is about 2 K from the calculation, so they distribute in the universe. According to the measurements of neutrino oscillation by Super-Kamiokande and the SNO experiment neutrinos have finite and light masses. They distribute relativistically since neutrinos have light masses, however, relativistic dark matter defuses too fast to form the galaxies or clusters, based on the current observation of universe. Because of that, neutrinos cannot explain a major part of dark matter.

1.2.3 axions

Axion is one of the beyond standard model (BSM) particles, which is required by the observed CP conservation in QCD. The Lagrangian of the strong interaction has CP violating term naturally, but the non-observation of CP violation for strong interaction shows the CP of strong interaction is

conserved within a level of 10^{-9} . To achieve this conservation we need to make a fine tuning of the parameter in the QCD Lagrangian. To avoid this problem, axion was devised by Pecci and Quinn. Axions are generated at the early of universe through non-thermal process. Because of this production mechanism, their momentum is small unlike neutrino. These characteristics predicts that the axion is a good candidate of the particle dark matter model.

1.2.4 WIMPs

Weakly Interactive Massive Particles (WIMPs) is a general name for the particles with mass and weak interactions. The WIMPs are able to explain the observational results. The standard model doesn't have a particle with such characteristics, but there are some candidates of WIMPs in BSM.

For example, the supersymmetric model is one of the most important BSM model. In the supersymmetric model, there are additional particles pairing each elementary particle in the standard model. The supersymmetric particles have a new symmetry called R-parity. R-parity +1 is assigned for particles in the standard model, and -1 is assigned for supersymmetric particles. The process based on supersymmetric model needs to conserve the product of R-parity, so one supersymmetric particle need to decay with at least with one supersymmetric particle. Because of this R-parity, supersymmetric particle with lightest mass, called LSP, cannot decay any more and considered to be stable relative to the age of the universe. This model allow the thermal generation of dark matter at the early universe. By considering the existence of WIMPs, the thermal production of dark matter is consistent with the measurement of CMB. Conventionally WIMPs with their mass of the order of GeV to TeV with a cross section of $10^{-(36-50)}$ are predicted by the supersymmetric models. But lighter WIMPs, such as WIMPs with mass of MeV, is becoming much interesting in recent days.

1.3 Detection of dark matter

Methods for experimental detection of the dark matter are categorized into three types.

The first method is direct detection. The XMASS experiment is one of the examples. These detectors try to observe an interaction of dark matter and normal matter, by using various signal. The second method is the generation

of dark matter by an accelerator. Though dark matter itself cannot be observed by accelerator's detector, missing mass from the vertex is calculated to find new missing particle of the BSM. The third method is indirect detection of dark matter. This types of detection try to observe self annihilation of dark matter trapped at heavy celestial bodies.

1.3.1 Interaction between the dark matter particle and nuclei

The interaction between the dark matter particles and normal matter stems from the interaction between the dark matter particle and quarks in the nuclei in an atom. Once we define the interaction with quarks, interaction for the nuclei, and atom can be calculated. The interaction between dark matter and quarks can roughly be categorized into two groups, one is the interaction changing the state of spin of the quark (Spin-Dependent, (SD) interaction), and the other is the interaction without any spin change (Spin-Independent, (SI) interaction). The SD interaction cancels out each other for the case of even mass number nuclei. For the case of the SI interaction, the interaction for each nucleon is summed up. So, there is a factor A^2 difference between the SD and the SI cross section about the dependence on the mass number A . Including the effect of the phase space, actual dependence on the mass number become A^2 for SD, and A^4 for SI for unit number of target nuclei. By using material with a large mass number, the sensitivity for dark matter becomes much larger in general.

1.3.2 Direct detection of dark matter

To observe the interaction by dark matter, several signal channels are used for direct detection: scintillation, phonon, ionization, etc. Some of detectors have multi-signal channels like scintillation and ionization, scintillation and photon, etc. Recoil energy given by a dark matter particle is a few keV or a few tenths of keV and event rate is small. Because of this a major part of the background source of the detection is natural radioisotopes contained in the material around and inside detectors. To find the signal of dark matter, we need to deploy detector at a low background site such as underground laboratories, use pure material for detectors, and achieve low threshold to extract signal from dark matter with a reasonable efficiency.

Crystals

The most famous experiment using crystals is DAMA/LIBRA which is using NaI(Tl) crystals. In 2008, they showed the result of the observation over 10 years, and claimed the existence of seasonal modulation of the event rate[10]. Though many hypotheses have been suggested to explain this annual modulation of event rate, but no clear reason was found. The DAMA/LIBRA group suggested that they are observing the event rate modulation caused by dark matter. Many experimental groups including XMASS are trying to observe this seasonal modulation to confirm DAMA/LIBRA. Details are discussed in Chapter 2. Other types of the crystal detector is developed by CRESST[11]. CRESST detector is made using CaWO_3 . This crystal can be used as scintillator and also as a thermal detector for phonon generated at an interaction.

Semiconductor

Ge and Si are used as semi-conductor detectors. The advantage of this type of detector is better energy resolution. The CDMS group developed the detector using Ge and Si crystal, and currently the Super-CDMS group is continuing the experiment with upgraded detectors [12]. Their sensor is sensitive to phonons and ionization signal. By using these two signal channels, they can separate the electron recoil signal and nuclear recoil signal.

Noble gas

The dark matter detector with noble gas is crudely categorized by its target material and the design of detectors. For the material, Xe and Ar are widely used. For the design of detectors, single-phase and dual-phase detectors are running. Table 1.1 shows the dark matter search experiment using noble gas for their detector material. These detectors are using noble gas in liquid

Material	Single phase	Dual phase
Xe	XMASS [15]	XENON [16], LUX [17], PANDA-X [18]
Ar	DEAP [13]	DARKSIDE [14]

Table 1.1: Direct dark matter experiment using noble gas.

phase at low temperature such as -100 or -200 °C. One of the advantages

of these noble gas is that these liquid materials are useful for scaling up detectors. Even though crystals or semiconductor detectors are constructed with a few hundred kilograms at maximum, multi-ton scale detectors are already achieved for both of xenon and argon. The XENON1T detector contains 3 tons of xenon in its whole detector, and one ton of xenon for its fiducial volume. The DEAP3600 detector has 3.6 ton of whole mass and 1 ton in its fiducial volume. Because the sensitivity for the dark matter is proportional to the mass of the detector if background is negligible, these large scale detector has the advantage. The other advantage of xenon as the detector material is large atomic number, no long-life RIs in xenon, etc. They will be discussed in the section 3.2.1. On the other hand, the largest advantage of Ar is the lower cost for production. But because of the existence of longer life RI of Ar, ^{39}Ar with its half life about 200 years, it is difficult to lower the energy threshold.

1.3.3 Other types of detection

1.3.4 Accelerator detection

The accelerator experiments, such as at LHC, are also running to generate particles beyond the standard model, and look for candidates of dark matter. Although dark matter particles themselves do not interact with the detector, they can be observed by detecting missing mass or energy at the interactions. Currently no candidates are observed even during the high energy run of LHC [19, 20].

1.3.5 Indirect detection

It is thought that a large amount of dark matter is trapped at a galactic center or at a star such as the sun. Indirect dark matter search tries to observe particles generated from the annihilation of dark matter particles. The observable particles depend on the model of the dark matter, such as positrons, anti-helium, and the deviation from the amount predicted by cosmic rays theories must be observed. Recent observations such as PAMELA [21] are reporting that the ratio of the number of electrons and positrons can not be explained by current cosmic ray models and the existence of 1 TeV dark matter is indicated. However there is a possibility that it can be explained by products of other celestial bodies such as a pulsar, so it has not yet provided

any evidence of dark matter. Other experiment, such as Super-Kamiokande is also trying to observe high energy neutrinos which are thought to occur due to pair annihilation of dark matter, but currently no significant signals are observed [22].

1.4 Current situation of direct dark matter search

Figure 1.7 show the current situation of direct searches. In this figure, CRESST-II [11], CRESST surface detector [23], DAMIC [24], DAMA/LIBRA [10, 25, 26], CDMSLite [27], SuperCDMS [12], CDMS Si [28], XMASS modulation analysis [29], XMASS fiducial volume analysis [30], LUX [17], XENON1T [16], PANDAX [31, 18] are shown. The shaded region at the bottom shows the region where neutrino coherent scattering causes background.

WIMPs with a larger mass are investigated by noble gas detectors. Current best limits are achieved by XENON1T and PANDA-X. On the other hand, WIMPs with mass of a few GeV or below has been investigated by crystal detector and semiconductor detectors. Recently theorists are suggesting to investigate the sub-GeV WIMPs by using the bremsstrahlung emission at the collision of dark matter and xenon nuclei [33]. This is the main topic of this thesis, and will be discussed in the chapter 2.

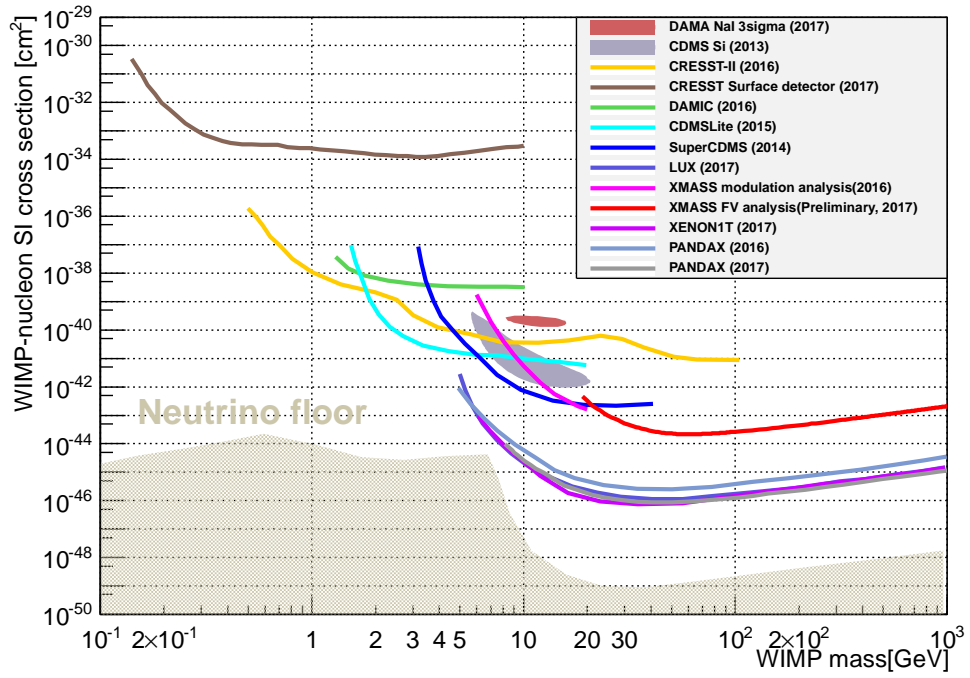


Figure 1.7: Current constraints for WIMP-nucleon cross section and its mass. See text for details.

Chapter 2

Dark matter search by annual modulation of event rate

A search for annual modulation is one of strong methods to extract dark matter signal from observed data including background caused by radioisotopes (RIs) as in [32]. Background, especially caused by U or Th from detector material, is stable for long years, but signal from dark matter is modulated by the motion of the earth. In this chapter, expected signal of dark matter and previous experimental results to search for annual modulation are summarised.

2.1 Kinematics of elastic scattering between dark matter and nucleus

In this section, the kinematics of dark matter interaction, especially for the kinematics between a nucleus and WIMP dark matter particle is reviewed. Here the nuclear recoil dark matter interaction is focused on.

2.1.1 Energy spectrum of nuclear recoil

Total event rate

In this section, we assume the collision between the dark matter particle χ and the nucleus whose element number Z and mass number A . The goal of this section is to calculate the differential cross section $\frac{dR}{dE}$. The differential

event rate dR is described using the number of particle dn :

$$dR = \frac{N_0}{A} \sigma_0 v dn, \quad (2.1)$$

where N_0 is the Avogadro number, A is the mass number of the target of detector, σ_0 is the cross section of the elastic scattering, and v is the velocity of dark matter. The cross section σ_0 is treated as constant in this section for simplification, but in the actual calculation of energy spectrum, we need to consider dependence of momentum transfer. And the differential number of particles dn is

$$dn = \frac{n_0}{k} f(v, v_E) d^3v, \quad (2.2)$$

where n_0 is mean dark matter particle number density, $f(v, v_E)$ is the velocity distribution of dark matter, which is not accurately known. The model of dark matter distribution most commonly used, and used in this thesis, is Standard Halo Model (SHM) which is described by the simple Maxwellian distribution. There are some other models, for example, Maxwellian distribution with dark matter rotational disk (dark disk model), and the model with dark matter stream from outside of the milky way, etc. In SHM, velocity distribution $f(v, v_E)$ is calculated as

$$f(v, v_E) = e^{-\frac{(v+v_E)^2}{v_0^2}}, \quad (2.3)$$

where v_0 is the velocity dispersion of dark matter around the sun, and is 232 km/s. By using these equations total event rate of the scattering between dark matter and nucleus R can be calculated as

$$\begin{aligned} R &= \frac{N_0}{A} \sigma_0 \int v dn \\ &= \frac{N_0}{A} \sigma_0 \frac{n_0}{k} \int v f(v, v_E) d^3v, \end{aligned} \quad (2.4)$$

where k is normalize factor and calculated as

$$k = \int f(v, v_E) d^3v. \quad (2.5)$$

Differential event rate

Because dark matter particles are assumed to be non-relativistic, the relationship between the kinetic energy E and velocity v of dark matter with

mass m is expressed as $E = \frac{1}{2}mv^2$. Assuming a dark matter particle scatters a target nucleus with mass M with an angle of ψ , recoil energy of $E_R = 2E \frac{Mm}{(m+M)^2} (1 - \cos \psi)$ is given to the nucleus. E_R distributes uniformly with $\cos \psi$. This leads a range of E_R , $0 < E_R < Er$, where $r = \frac{4mM}{(m+M)^2}$. By using the total event rate calculated in the previous section, a differential event rate $\frac{dR}{dE_R}$ is calculated as,

$$\begin{aligned}
\frac{dR}{dE_R} &= \int_{E_{min}}^{E_{max}} \frac{1}{Er} dR(E) \\
&= \frac{1}{E_0 r} \int_{v_{min}}^{v_{max}} \frac{v_0^2}{v^2} dR(v) \\
&= \frac{1}{E_0 r} \frac{N_0}{A} \frac{n_0}{k} \sigma_0 v_0^2 \int_{v_{min}}^{v_{max}} \frac{1}{v} f(v, v_E) d^3v,
\end{aligned} \tag{2.6}$$

where E_{max} is determined by the upper limit of dark matter velocity from astrophysics, such as escape velocity of the milky way. Hereafter 544 km/s is used for the escape velocity, which is used most commonly among direct search experiments. E_{min} is $\frac{E}{r}$, which is the smallest energy which can give certain recoil energy E_R .

2.1.2 Nuclear bremsstrahlung caused by sub-GeV WIMP

Conventionally, WIMPs are expected to cause nuclear recoils. Recoil energy of Xe nuclei can be calculated by classical kinematics [32]. The expected recoil energy spectra are shown in Fig. 2.1. It is observed that only small energy deposition is expected for Sub-GeV WIMPs. This make it difficult to observe low mass WIMPs by nuclear recoil signal in scintillation material such as scintillation of liquid xenon caused by nuclear recoil. Recently it is pointed out that even small energy of nuclear recoil leads electron recoil signal through bremsstrahlung of a γ ray [33]. It is expected to cause energy deposition of a few keV even from Sub-GeV WIMPs.

Emission of bremsstrahlung photons from the collision between a dark matter particle and nucleus

It is common feature that an accelerated charged particle emits bremsstrahlung photons and lose its energy. The origin of bremsstrahlung photon is change

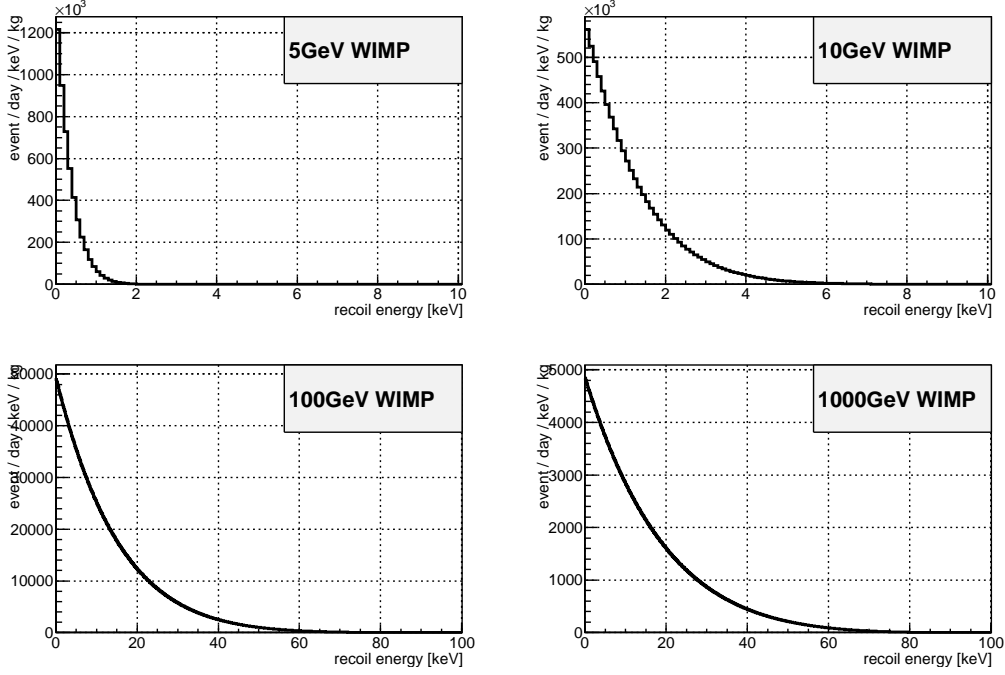


Figure 2.1: Energy spectrum of the nuclear recoil caused by each mass of WIMPs.

of the momentum of a charged particle. Thus, a collision of a charged particle emits photons. Similarly, nuclear bremsstrahlung can be a probe of the collision between a Xe nucleus and a dark matter particle. Bremsstrahlung from the collision of charged and non-charged particle is subject to the mass of the charged particle.

Calculation of differential cross section for a bare nucleus

In the classical electrodynamics [34], differential intensity of radiation emitted from the momentum change of bare charged particle is calculated as

$$\frac{d^2 I}{d\Omega_\gamma d\omega} = A \cdot \left| \int \frac{d}{dt} \left[\frac{N \times (n \times \beta)}{1 - n \cdot \beta} \right] e^{i\omega[t - n \cdot r(t)]} dt \right|^2, \quad (2.7)$$

$$A = \frac{Z^2 e^2}{4\pi^2 c}, \quad (2.8)$$

where, Ω_γ is solid angle, and ω is frequency of emitted photons (NOT scattered nucleus). Factor A depends on the charge of the particle as Eq. 2.8. n

is the unit vector from the point of collision and the point of observation, and β is the reduced velocity. In the low energy approximation, ω is small and in integral can be treated as 1. Since the kinematics of dark matter recoil is non relativistic, $|\beta| \ll 1$. In this case, Eq. 2.7 can be calculated by integration. Then, using polarization vector ϵ , Eq. 2.8, Eq. 2.7 can be written as

$$\begin{aligned}
\frac{d^2 I}{d\Omega_\gamma d\omega} &= A \cdot |\epsilon \cdot (n \times (n \times \beta) - n \times (n \times \beta'))|^2 \\
&= A \cdot |\epsilon \cdot ((n \cdot \beta - n \cdot \beta') n - \beta - \beta')|^2 \\
&= A \cdot |\epsilon \cdot (\beta - \beta')|^2.
\end{aligned} \tag{2.9}$$

For the case of a liquid Xe detector such as XMASS-I, total intensity is calculated by integrating Eq. 2.9 by solid angle and summing up with polarization.

$$\begin{aligned}
\frac{dI}{d\omega} &= A \cdot \sum_{\epsilon_{\perp, \parallel}} \int d\Omega |\epsilon \cdot (\beta - \beta')|^2 \\
&= A \cdot 2\pi \cdot \frac{8}{3} \cdot |(\beta - \beta')|^2 \\
&= \frac{2z^2 e^2}{3\pi c} \cdot |\Delta\beta|^2.
\end{aligned} \tag{2.10}$$

A differential cross section of the recoil with emitting bremsstrahlung photon, $\frac{d^2 \sigma}{d\omega dE_R}$, is

$$\begin{aligned}
\frac{d^2 \sigma}{d\omega dE_R} &= \frac{d\sigma}{dE_R} \cdot \frac{dN}{d\omega} \\
&= \frac{d\sigma}{dE_R} \cdot \frac{1}{\omega} \frac{dI}{d\omega},
\end{aligned} \tag{2.11}$$

where $\frac{dN}{d\omega}$ is the number of emitted photon per energy. Note that $\omega N = I$. Using nuclear mass M , recoil energy E_R , $|\beta|^2 = \frac{2E_R}{M}$, Eq. 2.11 is calculated as

$$\begin{aligned}
\frac{d\sigma^2}{d\omega dE_R} &= \frac{d\sigma_{el}}{dE_R} \cdot \frac{1}{\omega} \frac{2z^2 e^2}{3\pi c} \cdot |\Delta\beta|^2 \\
&= \frac{d\sigma_{el}}{dE_R} \cdot \frac{1}{\omega} \frac{2z^2 e^2}{3\pi c} \cdot \frac{2E_R}{M} \\
&= \frac{4z^2 e^2}{3\pi} \cdot \frac{1}{\omega} \frac{E_R}{M} \frac{d\sigma_{el}}{dE_R}.
\end{aligned} \tag{2.12}$$

Calculation with the effect of atomic structure

In the previous section, the differential energy of photons from bremsstrahlung is calculated based on the classical theory, assuming the scattering of a bare nucleus and dark matter particle. However, the effect of electron cloud in the atom needs to be considered in real situation.

In this case, the scattered nucleus and electron clouds are considered to form an electric dipole structure. By this approximation, the differential cross section is

$$\frac{d^2\sigma}{d\omega dE_R} = \frac{d\sigma_{el}}{dE_R} \cdot \frac{1}{\omega} \frac{|f(\omega)|^2 e^2}{3\pi c} \cdot |\Delta\beta|^2. \quad (2.13)$$

Detailed derivation of this equation is given in [33]. Comparing the Eq. 2.13 to the classical calculation, charge number of nucleus Z is change to the function of ω , $|f(\omega)|$, which represents the correction of the intensity of photons by the atomic structure. $f(\omega)$ is expressed as $f_1 + i \cdot f_2$ and have a structure called anomalous dispersion around the binding energy of each atomic electrons. f_1, f_2 and $|f|$ of atomic scattering factor f for xenon are calculated by NIST [35], and shown in Fig. 2.2.

Energy spectrum of the emitted photon

In the previous section, the differential cross section of the nuclear bremsstrahlung $\frac{d^2\sigma}{dE_R d\omega}$ was calculated. Then, the differential spectrum is obtained by integrating the energy spectrum of photons as

$$\frac{d\sigma}{d\omega} = \int_{E_{min}}^{E_{max}} dE_R \frac{d^2\sigma}{dE_R d\omega}. \quad (2.14)$$

By considering the energy of emitted photon, it becomes

$$\frac{d\sigma}{d\omega} = \frac{4e^2 |f(\omega)|^2}{3\pi\omega} \frac{\mu_N^2 v^2 \sigma_0^{SI}}{m_N^2} \sqrt{1 - \frac{2\omega}{\mu_N v^2}} \left(1 - \frac{\omega}{\mu_N v^2}\right) \quad (2.15)$$

By integrating Eq. 2.15 with the velocity distribution, we can obtain the expected event rate of the bremsstrahlung photons as Eq. 2.16, per unit detector mass and unit density of dark matter.

$$\frac{dR}{d\omega} = \frac{\rho_\chi}{m} \int v f(v, v_E) \frac{d\sigma}{d\omega} d^3v. \quad (2.16)$$

The energy spectra of photons from bremsstrahlung with and without correction are shown in Fig. 2.3.

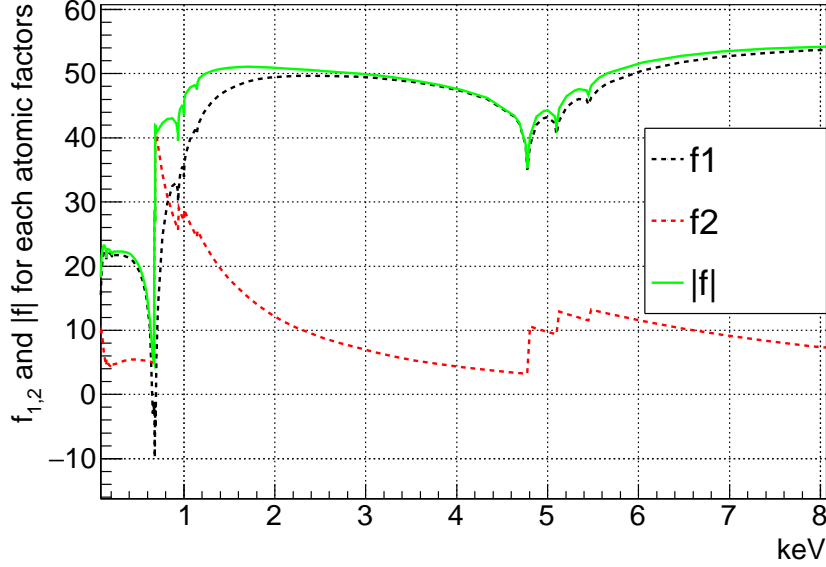


Figure 2.2: Atomic scattering factor f of a xenon atom. Black, red, and green lines show the real part, imaginary part, and the absolute value of the factor f , respectively.

2.2 Annual modulation of the event rate of nuclear recoil

In SHM, dark matter particles have the Maxwell distribution. Annual modulation of dark matter would be caused by the revolution of the earth around the sun. The relative velocity of dark matter and the detector on the earth, v_{det} , is described as follows.

$$\mathbf{v}_{det} = \mathbf{v}_{sun} + \mathbf{v}_{earth}. \quad (2.17)$$

Actually, \mathbf{v}_{earth} have both of revolution around sun and self rotation of the earth. Because the rotation speed of the earth is much smaller than that of revolution, only the effect from revolution is considered in Eq. 2.17. \mathbf{v}_{sun} is estimated as 232 km/s and

$$\begin{aligned} v_{earth} &= 1 \text{ AU} * 2\pi / 1 \text{ year} \\ &= 1.496e + 8 * 2\pi / 365.25 / 24 / 3600 \\ &= 29.8 \text{ km/s.} \end{aligned} \quad (2.18)$$

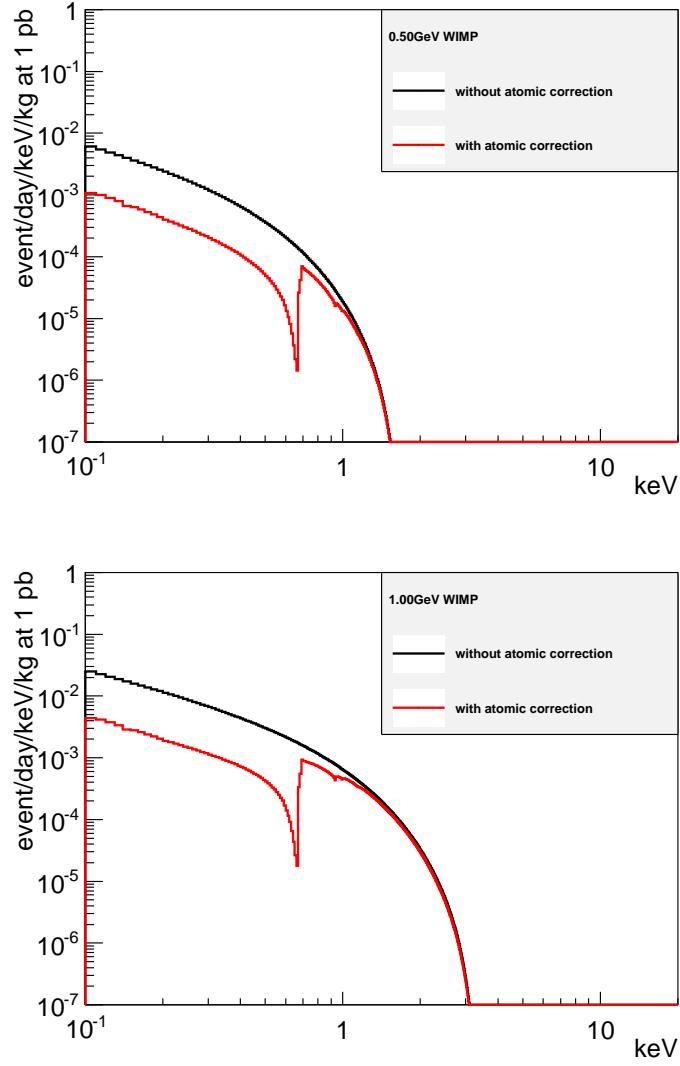


Figure 2.3: Energy spectrum of emitted photons from nuclear bremsstrahlung for mass of 0.5 and 1.0 GeV WIMPs. Cross section between WIMPs and nucleus is assumed as 1 pb. Black and red lines are bare nucleus case and considering atomic structure, respectively.

This velocity shows the mean value of earth's rotation speed. However the elliptic plane and \mathbf{v}_{sun} form and the angle is about 60 degrees. As a result, the absolute value of relative velocity of dark matter and the detector v can be written as

$$\begin{aligned} v &= v_{sun} + v_{earth} \cdot \cos \frac{t - t_0}{T} \\ &= 232 + 15 \cdot \cos \frac{t - t_0}{T}, \end{aligned} \quad (2.19)$$

where, t_0 and T show the offset of time and period of the earth's rotation, respectively. Note that the speed of solar system have uncertainty of about 10%. With the first order of approximation, annual modulation of differential event rate can be written as

$$\left. \frac{dR}{dE_R} \right|_E = A_0 + A_{annual} \cdot \cos \frac{t - t_0}{T}, \quad (2.20)$$

where T, t_0 are same as in Eq. 2.19. As already discussed in the previous section, the velocity distribution of dark matter is assumed to be Maxwellian. In the this halo model and standard WIMPs, T is one sidereal year and t_0 is 152.5 days. Event rate $\frac{dR}{dE_R}$ becomes maximum on 2nd of June and minimum on 4th of December.

A_0 and A_{annual} are subject to characteristics of dark matter particles. For example, different mass of WIMPs gives different A_0 and A_{annual} . Since they depend only on the cross section, we can compare the history of event rates with changing the cross section of WIMPs. Other models of dark matters are expected to give different A_0 and A_{annual} . t_0, T are dependent on halo models. Figure 2.4, 2.5 and 2.6 show the expected nuclear recoil spectrum, modulation part of nuclear recoil spectrum and expected time evolution caused by 10 GeV WIMPs, respectively. Details of fitting functions are discussed in the following chapter.

2.3 Experimental detection of annual modulation

Dark matter searches by using annual modulation has been performed over 20 years. Historically this method become famous because DAMA/LIBRA claimed a positive result. Though we discussed annual modulation caused

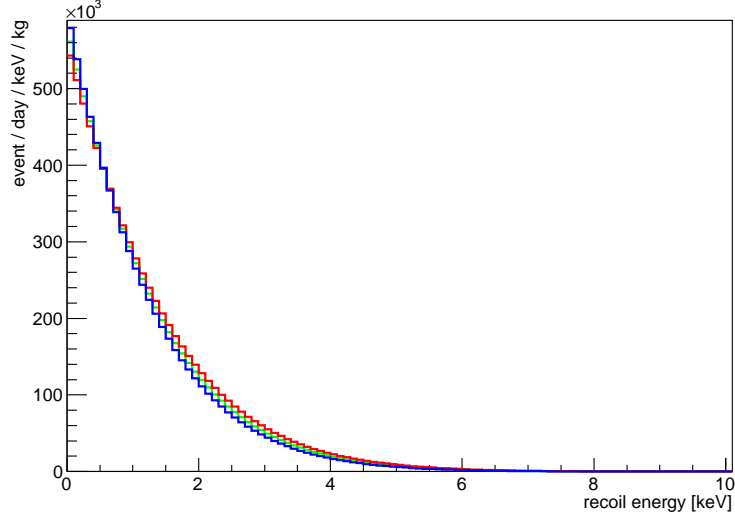


Figure 2.4: $\frac{dR}{dE}$ for 10 GeV WIMPs. Red, blue, and green lines show the spectra at summer, winter, and yearly averaged.

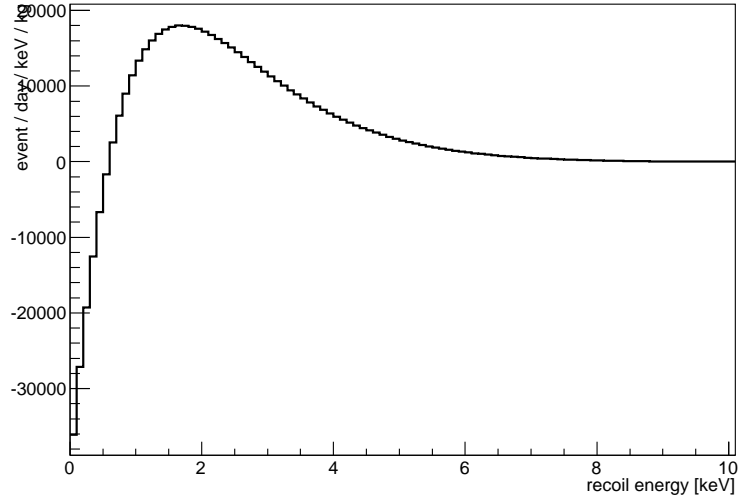


Figure 2.5: Modulation part, A_{annual} for 10 GeV WIMPs.

by WIMPs based on SHM, we also can search for the event rate modulation of any other dark matter model. For example, both of electron recoil dark matter and nuclear recoil dark matter need to be searched for.

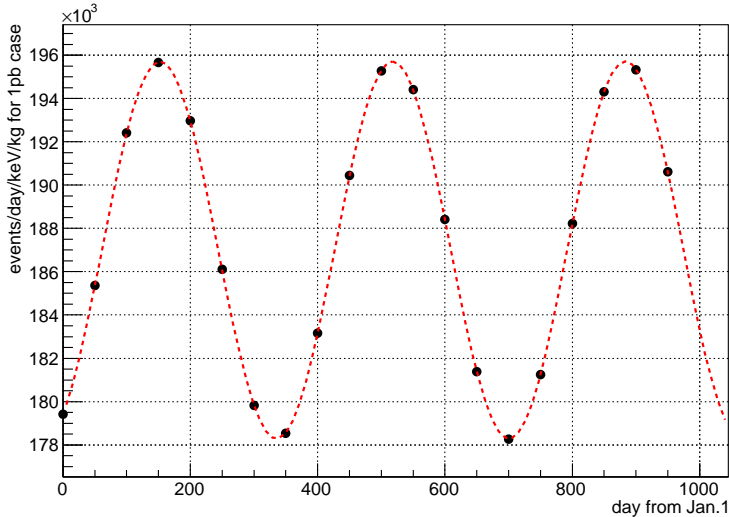


Figure 2.6: Expected time evolution of event rates for 10 GeV WIMPs at 1-2 keV. Black points are calculated based on the velocity at each time, using Eq. 2.19. The red line is smoothly interpolated curve calculated using cosine. Time of points are normalized at January 1st.

2.3.1 DAMA/LIBRA

In 2008, the DAMA/LIBRA group published the result of their observation using NaI(Tl) [10]. Figure 2.7 shows the observed amplitude at 2 - 6 keV. The result of the observations was clearly indicating a cosine curve of event rate modulation. The period and the phase of the cosine curve was consistent to the SHM WIMPs dark matter model. They had several upgrades of their detector, basically by increasing the detector mass. The updated result published in 2013 has exposure of 1.04 ton year [25]. Including the experiment DAMA/NaI, which is done before DAMA/LIBRA, the total exposure is 1.33 year. They claim that they are observing the annual modulation of rate caused by dark matter particles. The DAMA group simply showed the amplitude of modulation of event rate. Since their data include both of events caused by electron and nuclear recoils, WIMPs as well as more exotics can be considered. This is the reason why other experiments such as XMASS [29], XENON [36, 37, 38, 39], are looking for any modulation signal in their data without particle identification to confirm DAMA results.

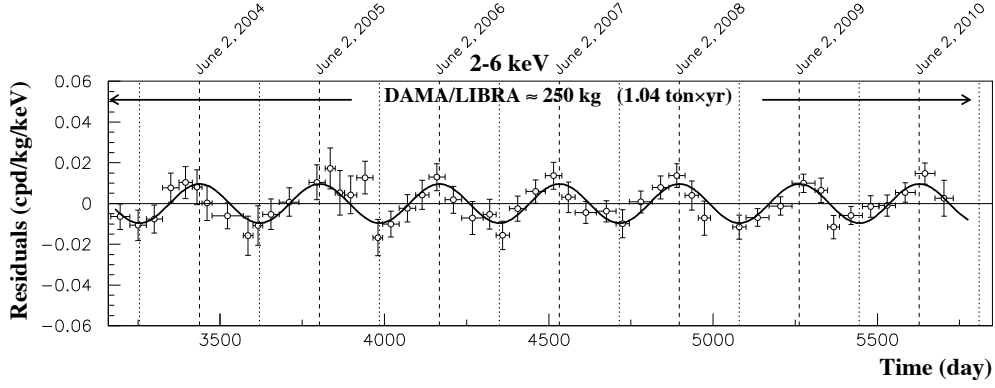


Figure 2.7: Annual modulation search by DAMA/LIBRA experiment. Total exposure is 1.04 ton year. [25]

2.3.2 XENON100

The XENON100 group published their result of the event rate modulation search with 1 year data in 2015 [37], and 4 years data in 2017 [39]. Since they had already shown a null result for nuclear recoils, it was interpreted as a constraint on electron recoil events. Figure 2.8 shows the relationships between observed amplitude and periods. In the analysis they used a profile likelihood method, and got no significant modulation amplitude. They also performed a frequency analysis, and no significant modulation was seen.

2.3.3 XMASS

In 2016, the XMASS group published a result of annual modulation search based on the data taken from November 2013 to April 2015. The data span over 1.5 year, and live time was about 500 days. Considering the detector mass, the exposure is about 1 ton year and comparable to that of the DAMA experiment. Fig. 2.9 shows the result with considering the spectrum of WIMPs. Fig. 2.10 shows the result of fitting without any assumption of the spectrum. Assuming WIMP dark matter, it rejected most of the parameter space of the allowed region of DAMA/LIBRA as shown in Fig. 2.9.

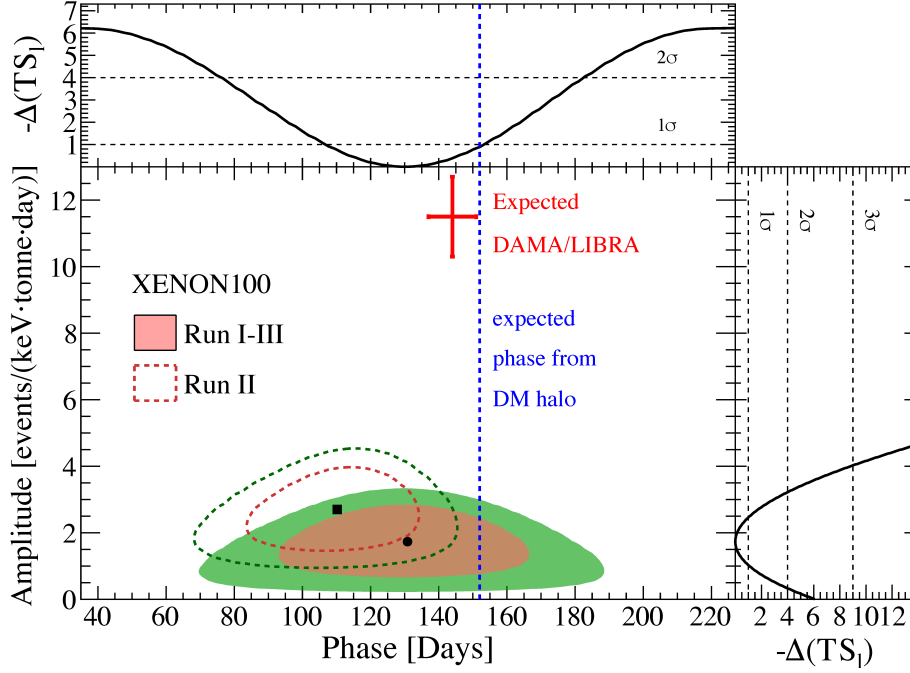


Figure 2.8: Annual modulation search by the XENON100 group [39]. The best fitted amplitude and period are shown. Filled contours are for the result using 4 years data. Dashed lines show the result using 1 year data.

2.4 Physics targets based on annual modulation search in this thesis

2.4.1 Sub-GeV WIMPs search by annual modulation of nuclear bremsstrahlung

In ref [29], the annual modulation analysis mainly focused on the DAMA expected region, and rejected most of it at 90% CL. Recently, the emission of bremsstrahlung photons is discussed in [33] and it can be used as a new probe for detection of sub-GeV WIMPs. Targets of this thesis is a Sub-GeV WIMP using annual modulation caused by bremsstrahlung photon emission. This is the first experimental result of Sub-GeV WIMP search by annual modulation.

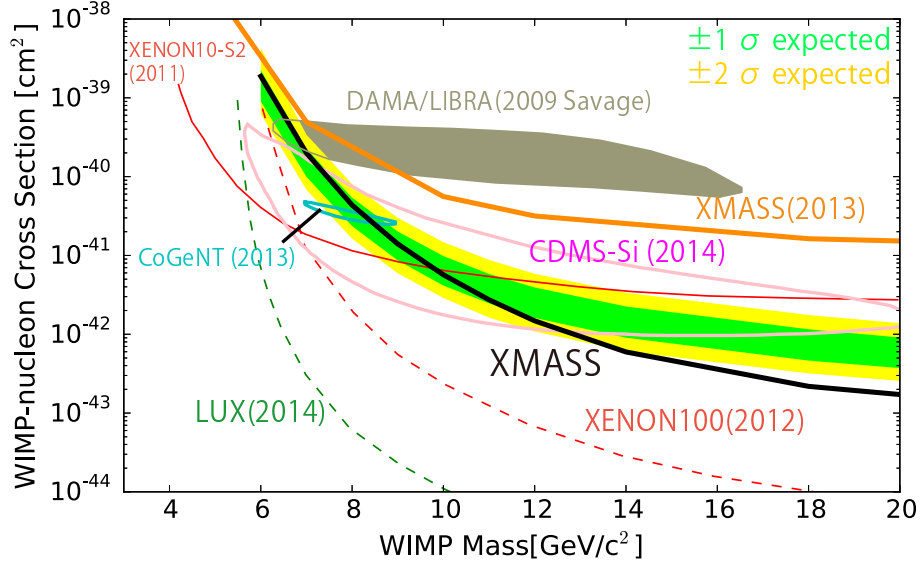


Figure 2.9: Annual modulation search by XMASS experiment. Black line shows the 90% limits by real data. Yellow and green bands are showing 1, 2 σ distribution of 90% sensitivity for null amplitude case, respectively. They are calculated by test statistics [29]

Annual modulation of bremsstrahlung photon emission spectrum

Because energy spectrum of the bremsstrahlung photons depends on the nuclear recoil energy spectrum, it has annual modulation as well. In the case of bremsstrahlung photons, annual modulation is calculated by using Eq. 2.16. The annual modulation of the energy spectrum still can be seen in first order. Expected event rates for nuclear bremsstrahlung are shown in Fig. 2.11, Fig. 2.12 and Fig. 2.13.

Energy Calibration at lower energy region

Calibration of response for electron and gamma at very low energy around 1 keV was not confirmed at the previous result of XMASS [29]. Calibration using compton scattering of gamma ray was performed by some of members of XENON group down to 1.5 keV [40]. For XMASS detector, escape effect of X-ray from ^{55}Fe source generate electrons energy around 1.2 - 2 keV. Because calibration below 1 keV do not exist, analysis for sub-GeV dark matter was conducted using the data above 1 keV. Energy calibration will be discussed

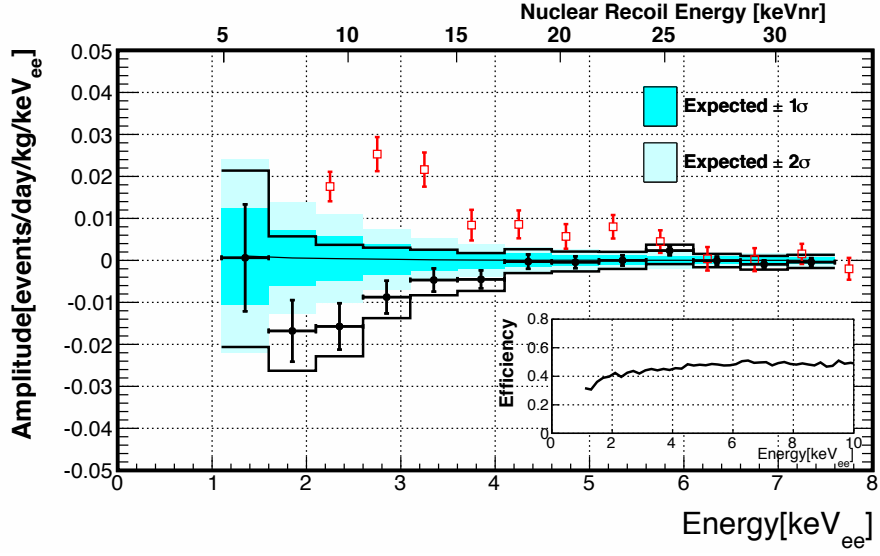


Figure 2.10: Annual modulation search by XMASS experiment. Black plots shows the best fit amplitude by data. Cyan and light cyan bands shows the $1, 2\sigma$ distribution of amplitude using test statistics [29]

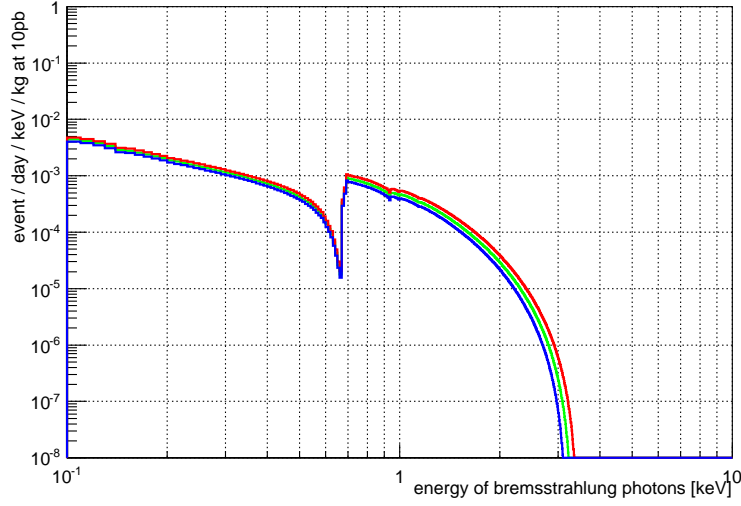


Figure 2.11: Energy spectra of bremsstrahlung for 1 GeV WIMPs. Red, blue, and green line show the spectra at summer, winter, and yearly averaged, respectively.

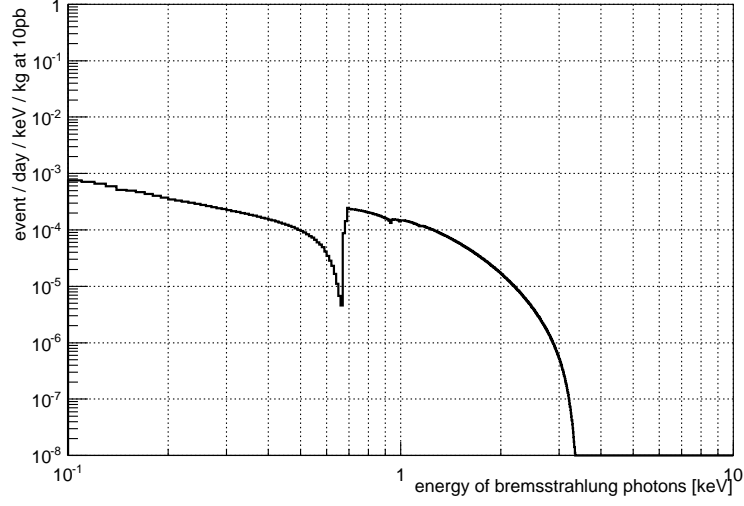


Figure 2.12: Difference between the blue and red curves in Fig. 2.11

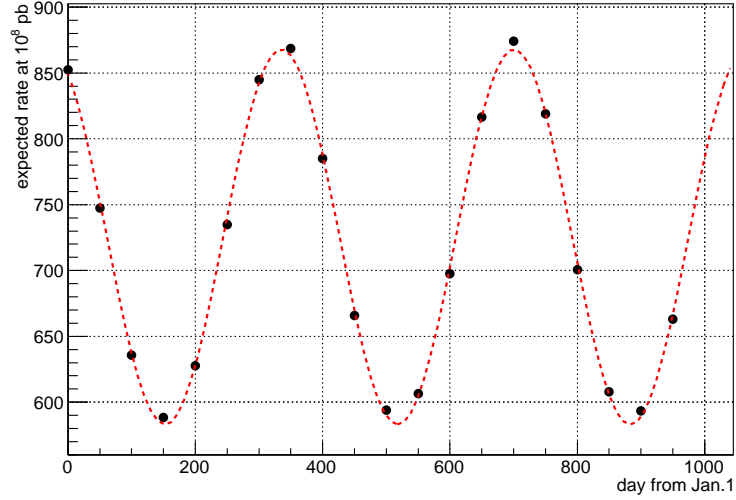


Figure 2.13: Time variation of event rate of bremsstrahlung for 1 GeV WIMPs at 1-2 keV. Each black point is calculated based on the velocity distribution at that period, using Eq. 2.19. The dotted red curve is the best fit by a cosine function. The origin of the period is started from January 1st.

in section 4.4.

2.4.2 Enhancement of sensitivity for nuclear recoil by lowering the energy threshold

For the nuclear recoil signal of WIMPs, detector threshold is important. Because of the velocity distribution discussed in Sec. 2, WIMPs event rate increase exponentially toward lower energy. By lowering the threshold of detector, sensitivity for WIMPs can be drastically improved. The second target of this thesis is enhancement of WIMPs sensitivity by lowering the energy threshold. The required multiplicity to trigger the detector DAQ was four before. In this thesis lowering multiplicity down to three was realized and achieved lowering energy threshold. Because of this, the energy threshold for WIMPs become 2.3 keVnr (4.8 keVnr in the previous analysis [29]). The improvement of DAQ hardware and mechanical noise reduction for low threshold will be discussed at Sec. 4.2 and 4.3, respectively. Figure 2.14 show the expected sensitivity for WIMPs. In this calculation only the statistics of lowest energy bins are used without any systematic error of data treatment, and -1σ line of [41] is used as the quench factor of xenon, to demonstrate its importance.

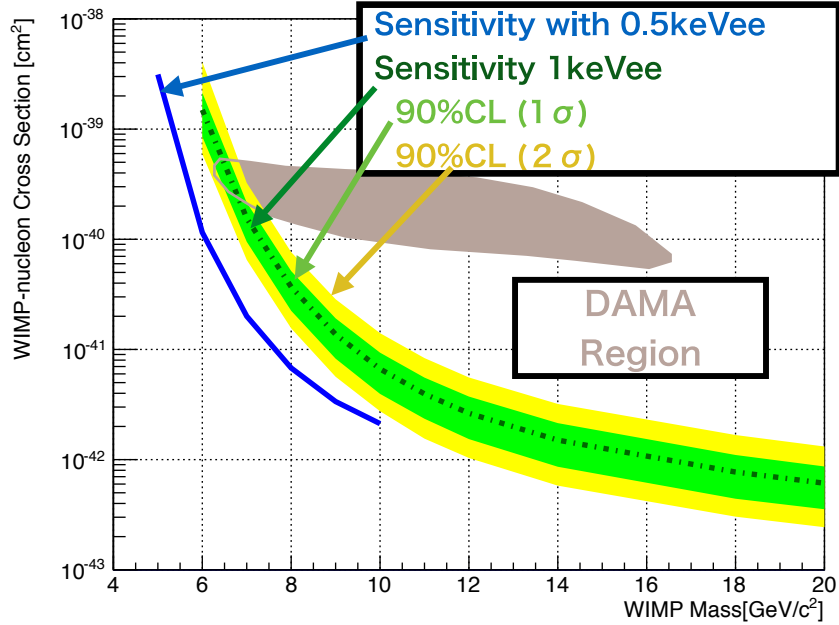


Figure 2.14: Expected sensitivity using low threshold data, without considering any systematical errors. Dark green, light green, and yellow bands are from Ref. [29].

Chapter 3

XMASS experiment

3.1 Purpose of the experiment

The XMASS experiment utilizes multi-purpose detectors for particle and cosmological physics. XMASS stands for

- Xenon neutrino MASS detector
- Xenon MASSive detector for solar neutrino
- Xenon detector for weakly interactive MASSive particles

At present, the main target of the XMASS is dark matter search. However other physics targets, for example, double electron capture, solar K-K axion are also searched for in this phase of the experiment. Also, XMASS is operating as a detector of supernova neutrinos. If a supernova close as Betelgeuse goes off, number of neutrinos are expected to be observed through coherent scattering of neutrinos.

The XMASS-I detector is operated in the Kamioka Observatory. It was constructed in 2010 and continued to take commissioning data until 2012, then refurbishment of the detector was conducted to reduce an impact of radioactive backgrounds. The XMASS-RFB detector started to take physics data in November, 2013. All data used in this thesis is taken after the refurbishment.

3.2 XMASS-I detector

The XMASS-I detector is a large and low radioactive background detector using liquid xenon. More than 1 ton of liquid xenon is used for the detector,

and 832 kg of them are in the sensitive volume. The detector is located under a mountain Ikeno-yama, Hida City, Gifu Prefecture to reduce the background (BG) due to cosmic rays. Under a large flux of cosmic rays, not only the incident particles itself cause BG but also a nuclear spallation reaction occurs with the detector materials and source of BG is also generated. These influences should be suppressed as low as possible. The Kamioka facility is 1,000 m underground and 2,700 m in terms of water, and the muon flux is 10^{-5} compared with the ground [42]. The whole view of the detector is as shown in Fig. 3.1, and a vacuum insulation container containing the LXe detector is located at the center of a water tank. In the water tank, an outer detector (OD) serving as a veto detector and a passive shield for environmental backgrounds, and an LXe detector deployed at the center called an inner detector (ID).

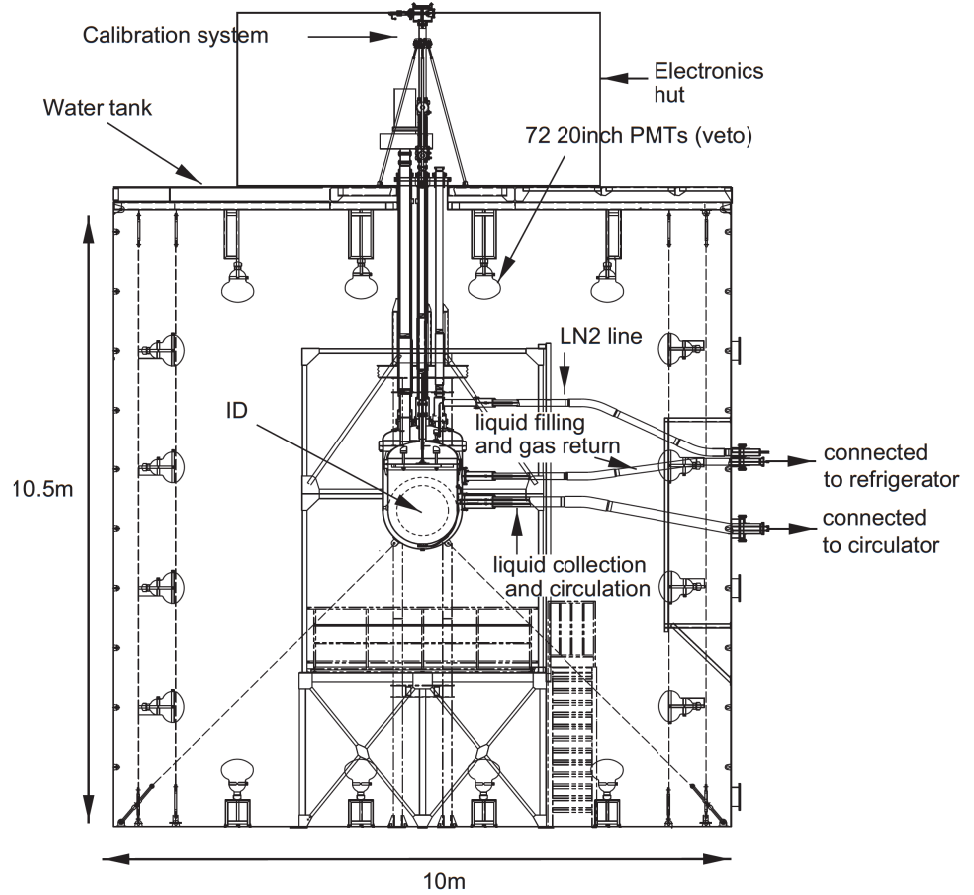


Figure 3.1: The whole view of the XMASS-I detector [15].

3.2.1 Liquid xenon

Liquid Xe is used as the target material. Liquid xenon have several advantage useful for low background experiment, and actually used for many physics experiments.

- Large atomic number
 - Xenon have the large atomic number ≈ 132 . This has two advantages as the detector material. First, the larger atomic number gives a larger cross section for dark matter. In the WIMP model, the cross section between atom and WIMP particles increases as a function of an atomic number A . For example, a spin independent cross section σ_{SI} is proportional to A^4 for the case of large WIMP mass. So material with a large atomic number have better sensitivity for nuclear scattering between WIMPs. Second, atoms with high atomic number interact more strongly with radiation. So most of radiation from natural RIs contained in detector material, such as β ray, γ ray interact with liquid xenon around the wall. This effect, called self shielding, make low BG region at the inner part of a detector. By using the inner part for dark matter search, we can reduce the most of the background.
- No long-life RIs in xenon
 - By the self shielding effect, an impact of RIs in the detector materials can be suppressed. But it does not work for the radiations from radioactive isotope of xenon, because they are dissolved in liquid xenon and distributed uniformly in the detector. For the case of other rare gas, for example Ar, has long life RI ^{39}Ar and they become background of the experiment. In xenon case, there are no long-life RIs. Since half life of radioactive xenon nuclei are a few months at most, no need to worry.
- Large scintillation yield
 - Liquid xenon is used as liquid scintillator, and number of detectable photons par unit energy is important for lowering detector threshold and improving the energy and position resolutions. Liquid xenon have large scintillation light yield, relative to other

materials. In the XMASS-I case, calibration data using 122 keV γ ray indicate that our detector have about 14 photoelectrons (PE)/keV.

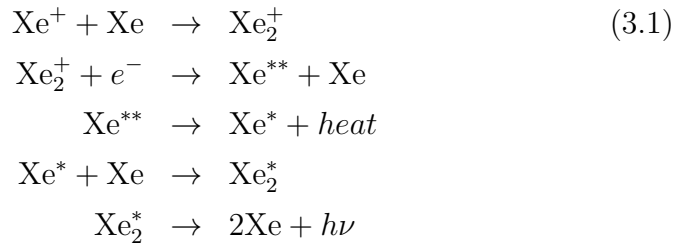
- Scalability of the detector
 - Xenon can be kept at the liquid state with -100 degree C and about 1.5 atom. This temperature can be achieved by commercial cryocooler or liquid nitrogen. Because it is liquid, detector shape is not limited and it is possible to realize large detectors. Although large and uniform crystal is difficult to make, liquid state doesn't have such limitation. Since sensitivity of the detector is proportional to the total mass of the detector once BG suppression is achieved, the scalability is much important for a dark matter search.

Scintillation process of xenon

Details of scintillation process for xenon is reported in [43, 44, 45]. The scintillation process of xenon is complicated, and it has a different scintillation decay time constant for each incident particle and for each scintillation process. In Fig. 3.2, the measured value of the decay time for each particle is shown. Particles such as α, β, γ , neutron and dark matter particles, cause two branches of scintillation process. One is electron-ion recombination process, and the other is excitation process.

First of all, let's consider radiation such as α ray and nuclear recoil that cause a high linear energy transfer. Since these incident particle ionize the surrounding Xe atoms and collides to other nucleus, both of excited states ($\text{Xe}^*, \text{Xe}^{**}$), and the ion (Xe^+) are generated. As mentioned earlier, there are two branches of scintillation processes;

1. Process with ionization-recombination



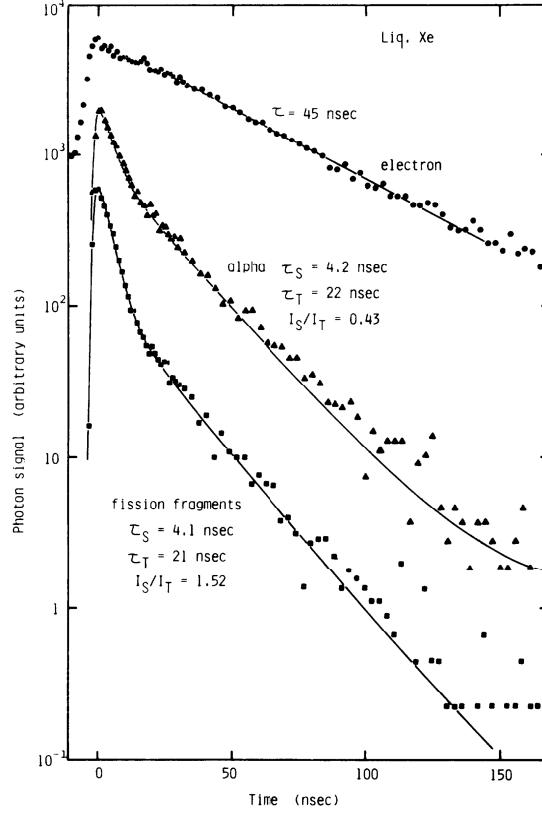
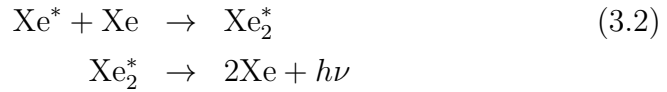


Figure 3.2: LXe scintillation decay time constant [43].

2. Process with direct excitation



In either case, finally the Xe_2^* , dimer of Xe and Xe^* , provide a photon of ultraviolet light of 175 nm. There are two types of excited state, spin singlet and triplet. The singlet state has a scintillation decay time constant of about 2-4 ns and the triplet state has about 20 ns [43, 44], and the ratio of each component varies depending on the type and energy of incident particle. For the case of radiation with low linear energy transfer such as β and γ rays the Xe^+ ion cause scintillation lights mostly through recombination. The recombination process itself is same as for α case, but the scintillation decay

time constant actually measured is about 45 ns. This is because the density of the generated ions is low and it takes time to recombine. α ray or recoiled Xe nucleus ionizes the surrounding Xe atoms with high density, Xe_2^+ and e^- easily can find the pair of recombination and causes fast decay of scintillation light.

3.2.2 Inner Detector

The inner detector (ID) in which the LXe detector is contained has a two-layer structure of Outer Vacuum Chamber (OVC) and Inner Vacuum Chamber (IVC) for heat insulation. The main body of the detector is housed inside the IVC and it consists of 642 PMTs fixed to a holder made of oxygen-free copper and the overall shape of the holder is dodecahedron. Each pentagon constituting the dodecahedron is further divided into 5 triangles structure, called pentakis dodecahedron. In addition to the PMT, six LEDs for calibration are attached to the PMT holder. The size of the detector is approximately 80 cm in diameter and the amount of inner LXe is 832 kg. In the IVC, 1114 kg of xenon is contained in total. Figure 3.3 show the structure of ID.

PMT

PMT for XMASS detector, R10789, were developed by the XMASS group and HAMAMATSU Photonics KK. The advantage of this PMT is

- Components with low RI contamination.
- High QE for the scintillation light of liquid xenon
- Stable performance at the low temperature (-100°C)

In total, 642 PMTs are used in the detector. For RI component, ^{60}Co , U chain, and Th chain, etc. were measured by using Ge detectors, and low background material were chosen for mass production.

3.2.3 Outer detector

The Outer detector (OD) is a cylindrical water tank with a height of 10.5 m and a diameter of 10 m and effectively shields neutrons and gamma rays from rock by pure water. Since ID is located in the center of the OD, thickness

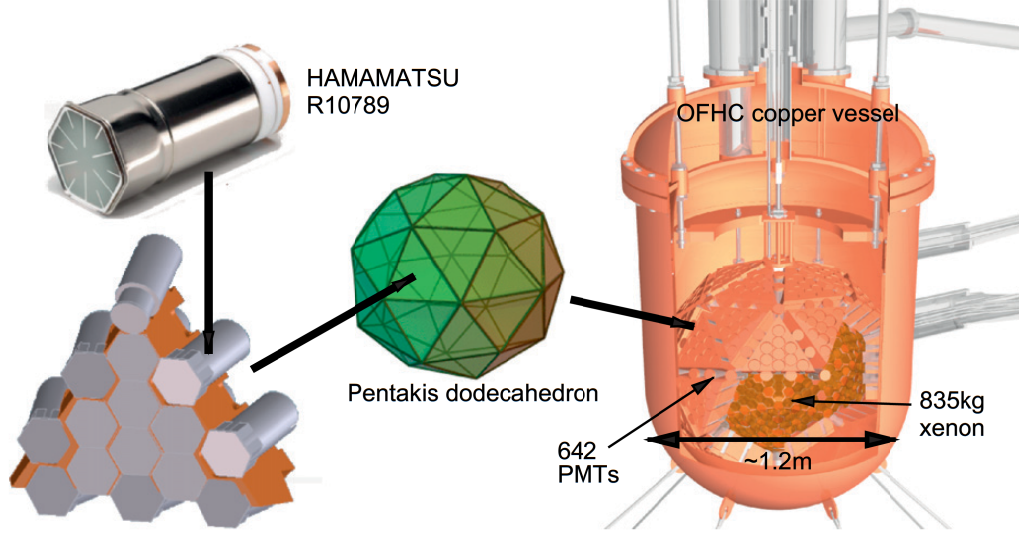


Figure 3.3: Inner detector [15]

of water is more than 4 m. 72 PMTs (HAMAMATSU R3600, 20 inch) are arranged on the inner wall surface of the tank. The OD is also used as veto for cosmic muons by observing Cherenkov light generated when a cosmic ray enters. Ultra pure water contained in the tank is generated by the same technology as for Super-Kamiokande. Since Rn in water may cause a fake signal in the annual modulation analysis its radioactive level is suppressed below several hundred mBq/m³.

3.2.4 DAQ system

The DAQ system of the XMASS-I detector consist of two types of electrical modules. One is called as ADC TDC Module (ATM) and the other is Flash ADC (FADC). Though ATMs have the capability of recording timing and charge, they are used only for making triggers. FADCs record raw waveforms of the PMT signal useful for data analyses.

Trigger system

XMASS-I has triggers categorized into four types.

- Inner detector trigger
- Outer detector trigger
- Clock trigger every 1 sec
- Special configuration for DAQ works

A trigger module assigns the trigger identification (triggerID) for each event, such as normal trigger, low threshold trigger, OD trigger, clock trigger, etc. An ID trigger system which is used for physics analyses will be explained below.

ID Trigger

Raw signal from the PMT is sent to pre-amplifier (preamp), and then it is fed into ATM and FADC. A trigger to record the signal is made by ATM. ATM makes the square wave called HIT with 200 ns width and 11 mV height when preamp sends waveform with more than 0.25 PE in height. All HIT signals are summed up in individual module and cause a HITSUM signal from each module. They are sent to discriminator after summing up all HITSUM from all the modules. DAQ system of XMASS-I is triggered by an event, when total height of HITSUM exceed the threshold of the discriminator. The threshold is set to -40 mV from baseline from the beginning, and -25 mV threshold is added from December 2015. -40 mV (≈ 4 hits) data is called as normal ID trigger, and -25 mV (≈ 2.5 hits) data is called as low threshold ID trigger. The detail of development of the low threshold trigger is discussed in Sec. 4.2. The discriminator sends NIM signal to a trigger module called TRG. The TRG module has several channels to assign different bit number of trigger ID, and each events can be categorized by the trigger ID. This module receives eight input signal with the NIM standard, and assigns the trigger ID. The triggerID consists of eight bits correspond to each channel. Timing of the event is defined by the timing of the logic signal firstly arrives. Signals coming within 150 ns from the first logic signal are treated as same event and trigger information is combined. For example, if ID trigger (0th bit) and OD trigger (1st bit) come within 150 ns, that event will have trigger

ID 3 ($= 2^0 + 2^1$).

The output NIM signal from the TRG module is used as a global trigger, and sent to all ATMs and FADCs. Then all modules records their data as one event. Figure 3.4 shows the trigger system of XMASS-I detector.

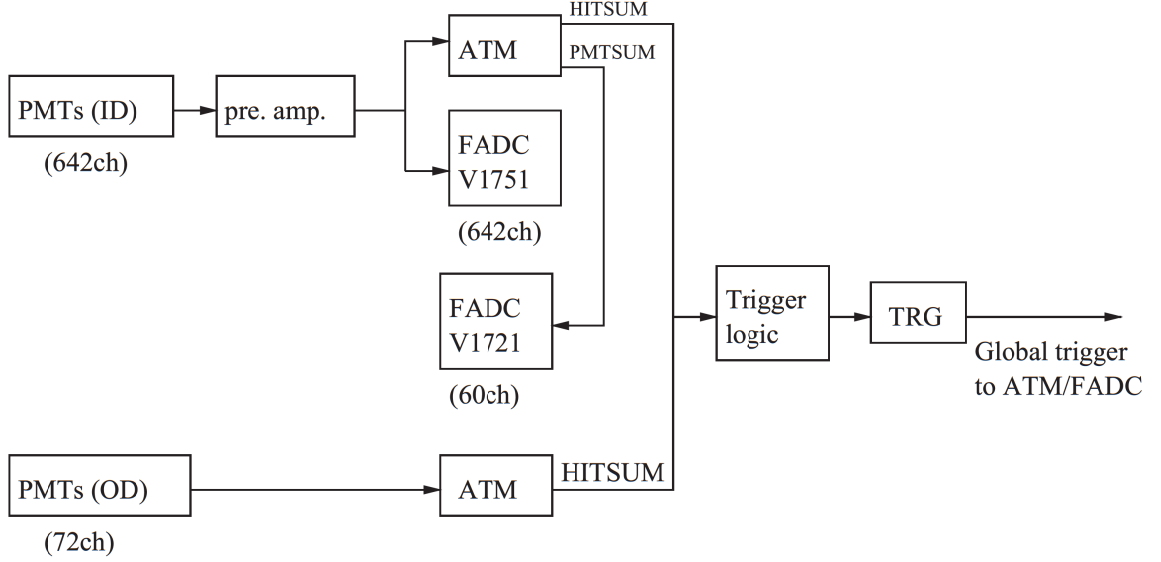


Figure 3.4: Simplified trigger flow of the XMASS-I detector. The TRG module sends the global trigger to all modules, and record the trigger ID for each types of input trigger. FADC V1721 is used only at the commissioning phase of the XMASS-I detector [15].

FADC

FADC used in XMASS-I is CAEN V1751. Its timing resolution is 1 ns, and dynamic range is 1 V. The size of time window of recorded waveform is set to be 10 μ s for each event in XMASS-I. But, a timing window for actual analysis is set to be [-200, 300] ns from the trigger timing. This is important to avoid afterpulses and noises after bright events. PMT output charges of each recorded pulse is integrated, and converted to number of PEs by using a gain table for individual PMTs. Figure 3.5 shows the specification of FADC.



Channels	8
Sampling rate	1GHz
Resolution	1mV/count
Dynamic range	1Vpp

Figure 3.5: FADC V1751, which is used in the XMASS DAQ [46, 47].

3.3 Calibration system

3.3.1 Inner calibration system

Detector stability was monitored by inner source calibration. Figure 3.6 shows the schematic view of the calibration system. From the IVC of the detector, calibration guide tube extends up to the top of the water tank. At the top of inner calibration guide tube, there is a stepping motor. This stepping motor operates the calibration source position. The resolution of the positioning is about 1 mm.

3.3.2 Calibration source

Calibration source of inner calibration system is made by one of the collaboration institute, KRISS, in Korea [48]. There are two types of calibration sources, needle and flat types. The needle type is called as 4π source, and there are ^{57}Co , ^{241}Am source. The shape of needle source is shown in Fig. 3.7. The other type of sources, the flat type have ^{241}Am , ^{55}Fe , ^{109}Cd , and ^{137}Cs . They are called as 2π source. The shape of 2π source is shown in Fig. 3.8. Table 3.1 summarize the types and energy of calibration sources.

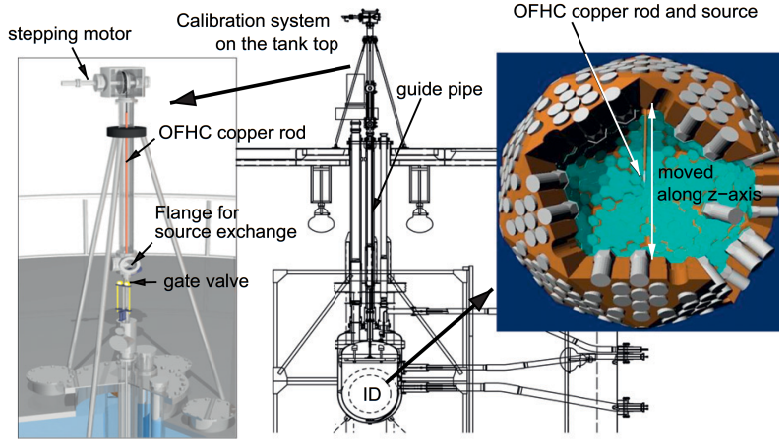


Figure 3.6: Calibration system of XMASS detector [15].

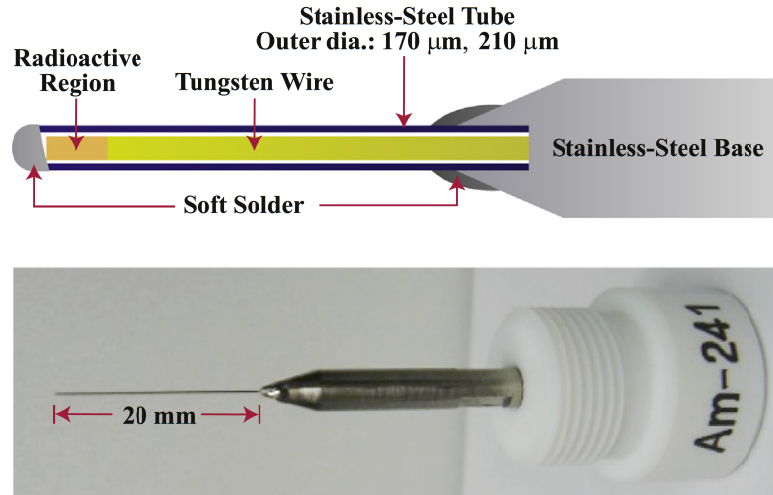


Figure 3.7: 4π (needle) calibration source [48].

3.4 Simulation

The Monte Carlo simulation (MC) code of the XMASS-I detector is based on Geant4. As shown in Fig. 3.9, the geometry of the PMTs and the detector are



Figure 3.8: 2π (flat) calibration source.

Type	RI	Energy (keV)
2π	^{55}Fe	[1.65],5.9
2π	^{109}Cd	(8),22,58,88
4π	^{241}Am	17.8,59.5
2π	^{241}Am	[30],59.5
4π	^{57}Co	(59.3),122
2π	^{137}Cs	662

Table 3.1: List of calibration sources for XMASS. Energy with parenthesis ”()” is for X ray from the material of source, and with block parenthesis ”[]” is for events accompanying escape X rays from a xenon atom.

accurately reproduced, and all scintillation photons generated are traced. For some parameters such as the optical parameters of LXe and the reflectance of the materials are tuned to reproduce the internal calibration data.

3.4.1 Al seal modeling

Based on the background study [30], main background component at low energy is due to the RIs in the Al seal of the PMT. Figure 3.10 show the fine structure around the Al seal and quartz window observed at the room temperature. There are a narrow gap between the quartz window of PMT and the Al seal of PMT. Although pure aluminum layer was deposited at the side of the quartz window as an optical barrier, inside the gap no aluminum layer was deposited. Because of this incompleteness of the optical barrier, there are some leakages of scintillation light caused by β ray and α ray emitted from the Al seal. Though the amount of this leakage of scintillation lights is subject to the fine structure of the gap, it is difficult to measure the fine structure at low temperature.

Because of this, the structures based on the pictures for several samples were measured, and two extreme models of BG were constructed for systematic error estimation as shown in Fig. 3.11. Figure 3.12 show the spectra caused

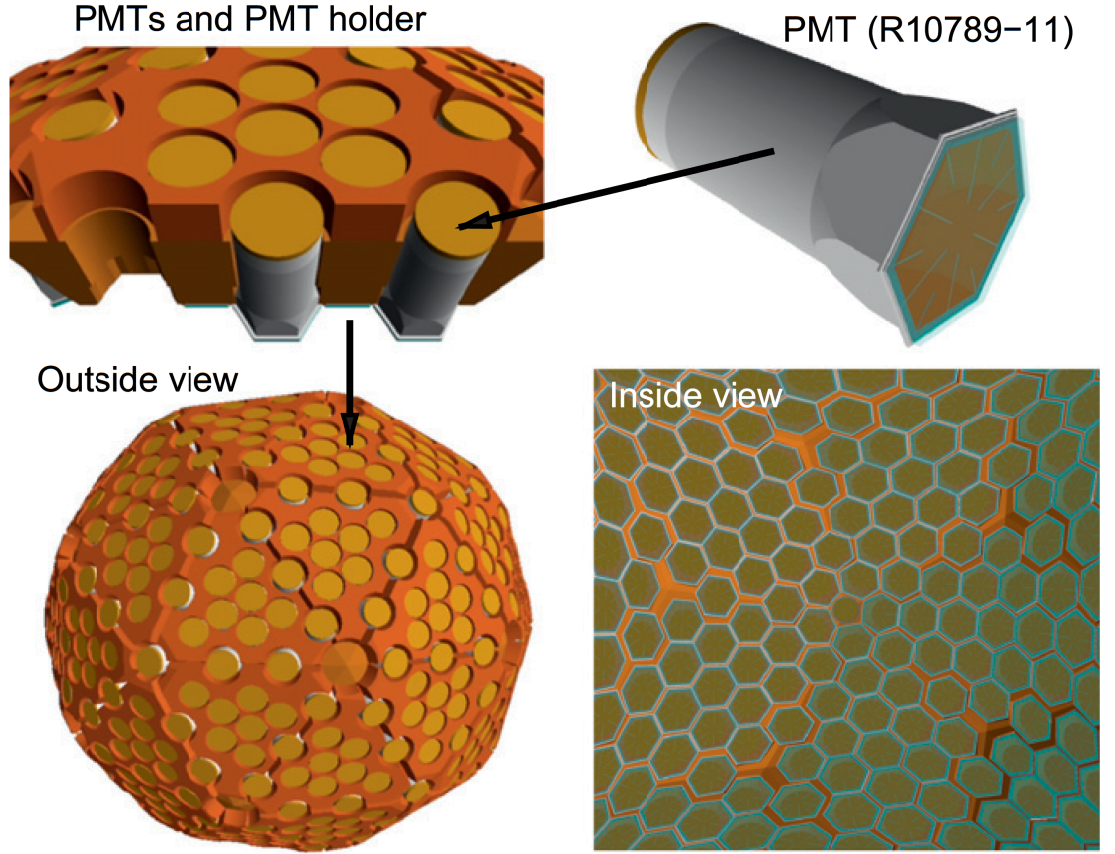


Figure 3.9: Geometry of XMASS-I detector simulation. After RFB, copper plate shield are installed [15].

by the RIs contained in the Al seal.

3.4.2 Scintillation yield of LXe

The scintillation efficiency for each deposited energy differs with the type of incident particles. The relative difference of the efficiency is considered for each particle as follows:

$$\alpha \text{ ray} \geq \gamma \text{ ray} > \text{nuclear recoil} \quad (3.3)$$

α rays have slightly higher efficiency of scintillation than that of γ rays. This is because of its higher density of ionization. Nuclear recoils have high density of ionization, but the total deposit energy in LXe is much smaller

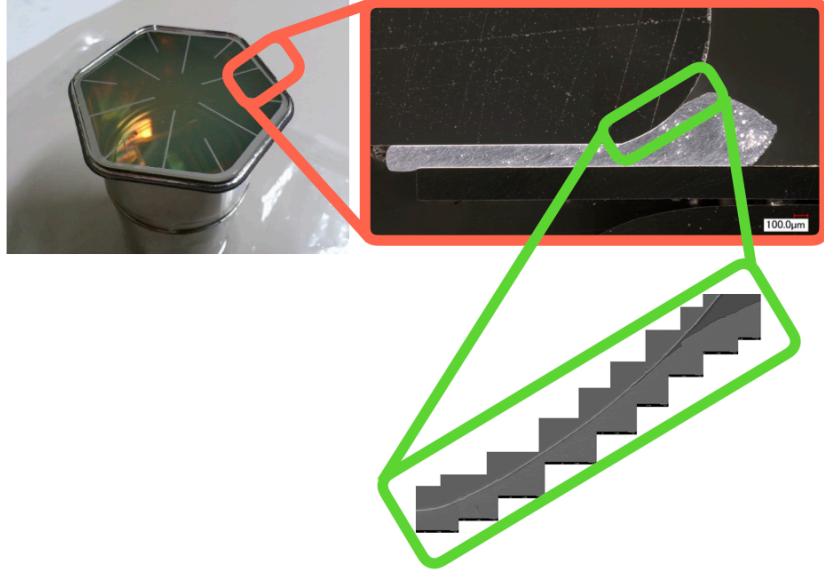


Figure 3.10: The photos around Al seal for one PMT. There is a narrow gap around the Al seal.

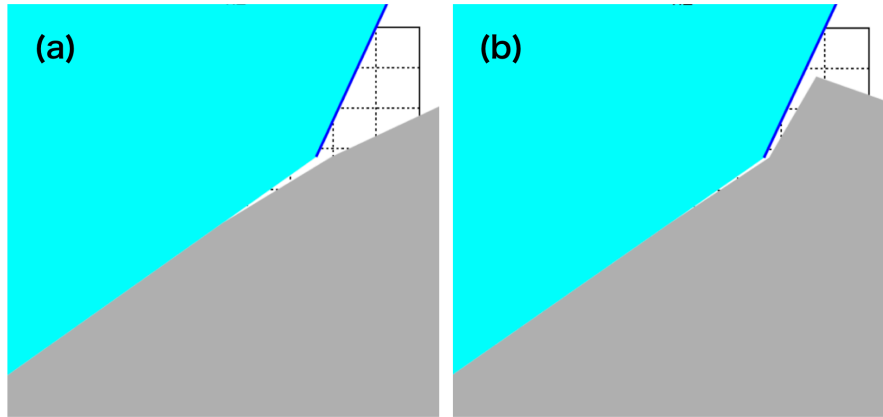


Figure 3.11: Two models of a gap around the Al seal of PMT. (a): a model based on an optical inspection at the room temperature. (b): a model in a case of construction of the Al seal under low temperature. Cyan part, grey part, and blue line represent the quartz window, Al seal, deposited aluminum layer, respectively.

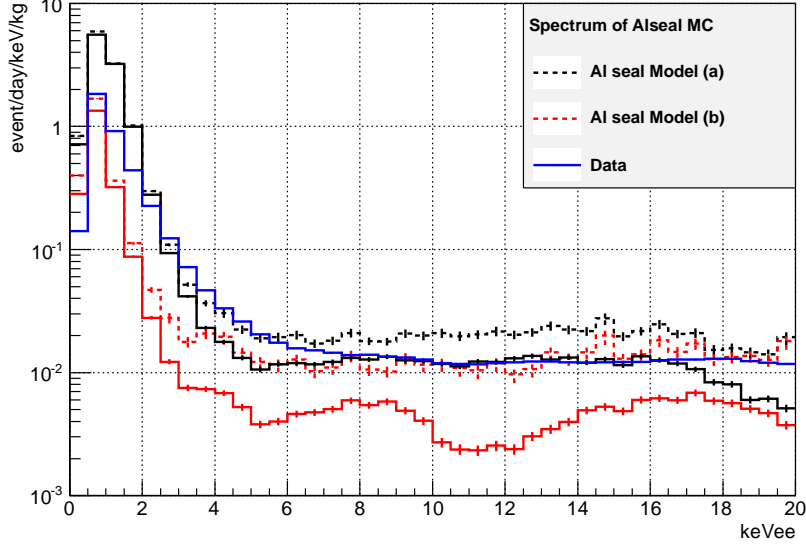


Figure 3.12: Energy spectrum caused by the RIs in the bulk of the Al seal. Black and red lines show the spectra of the shape (a) and (b) in Fig. 3.11, respectively. Dotted lines are spectra with other components. Blue line is observed data.

than α rays. These low energy nuclear recoils make collision with other Xe nucleus, and finally they produce heat. Because of that, the scintillation efficiency for nuclear recoil is much smaller than that for γ rays. The quench factor for this nuclear recoil, called L_{eff} , is calculated as below.

$$L_{\text{eff}} = \frac{\text{Scintillation yield induced by nuclear recoil}}{\text{Scintillation yield at 122keV } \gamma \text{ ray}} \quad (3.4)$$

Figure 3.13 [41], 3.14 [49] show the measured value of L_{eff} . In the previous studies [29] the curve shown in Fig. 3.13 is used. The curve below 3 keVnr in this figure is an extrapolation from high energy side. On the other hand in this study, more recent data given by the LUX experiment, shown in Fig. 3.14, are used below 3 keVnr.

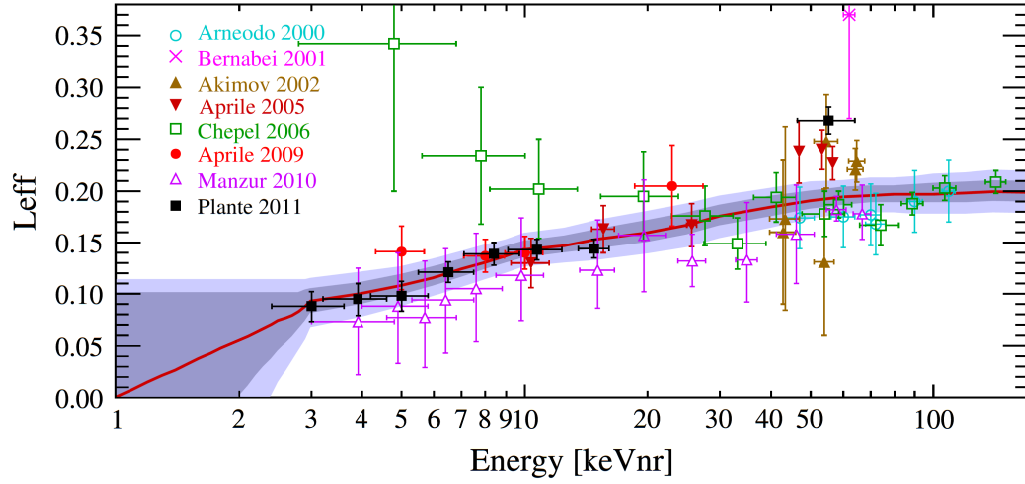


Figure 3.13: L_{eff} measurement above 3 keVnr.[41]

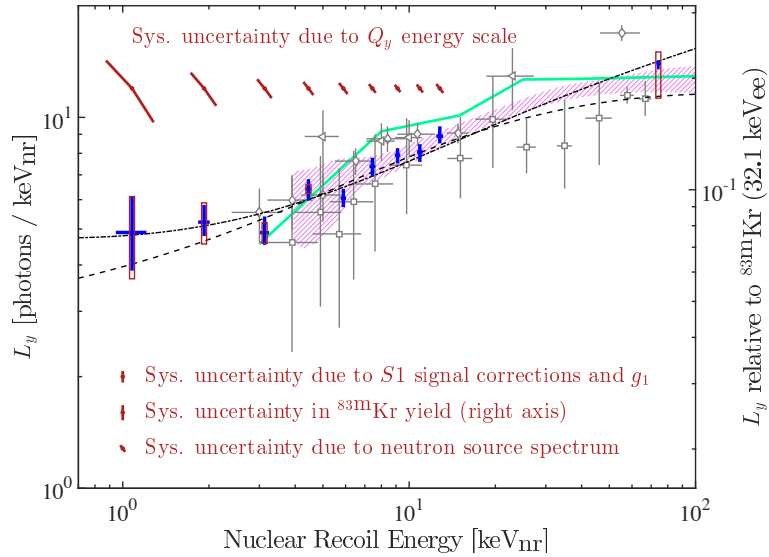


Figure 3.14: L_{eff} measurement by the LUX group including points below 3 keVnr [49]. Blue points are obtained by using mono-energetic neutron beam from a DD generator.

Chapter 4

Developments toward high sensitivity

4.1 Key ingredients to achieve high sensitivity

As already discussed in the Chapter 2, annual modulation of event rate is one of the unique characteristic observables caused by dark matter particles. To achieve the better sensitivity for dark matter such as WIMPs, improvements of hardware and software such as

- Lower energy threshold
- Larger exposure of data with stable condition
- Calibration for lower energy

are important. In this chapter, the actual developments to achieve better sensitivity are discussed.

4.2 Modification of electronics toward lower mass WIMP search

In the previous analysis on XMASS, trigger threshold of detector was set to be four hits of PMTs. The purpose of low threshold trigger is to lower the

energy threshold, by using three PMT hit events. To keep the event quality with the four hit threshold unchanged, following measures were implemented.

- Assigning the independent triggerID in addition to the normal threshold triggerID.
- Defining event timing with the normal threshold trigger for the case of presence of normal triggerID.

are needed. For the first measure, a low threshold trigger was installed as parallel circuit with normal trigger circuit, and a new triggerID for the low threshold was newly assigned as shown in Fig. 4.1.

As already discussed, the global trigger of XMASS-I is based on the height

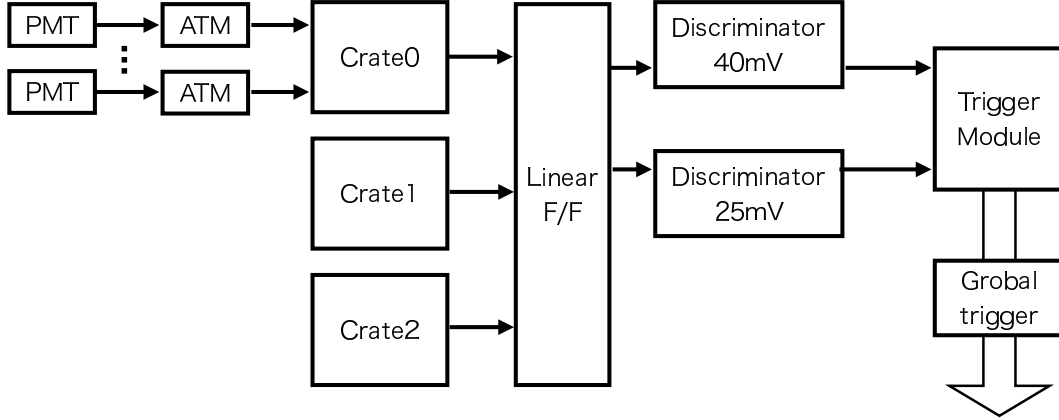


Figure 4.1: Simplified trigger flow with low threshold trigger

of an analog square waveform, called HITSUM. HITSUM has a pile up signal of a square waveform with 11 mV height and 200 ns width. HITSUM from ATM are summed up in 3 crates individually, then those output signals are summed up again with a Linear FAN-IN FAN-OUT (Linear F/F) module and the final output is sent to a discriminator. To implement the low threshold trigger, the output of the Linear F/F is sent to both of discriminators for the normal threshold (-40 mV from baseline) and the low threshold (-25 mV from baseline) trigger. So, the normal threshold events have both of the normal threshold triggerID and the low threshold triggerID. By picking up events with the normal threshold trigger bit, data with four hit threshold can be collected.

The second measure is important to keep data quality with four hit threshold

unchanged. Because HITSUM is analog signal, timing of the low threshold trigger comes faster than that of the normal threshold. This makes the event timing to be determined by the low threshold trigger. To avoid this shift of timing relative to the normal threshold, a 110 ns of timing delay was installed for low threshold trigger circuit. Figure 4.2 shows the relationship of the timing of each trigger line. This timing delay was made by installing a long cable with length of 22 m. Because of this delay, event with the normal trigger timing is determined by the normal trigger timing irrespective of any presence of the low threshold trigger signal. Even in this case the triggerID for the low threshold events can still be assigned, because the delay is smaller than the timing window of TRG module, 150 ns. The level of discriminator

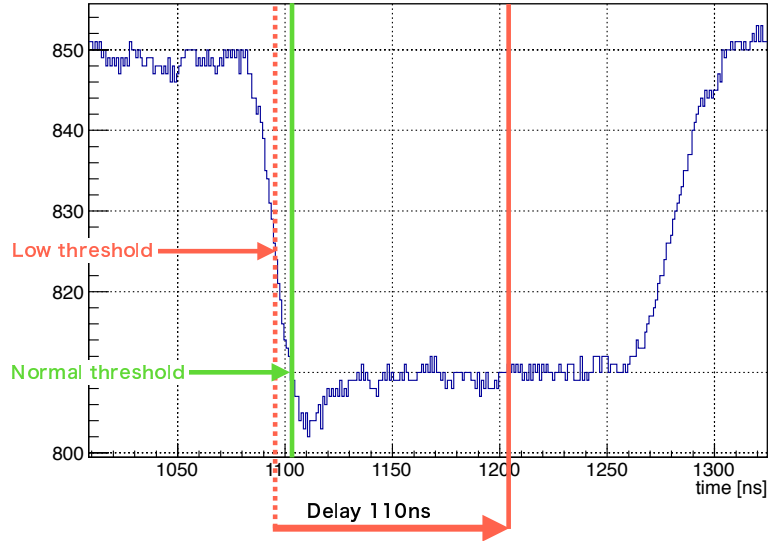


Figure 4.2: A schematic view of the timing delay of low threshold trigger for the HITSUM waveform.

for the low threshold trigger is set to 25 mV, to take three hit events.

4.3 Identification of noise events in the low threshold data

4.3.1 Weak flashing of PMTs

From a study of afterpulses of PMT R10789 [50], it is known that there is a weak flashing after the amplifying photoelectrons. One of the possibilities of

this flashing is the discharge close to the anode of PMTs. This weak flash occur with 0.3 - 1.0% probability for single photoelectron, and have 40-50 ns timing delay from the injected photoelectron. Figure 4.3 show the schematic view of the flashing. This delay comes from the transit time of the PMT R10789. In this thesis we argue that this weak flash lights go outside of initial PMT and make hits in other PMTs. This weak flashing phenomena was not observed for the analysis with the normal threshold data, but become serious problem for analysis with the low threshold data.

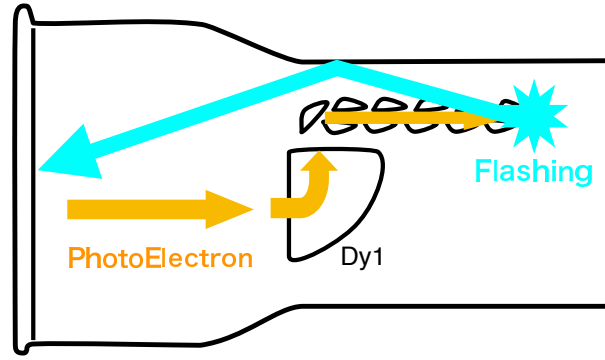


Figure 4.3: Schematic view of PMT flashing.

4.3.2 Properties of flasher events and event selection

Since this flashing cause three hit events, change of single rate of PMT affects the event rate of three hit events. This needs to be avoided to realize stable data analysis. To remove the three hit events caused by this weak flash, a data selection was established as follows.

Clock trigger data for investigating the flasher events

To investigate properties of PMT flasher, random trigger events are needed. For that purpose, a special clock trigger run was taken. Frequency of the clock was 500 Hz, and each events have $7.5 \mu\text{s}$ time window. Total livetime of this clock run was 31.02 second. Using two hit event obtained in this clock trigger run, an angular distribution and time distribution were measured. Figure 4.4 (a) shows the timing difference of 1st and 2nd hit PMT of two hit events. This timing distribution have clear peak around 50 ns. Figure 4.4 (b) shows the angle distribution around the peak in the Fig. 4.4 (a). This figure

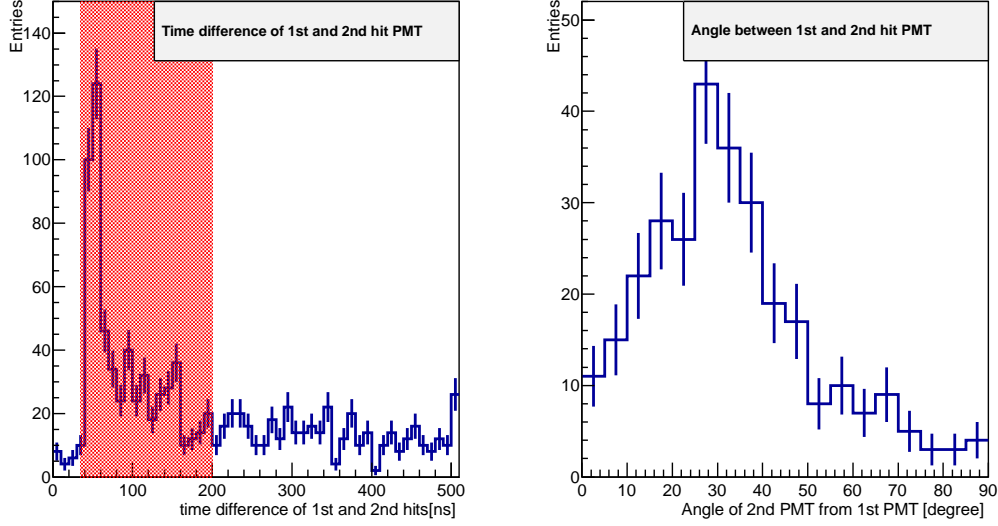


Figure 4.4: Distribution of (a):timing, and (b):angle between 1st hit and 2nd hit PMT of two hit events. Angle was calculated by using red hatched region of time distribution.

shows the angle between 2nd hit PMT and 1st hit tend to have angle smaller than 50 degrees. By using these distributions, selection criteria would be (1) time difference is more than 35 ns and (2) angle between hits are within 50 degrees. All combinations of two PMTs are examined in each three hit event. If a certain event have at least one pair of PMTs recognized as a flasher, that event is removed as a flasher event.

4.4 Energy scale calibration at low energy

As nuclear recoils were described in Sec. 3.4.2, number of photons created by electron and γ rays are also not a linear function of the energy as well. Especially at lower energy such as around a few keV, it generates less number of photons than that at higher energy in unit energy. By using the calibration sources of the XMASS-I detector in Sec. 3.3.2, these energy non-linearities are measured. The lowest energy of calibration for electron recoil performed by us is the L-shell escape peak using a ^{55}Fe source. X ray from the ^{55}Fe source have energy of about 5.9 keV. After absorbed by the L-shell electron,

sometimes a fluorescence X ray with various energies about 4 keV go back to the housing of the ^{55}Fe source. In this case, only remainings, such as L-shell electron or Auger electrons, are observed. Their energies distribute at 1.2 - 2 keV, and the weighted mean energy is 1.65 keV. Including other experiments using liquid xenon, no calibration of the response for electron recoil event below 1 keV exists. Because of these situation the number of generated photon below 1 keV is assumed to be zero for conservative evaluation of signal. Figure 4.5 shows the distribution of the number of PEs for the escape peak. Solid blue and red histograms are observed data and MC around the escape peak. Green line shows the expected tail component from the 5.9 keV peak. Dotted red histograms is the distribution only the for escape peak. The tail component is caused by the geometry of the source. Because of the uncertainty of the tail component, it was also modeled with parameters and fitted simultaneously. Dotted red histogram is simulated result for the process described above considering non linear effect, and then sum of the tail and the peak is compared to the distribution of the data.

The cutoff at the low energy side is partly due to the trigger threshold and may affect the peak position. To compensate this uncertainty, the ratio between the number of events in the 5.9 keV peak and the escape peak is constrained by the simulation with appropriate uncertainty and thus the position of the escape peak is determined with an uncertainty shown in Fig. 4.5. Figure 4.6 shows the non-linearity observed in Data and MC at calibration points. They are normalized at the point of 122 keV γ ray from ^{57}Co . Other points show the response to γ rays from calibration sources. Simulation of the XMASS-I detector is generating the number of photons with initial model of non-linearity, but the real response between the data and calibration points differs. As Fig. 4.6 is showing, MC generates too much number of photon for each gammas without any correction of the generation of photons for simulation. The black line in the figure is the best fit for the distribution with a log-polynomial function. Hatched region show the error points of fitting. Then, a correction to the initial model of non linearity is applied based on this function. Fig. 4.7 shows the result of the correction in MC based. All calibration points are consistent within the band of uncertainty.

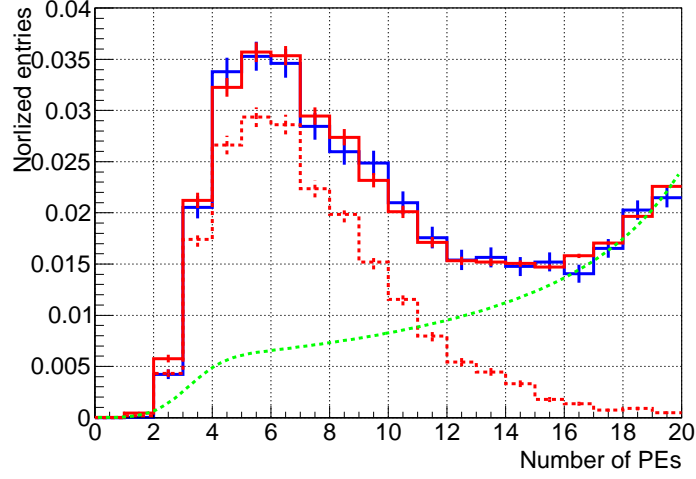


Figure 4.5: PE distribution for the escape peak. Solid blue and red histograms are showing the observed data and MC. Dotted red histogram and green line are showing the best fit result for the escape peak component and tail component from the 5.9 keV X ray.

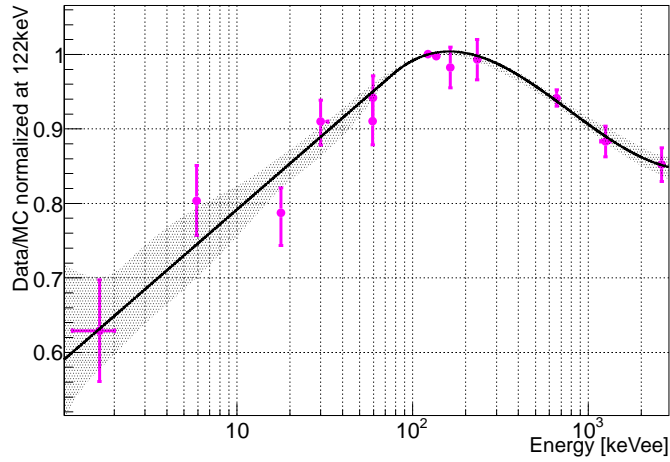


Figure 4.6: Comparison between data and MC for each peaks of γ ray from each calibration sources. Magenta points are Data/MC normalized at 122 keV. Black line and hatched regions are showing the best-fit function and its error bands.

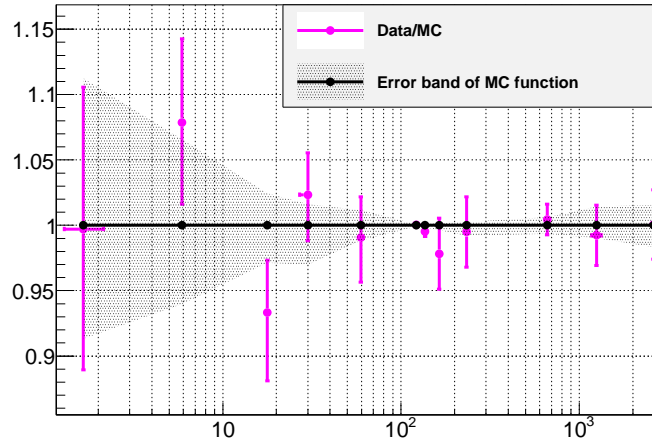


Figure 4.7: Comparison between data and MC for each peaks of γ ray from each calibration source with the correction to the non linearity. Magenta points are Data/MC normalized at 122 keV. Black line and hatched regions are showing the band of uncertainties.

Chapter 5

Data set and reduction

5.1 Summary of the data set

The data set used for this study is shown in Table 5.1. In the analysis of this thesis, dark matter run data from November 20th, 2013 to June 20th, 2017 are used. The data with low threshold trigger was introduced on December 8th, 2015. Total exposure is two times larger than that of DAMA/LIBRA (1.04 ton year) with the normal threshold trigger.

Type	Start	End	Calender days [day]	Livetime[day]	Exposure [ton year]
Normal	Nov. 20th 2013	Jun. 20th 2017	1308.0	1045.0	2.38
Low	Dec. 8th 2015	Jun. 20th 2017	560.0	276.7	0.63

Table 5.1: Summary of the data set.

5.2 Run selection and binning

5.2.1 Run selection for the normal threshold runs

To select good dark matter run, following conditions are required.

- No problematic DAQ modules
- No significant noises in the data

- Stable condition of detector during the run (temperature is stable within ± 0.05 °C and pressure is stable within ± 0.0005 MPa)
- Stable ID/OD trigger rate of ID/OD trigger rate during the run

Standard temperature and pressure of the detector are -100.1 °C and 0.1624 MPa, respectively. To monitor the temperature stability, three sensors attached to the detector are used. For example, all of three sensors are needed to be stable within ± 0.05 °C to pass the selection.

5.2.2 Run selection for the low threshold runs

For the low threshold run, the change of the single rate of PMTs and PMT flashing affect the trigger rate stability significantly as described Sec. 4.3. To suppress the systematic change of event rates due to them, following two conditions are required to pass the run selection:

- Single rate for each PMT is within ± 500 Hz or less than 2.5σ deviation from a standard rate
- Sum of single rates of PMTs is within ± 500 Hz or less than 2.5σ deviation from a standard rate

Since these conditions depend on event statistics, at least five hours and two days of livetime are required for the first and the second condition, respectively. If necessary consecutive runs are merged so that these conditions meet. For some of periods, livetime for low threshold is shorter than that of normal runs. They are caused by the change of single rate for some number of PMTs. This will be discussed in next section, 5.2.3.

5.2.3 Time binning

Runs with good condition are divided into the 86 periods. The start and end of each period are determined so that two periods are assigned to each month; early 15 days and late 15 days. Low threshold data taking started in December 2015, and there are 32 periods. Figure 5.1 (a) shows the live time of each period of normal threshold and low threshold data. Horizontal axis is the time from the January 1st of 2014 and each point shows each period. The shorter live time for low threshold run than normal threshold run is caused by the criteria for single rate stability discussed in Sec. 5.2.2. Figure 5.1 (b)

shows the total single rate for each period. Figure 5.1 (c) shows the number of PMTs with single rate more than 100 Hz. Xenon distillation work was conducted during the term from January 10th to February 8th and some of PMTs became high rate after that work as Fig. 5.1 (c) shows. Because of that, livetime for low threshold run is short around 1100 - 1200 days in the plot. Other low threshold periods with shorter livetime are coming from the change of single rate for unstable one or a few number of PMTs in short time. The single rate of some typical unstable PMTs, ID 316, 445 and 594 before the run selection for low threshold run, are shown in the Fig. 5.1 (d). The single rate of some typical stable PMTs, ID 72, 105 before the run selection for low threshold run, are shown in the Fig. 5.1 (e). Corresponding calendar months of each period and threshold are shown in Fig. 5.2.

5.2.4 Energy binning

In this thesis, energy is expressed in the unit of the electron equivalent energy. Since all of our calibration data is taken with γ ray sources, simulations are necessary to extract the non-linear relationship between observed photoelectrons and the electron equivalent energy. This non-linearity curve is tuned to explain our calibration data, as discussed in Sec. 4.4. Figure 5.3 shows the conversion of scaled number of PE to keVee. Each black point shows the mono energetic simulation of electron. The vertical axis is the electron equivalent energy. The horizontal axis is number of PE scaled by the light yield at 122 keV γ , 15.5 PE/keV. The red line is the fitted function for the distribution.

Even the function is extended below 1 keV, it is an extrapolation because no calibration points are existing including the measurement of other experiments. Therefore only the data above 1 keVee is used for the analysis of bremsstrahlung spectrum and model independent amplitude fitting. On the other hand, energy bin below 1 keVee can be used for the analysis with nuclear recoil based on the quench factor measured by LUX group [49]. This threshold was determined by evaluating the trigger efficiency of the low threshold data of WIMP simulation. To keep 50% trigger efficiency for 4 GeV WIMPs, 2.3 keVnr (0.5 keVee) was selected for the analysis of nuclear recoil.

Error for the non-linear energy conversion function is based on the energy scale function discussed in Sec. 4.4. At 1 keVee, the error for energy conversion is +22% and -14%.

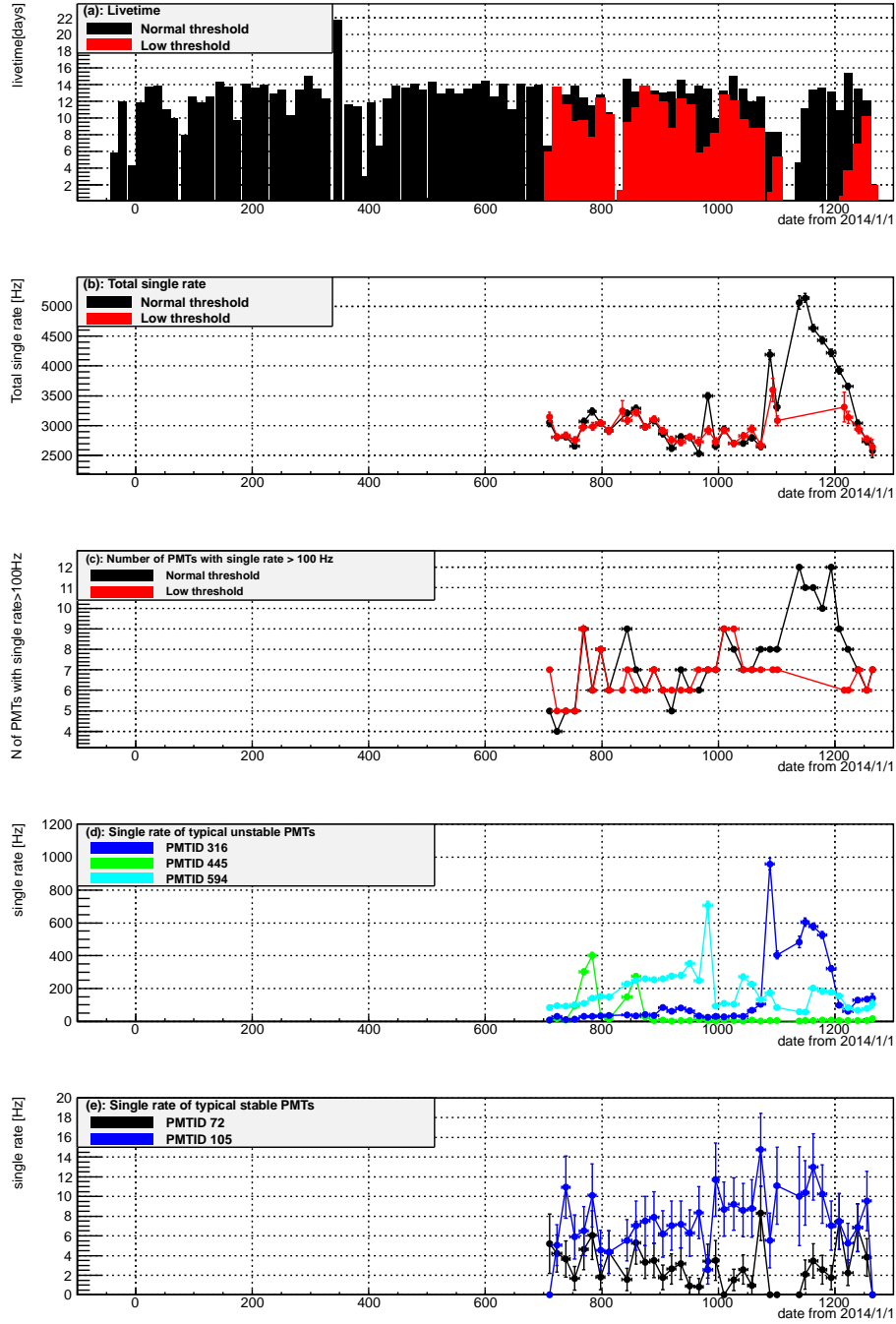




Figure 5.1: (a):Livetime, (b): single rate of total detector, (c): number of PMTs with single rate more than 100 Hz, (d): the single rate of typical unstable PMTs, and (e): the single rate of typical stable PMTs. For (d) and (e), run selection for low threshold run is not applied. Each point shows the each period.

Year		2013	2014	2015	2016	2017				
Month										
Jan	early		3		2	52	26	75		
	late		4		25-28	3	53			
Feb	early		5		29	4	54		76	
	late		6		30	5	55		77	
Ma	early		7		31	6	56		78	
	late		8		32	7	57		79	
Apr	early		9		33	8-9	58		80	
	late		10		34			27	81	
May	early		11		35	10	59	28	82	
	late		12		36	11	60	29	83	
Jun	early		13		37	12	61	30	84	
	late		14		38	13	62	31	85	
Jul	early		15		39	14	63			
	late		16		40	15	64			
Aug	early		17		41	16	65			
	late		18		42	17	66			
Sep	early		19		43	18	67			
	late		20		44	19	68			
Oct	early		21		45	20	69			
	late		22		46	21	70			
Nov	early		23		47	22	71			
	late		0		24	48	23	72		
Dec	early		1		25-28	0	49-50	24	73	
	late		2			1	51	25	74	

: Normal thershold

: Low thershold

Figure 5.2: Year and month for each period. Yellow and Green columns are showing the period with normal threshold and low threshold, respectively.

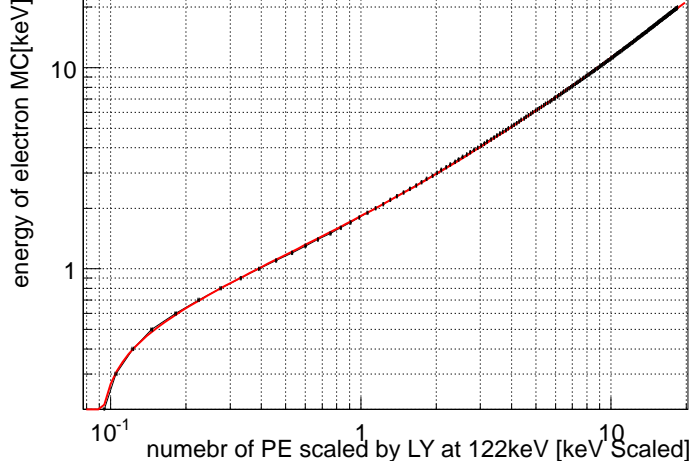


Figure 5.3: The non-linear energy conversion function. Black points are mono energetic electron MC, red line is fitted function. Horizontal axis is the number of PE scaled by the light yield of 122 keV γ , the vertical axis is the energy of electron.

5.3 Data reduction

There are following five steps in data reduction.

5.3.1 Noise cut

Purpose of this noise cut is to remove events caused by electric noise. Since signal from PMT is negative, events with large positive signal, more than 0.1 PE/ns, are rejected. Also, events during bad condition of modules (ATM periodical calibration, FADC event header failure, etc) are rejected.

5.3.2 Afterpulse cut

After a bright event such as caused by a cosmic muon, many one PE level afterpulses are observed. These afterpulses sometimes create another event. This is called as an afterpulse event. To cut these afterpulse events, two cut referred as to the dt cut and timing RMS (trms) cut are used. Since these 1 PE level afterpulses continue for a few ms timescale, 10 ms software veto time is set after each events. This is called as dt cut. Livetime of the detector is calculated considering the dt. Livetime is calculated by counting the number

of GPS 1 PPS signal, and the GPS pulses during the veto time by dt cut are not counted. In addition to the dt cut, a cut based on randomness of afterpulse timing is applied. Since these 1 PE afterpulse arrives randomly in FADC time window, root mean square of pulse timing becomes larger than the scintillation events. Trms less than 100 ns is required to pass afterpulse cut. Figure 5.4 show the distribution of dt and trms. There are events with short dt and large trms, caused by afterpulses.

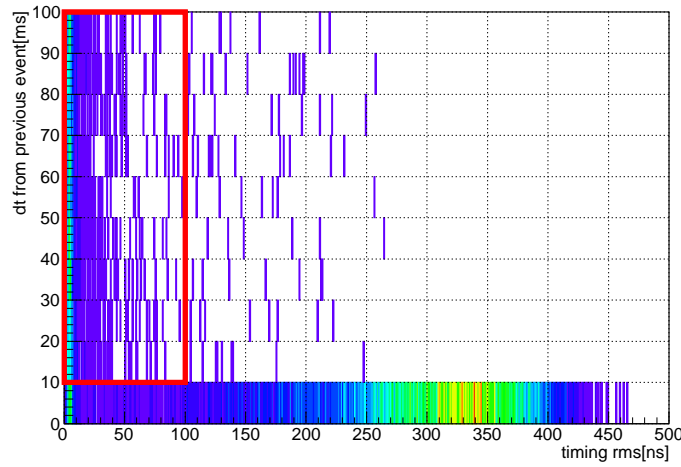


Figure 5.4: Dt and trms distribution observed in a dark matter run. Events with short dt less than 10 ms or large trms more than 100 ns (outside red box) are caused by afterpulses and removed by the cut. Events inside the box pass this cut.

5.3.3 flasher cut

This cut is applied only for events with three hits. This cut is applied to remove events caused by weak flashing of PMTs. See details in Sec. 4.3.

5.3.4 cherenkov cut

This cut is used for removing events caused by cherenkov lights. β rays from ^{40}K in the photo cathode of PMTs, or from the radioactive decay of U, Th chains can produce cherenkov photons in a quartz window of a PMT. This cherenkov photons have small photon yield and fast timing profile of

emission. To cut these events, a head-total ratio of the number of PMT hits is used. The head-total ratio is calculated by the number of PMTs in first 20 ns, divided by the number of PMTs in a total time window of analysis (300 ns). If this ratio cherenkov parameter is more than 0.6, that event is cut as a cherenkov event. Because three hit events have only three possible values (1.0, 0.66 and 0.33), events with the head-total ratio 1.0 are rejected.

5.3.5 likelihood cut

All cuts discussed above are called as a standard cut. After the standard cut, this cut is applied. For the analysis of a low energy region ($E < 2$ keV), a reconstruction algorithm based on PE pattern doesn't work well. Because of this, this cut to improve S/N was developed. This cut consists of three parameters calculated based on observed PEs: max/Total PE ratio, Sphericity and Aplanarity of the PE distribution. To distinguish the signal and background, two types of MC, uniform and wall (generated in radius more than 38cm from center and at the inner surface of the detector) distributed electron simulation are used. A likelihood function L is calculated as

$$L_i = \prod_j^{Npar} F_{ij}(q), \quad (5.1)$$

where, q is number of PEs, and $F_{ij}(q)$ is a probability density distribution. The index j represents each parameter (j = Max-to-total ratio, sphericity, aplanarity), and i represents the index for the spacial difference of event vertices of simulation (i = uniform, wall).

Sphericity and Aplanarity

Sphericity and aplanarity are calculated by a tensor of detected PE squared and position of each PMT. Definition of sphericity tensor T_{ij} is

$$\begin{aligned} T_{ij} &= \frac{\sum_{\alpha}^{NPMT} q_{\alpha,i} q_{\alpha,j}}{\sum_{\alpha}^{NPMT} q_{\alpha}^2}, \\ q_{\alpha,i} &= q_{\alpha} n_{\alpha,i}, \end{aligned} \quad (5.2)$$

where α specifies one of ID PMT, q_{α} is detected number of photoelectrons in PMT α , $n_{\alpha,i}$ shows i -th component ($i = 1, 2, 3$ correspond to x, y and z,

respectively) of a unit vector pointing from the center of the detector toward the PMT α , respectively. Then, 3 eigenvalues can be calculated by viewing T_{ij} as 3×3 matrix. The sphericity S and aplanarity A can be calculated by using these values, $\epsilon_1 \geq \epsilon_2 \geq \epsilon_3$, as

$$S = \frac{3}{2}(\epsilon_2 + \epsilon_3), \quad (5.3)$$

$$A = \frac{3}{2}(\epsilon_3), \quad (5.4)$$

Sphericity and aplanarity are the measures of how closely the hit distribution resembles a sphere or a plain, respectively. For example, if hits in an event distributes uniformly, $S=1$ and $A=0$. If hits are concentrated on a plain, $S=0$ and $A=1$.

Max-to-total ratio

In addition to the sphericity and aplanarity, the max-to-total ratio parameter is used. This parameter is calculated as

$$M = \frac{\text{Max}(q_\alpha)}{\sum_\alpha q_\alpha} \quad (5.5)$$

$\text{Max}(q_\alpha)$ represents maximum photoelectron among q_α . In Fig. 5.5, distribution of each parameters at 2 keV are shown.

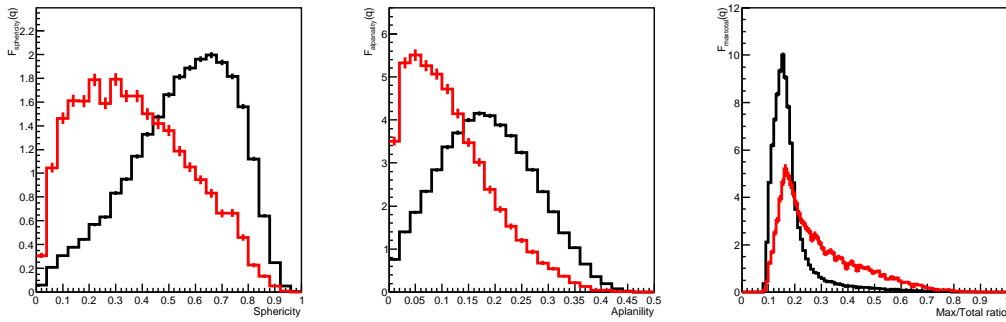


Figure 5.5: Probability density function of Sphericity, Aplanarity and Max-to-total ratio parameters around 2 keVee. Black histogram shows the distribution of uniformly distributed events, and red shows the distribution of events around the wall.

Log likelihood

As indicated in Eq. 5.1, the cut criteria is defined by the log likelihood ratio using three parameters described above. For uniform electron events, criteria for $\log L_{\text{uniform}} - \log L_{\text{wall}}$ to keep 50% efficiency for events after all cuts above are calculated for each PE range. By calculating the log likelihood ratio for each events of data, and the event with larger likelihood value than criteria are reduced by this cut. In the Fig. 5.6, log likelihood distribution for uniform electron MC at 2 keVee is shown. The remaining fraction of the wall events is 16% for this energy.

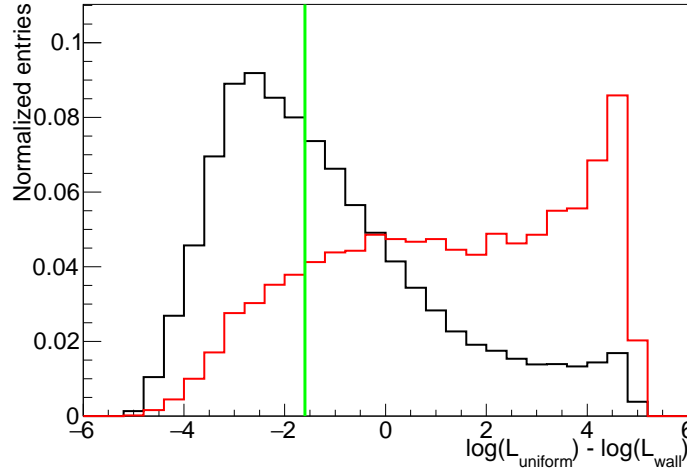


Figure 5.6: Log likelihood distribution for uniform electron MC. Black is the distribution from uniform, and red is the distribution around the wall. Green line is the cut value for this energy, 2 keVee.

Figure 5.7 show the energy distribution of the observed data. Black, red, green lines are showing the spectrum after no cut, after standard cut and after standard plus likelihood cut.

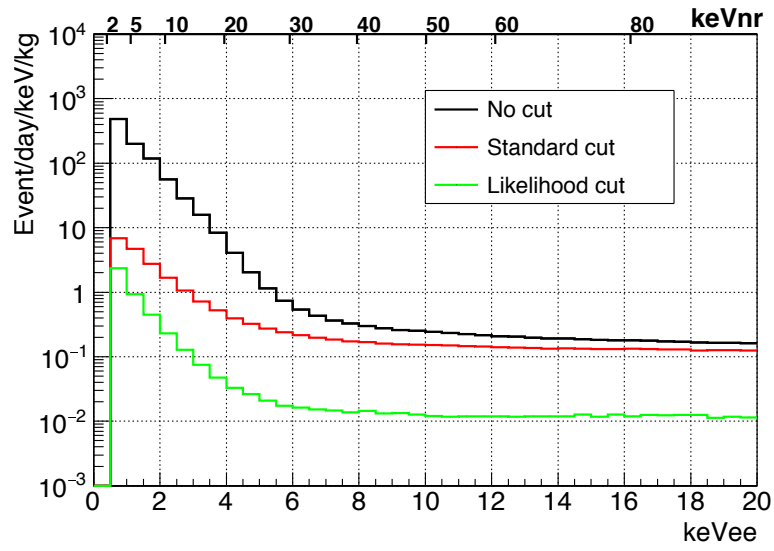


Figure 5.7: Energy spectrum of the data. Black, red, green lines are showing the spectrum after no cut, after standard cut and after standard plus likelihood cut.

Chapter 6

Systematic errors and error estimation

6.1 Systematic errors in the real data analysis

The origins of systematic errors in event rates of real data are listed as follows:

- Stability of Light Yield of the detector
- Stability of electronics
- Event rate fluctuation from weak flashing of PMT

Each of them will be discussed in this chapter in detail.

6.1.1 Stability of Light Yield of the detector

Monitoring light yield stability

To monitor the light yield, 122 keV γ peak of a ^{57}Co source was used. Figure 6.1 shows the PE spectrum of the ^{57}Co source. In Fig. 6.2, the change of light yield at 122 keV γ rays is shown. The change of the light yield is identified to originate from the change of the amount of impurities that absorb scintillation lights in LXe. Xe in the XMASS-I detector was purified using hot metal getters before introducing to the detector. However, after the introduction, no circulation was performed. It is considered that impurities existing in the detector were gradually trapped at the cryocooler and the

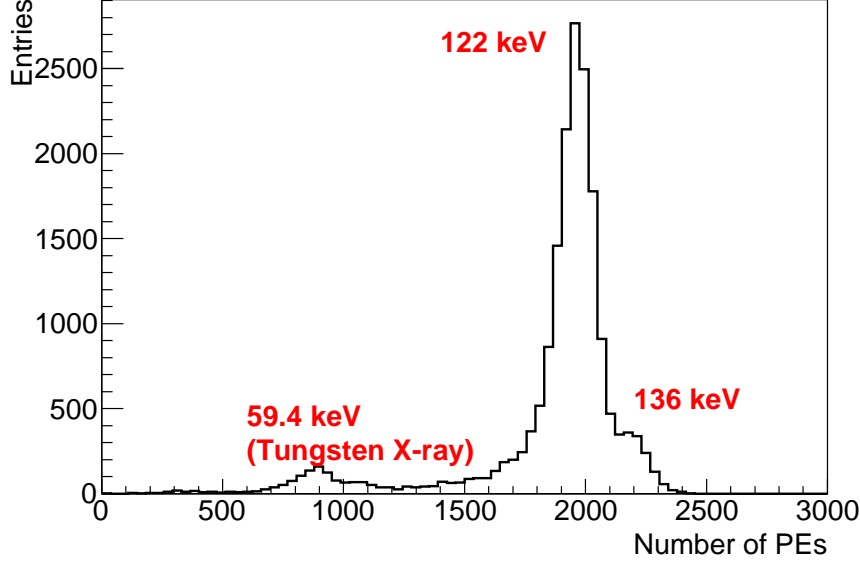


Figure 6.1: Number of PE spectrum of the ^{57}Co source. 122keV, 136 keV γ rays was emitted from the decay of ^{57}Co . Tungsten of the source structure emits 59.3keV X-ray.

light yield of the detector increased at the first nine months of the XMASS operation.

In August 2014, there were a sudden change of the light yield. At that time, there was a power outage and the cryocooler stopped. Warming up the cryocooler released the impurities which were trapped before. Also, LN2 was supplied through tubes attached to the wall of LXe chamber to avoid increase of pressure. This made the temperature of detector lower than the usual. Impurities released from the cryocooler could go into the detector at that time. This decrease of the light yield was stopped by the gas purification and maintenance of the cryocooler on Jan 2015. After that maintenance, recirculating gas purification started to remove impurities. After the recirculating gas purification, light yield became stable.

The period of low threshold data taking is indicated by the arrow in Fig.6.2. In this period, light yield change was small and stable. A small change around October 2016 was originated from a test of gas circulation condition. A change around the February 2017 was originated from the distillation work of LXe. However changes of light yield from these works are only 1 or 2%,

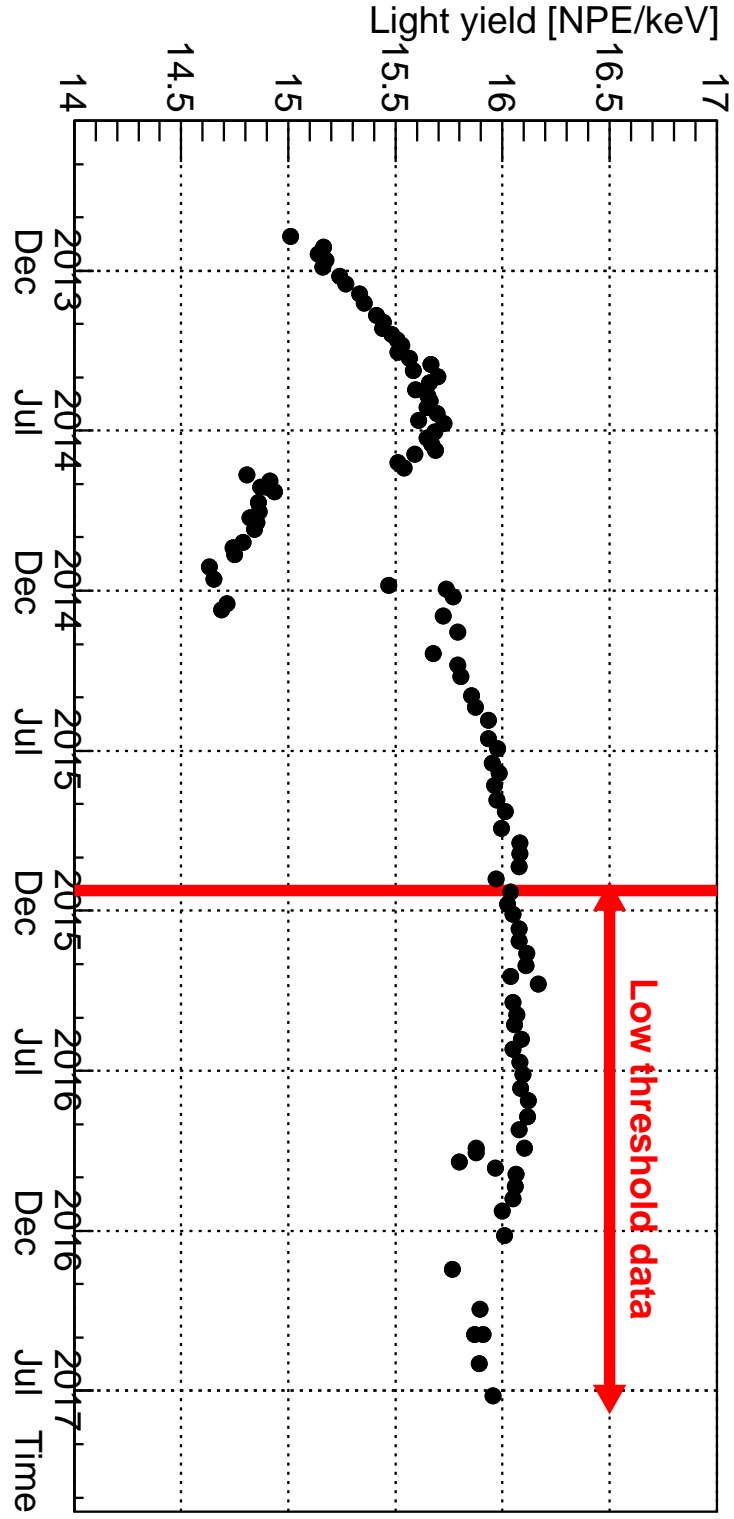


Figure 6.2: Change of light yield of 122 keV γ rays. Vertical axis is in the unit of number of PE divided by energy of γ ray in keV.

much smaller than that at the power outage, about 6%.

Parameter estimation by simulation

Calibration data taking with a ^{57}Co source is performed every few weeks. Using calibration data at seven positions ($\pm 30\text{cm}$, $\pm 20\text{cm}$, $\pm 10\text{cm}$, 0cm), optical parameters, absorption length, scattering length, intrinsic photo yield of LXe are obtained by fitting data with simulated data. They were obtained by a χ^2 minimization. χ^2 function to obtain the parameters is

$$\begin{aligned}\chi^2 &= \sum_{z(\text{source})} \chi_{NPE}^2(z) \\ \chi_{NPE}^2(z) &= \sum_i^{NPMT} \frac{(N_i(\text{Data}) - b \cdot N_i(\text{MC}))^2}{\sigma_i^2},\end{aligned}\quad (6.1)$$

where N_i is mean number of PEs for each PMT i , and σ_i is the quadrature of the statistical and systematic errors.

$$\sigma_i^2 = N_i(\text{Data})/N_{\text{events}}(\text{Data}) + b^2 \cdot (N_i(\text{MC})/N_{\text{events}}(\text{MC}) + \sigma_{\text{sys}}^2). \quad (6.2)$$

MC data samples with various absorption and scattering lengths are generated. The intrinsic light yield is considered as the parameter b in the χ^2 function. From this fittings, the change of the light yield is understood by the change of the absorption length. The best fitted parameters for each calibration are shown in Fig. 6.3.

Change of efficiency for each period

Change of light yield make the change of spectrum shape in two of aspects. One is the distortion of spectrum caused by the change of transparency. The other is the change of cut efficiency for each energy. These changes can make the systematical change in event rates. To correct the effect of them, the relative change of the spectrum is calculated based on the background MC simulations with Al seal and other components with uncertainty. Hereafter, relative efficiency is defined as the ratio between an event rate at a certain light yield period and the one at a fixed period, i.e.,

$$\text{Eff}(\text{LY}, E_{\text{corr}}) = \frac{R(\text{LY}, E_{\text{corr}})}{R(\text{LY}_0, E_{\text{corr}})}, \quad (6.3)$$

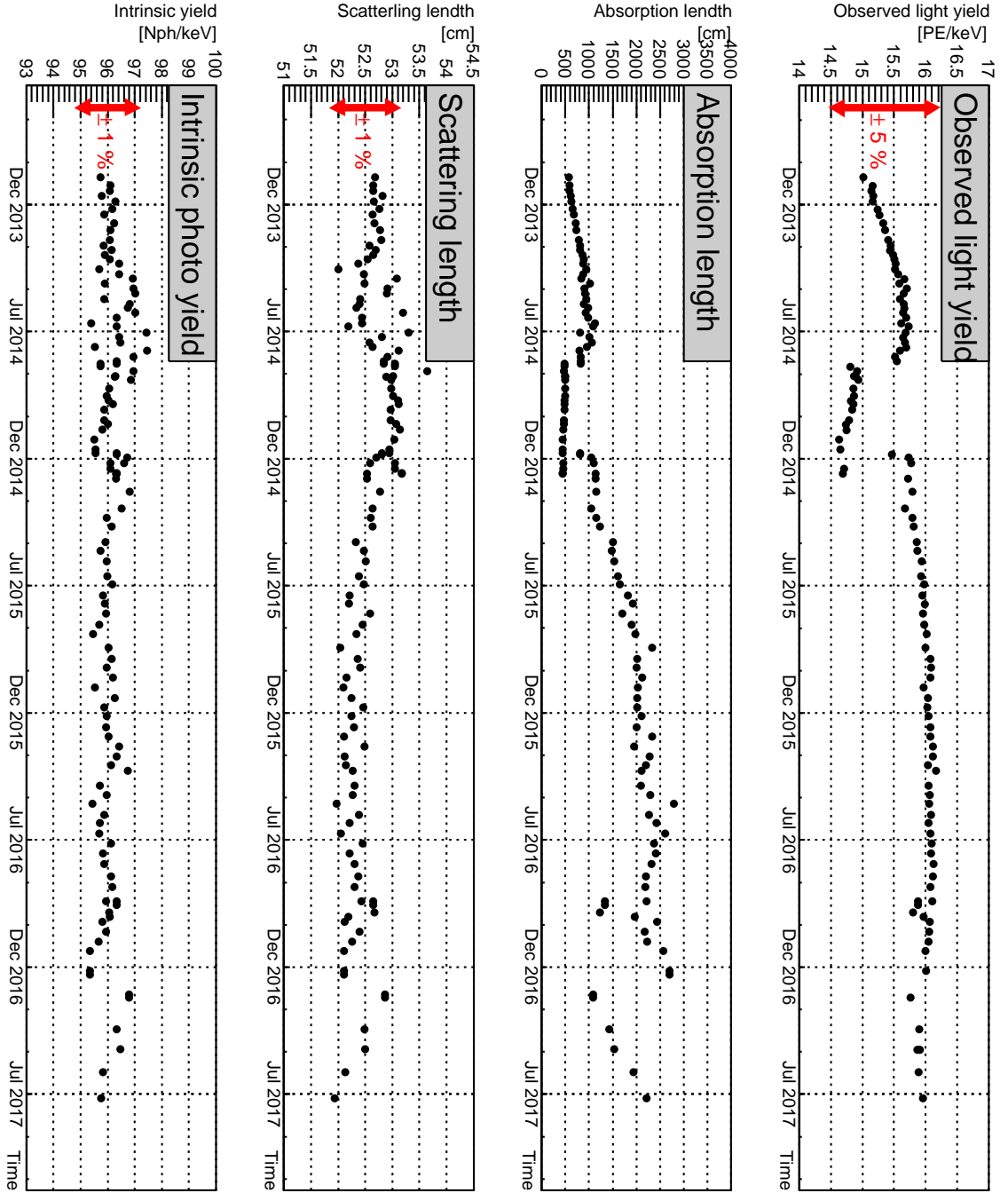


Figure 6.3: Optical parameters obtained through a fitting with MC samples. Changes of the light yield are explained to the change of absorption length.

where LY, LY₀, E_{corr} and R indicate light yield at a certain period as shown in Fig. 6.2, light yield at February 2014, electron equivalent energy corrected by the light yield of each periods discussed in Sec. 5.2.4, the event rate after the data reduction by background MC simulations. The relative efficiency curves for each energy are shown in Fig. 6.4. These efficiency curves are calculated as a function of light yield with uncertainty as described in following paragraph.

Because heavy CPU consumption is required to estimate the curves, they are calculated for 0.5-1, 1-2, 2-6, 6-20 keV merged bins. The uncertainty of shape of Al seal, discussed in the Sec. 3.4.1, introduces the largest uncertainty of relative efficiency calculations. The MC with different light yield are prepared for two types of the Al seal models. For other systematic error, decay time uncertainty based on [52], energy non-linearity discussed in 4.4 are considered. Figure 6.5 show the efficiency curve evaluated by changing systematic errors. By using all systematic errors, and upper side of the uncertainty $\Delta\text{Eff}_{\text{upper}}$ of relative efficiency is calculated as

$$\Delta\text{Eff}_{\text{upper}} = \sqrt{(\sigma_{\text{Alseal}}^{\text{stat}})^2 + (\sigma_{\text{default}}^{\text{stat}})^2 + \sum_{\text{Eff}_i > \text{Eff}_{\text{default}}}^{N_{\text{sys}}} (\text{Eff}_i - \text{Eff}_{\text{default}})^2}, \quad (6.4)$$

where N_{sys} and index i are representing the number of systematical errors and MC with changing the systematical errors, respectively. The summation is for the systematic errors whose efficiencies are larger than the one for the default MC simulations. Indices "default", and "Alseal" are representing the efficiencies evaluated with default geometry and modified geometry indicated in Fig. 3.12, respectively. $\sigma_{\text{default}}^{\text{stat}}$ and $\sigma_{\text{Alseal}}^{\text{stat}}$ are statistical error for each simulation. Since the simulation with changing the decay time and energy non-linearity are based on the statistically same sample, only $\sigma_{\text{default}}^{\text{stat}}$ and $\sigma_{\text{Alseal}}^{\text{stat}}$ are considered for statistical errors. Similarly, we can calculate a lower side of the uncertainty $\Delta\text{Eff}_{\text{lower}}$ as

$$\Delta\text{Eff}_{\text{lower}} = \sqrt{(\sigma_{\text{Alseal}}^{\text{stat}})^2 + (\sigma_{\text{default}}^{\text{stat}})^2 + \sum_{\text{Eff}_i < \text{Eff}_{\text{default}}}^{N_{\text{sys}}} (\text{Eff}_i - \text{Eff}_{\text{default}})^2}. \quad (6.5)$$

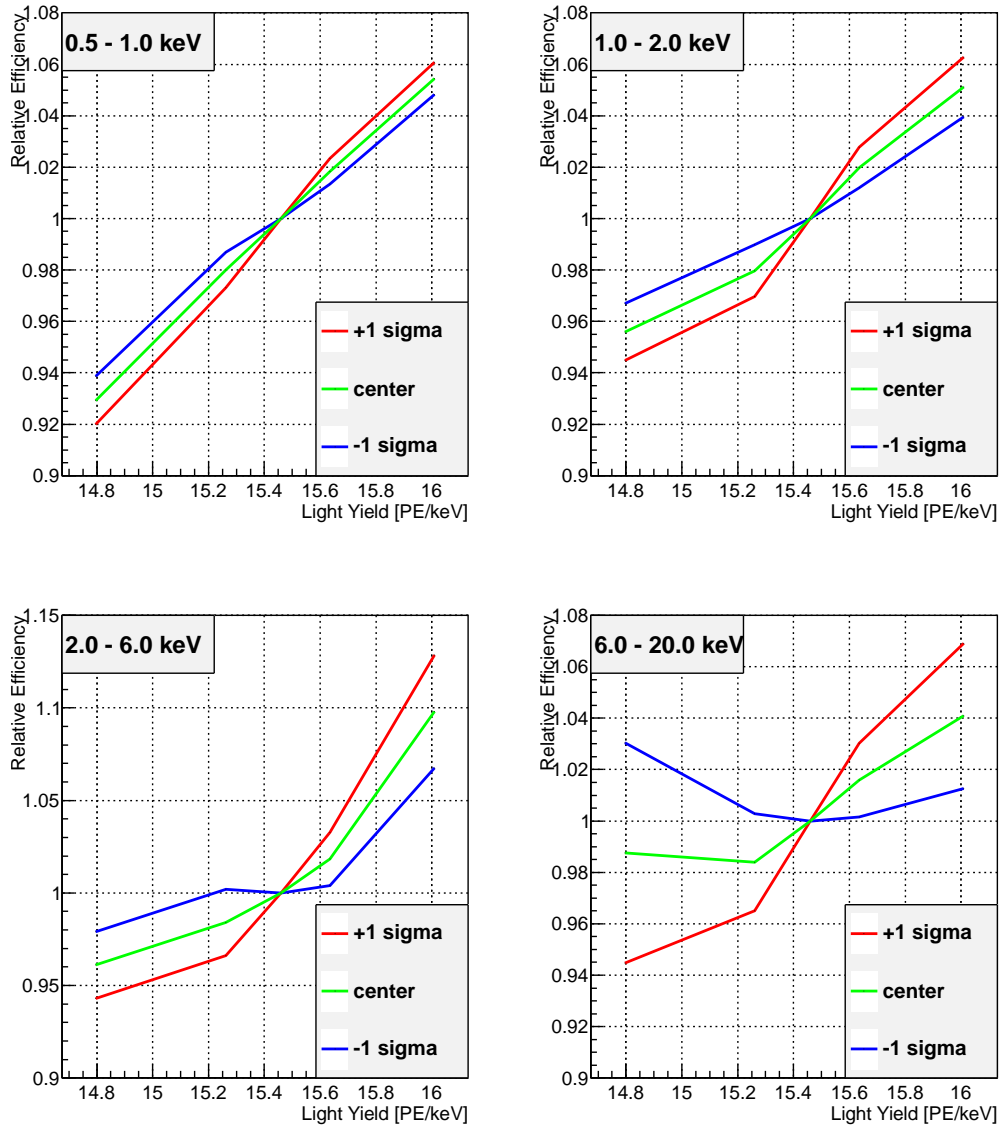


Figure 6.4: Relative efficiency curves with their uncertainties.

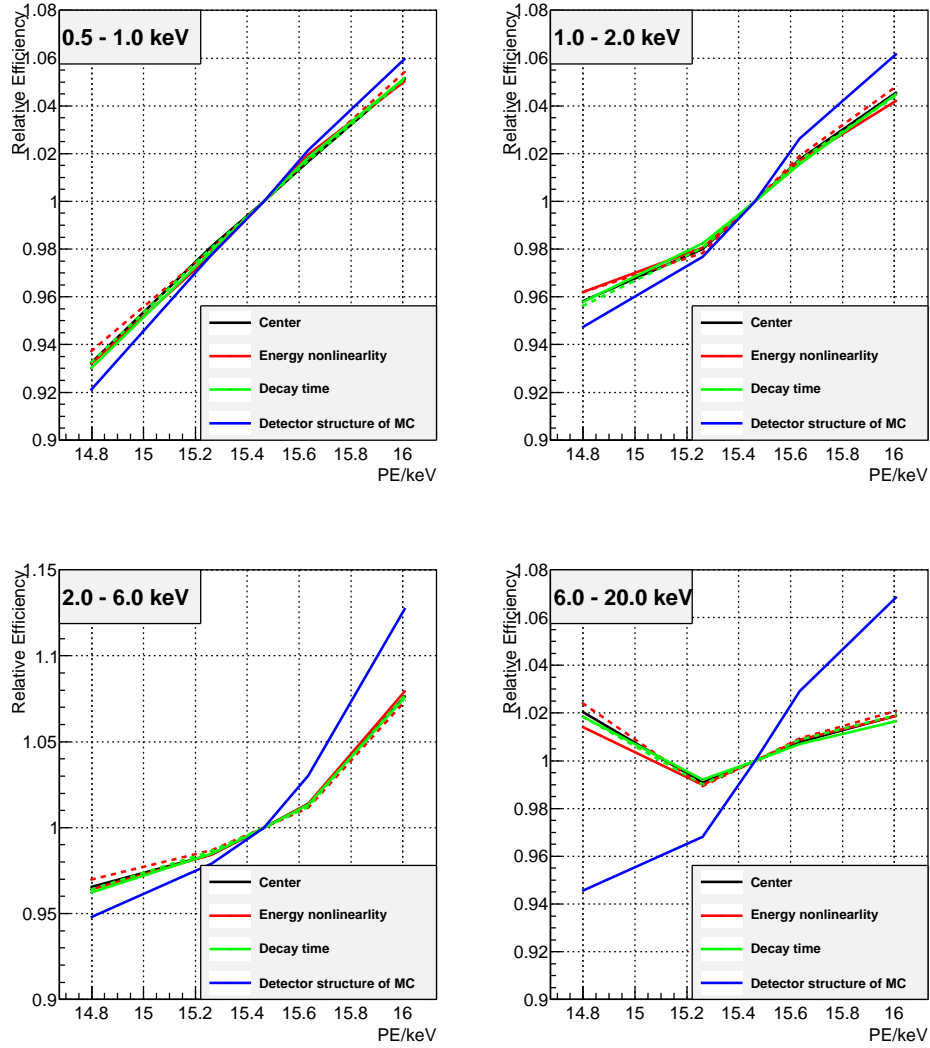


Figure 6.5: Relative efficiency. Each color shows the each component of systematic errors. Solid, dotted lines are +1 and -1 σ , respectively. Each color shows the each component of systematic uncertainty discussed in the text.

The upper side of the uncertainty $\text{Eff}_{\text{upper}}$, lower side $\text{Eff}_{\text{lower}}$, and the nominal efficiency $\text{Eff}_{\text{center}}$ are defined as

$$\begin{aligned}\text{Eff}_{\text{upper}} &= \text{Eff}_{\text{default}} + \Delta\text{Eff}_{\text{upper}}, \\ \text{Eff}_{\text{lower}} &= \text{Eff}_{\text{default}} - \Delta\text{Eff}_{\text{lower}}, \\ \text{Eff}_{\text{center}} &= \frac{\text{Eff}_{\text{upper}} + \text{Eff}_{\text{lower}}}{2}.\end{aligned}\tag{6.6}$$

In the fitting, uncertainty of the efficiency is considered with correlation between each period of data. Figure 6.6 shows the distribution of relative efficiencies for center (Black lines), $+1\sigma$ (Red lines), and -1σ (Blue lines) for each period and each energy region.

6.1.2 Stability of Electronics

Since the DAQ trigger is generated by a discriminator connected to the HITSUM signal, changes of the baseline of the signal HITSUM causes systematic changes of event rates. The baseline is monitored by recording raw waveforms by some channels of FADC and calculating the baseline level of HITSUM event, each crate, and each module. The distribution of the calculated baseline level is shown in Fig. 6.7. The analog baseline of each crate is inspected using an oscilloscope for every month and if necessary adjustment is done to keep the stability of the modules. In addition, they are inspected and adjusted if any changes of baseline is observed. At the output of the linear F/F in Fig. 6.8, mean of the HITSUM baseline for each run is shown. It has random fluctuation of 0.7 mV in RMS as shown in Fig. 6.9. Because of this, a change of HITSUM baseline within 1 mV is took into account as a systematic errors. The effect of a change of the HITSUM baseline is evaluated using the HITSUM distribution. Figure 6.10 shows the distribution of HITSUM height for the lowest energy bin, 0.5 - 1.0 keV, after the reduction. From this figure, (Entry at the 1 mV bin at 25mV)/(Entry of total data) found to be 0.3%. Based on this evaluation, an uncertainty of 0.3% is considered as systematic error at the lowest energy bin.

6.1.3 Event rate fluctuation caused by weak flashing of PMTs

Three hit events are affected by the changes of single rates of PMTs. Changes of rate of accidental coincidence itself are small, but weak flashing of PMT

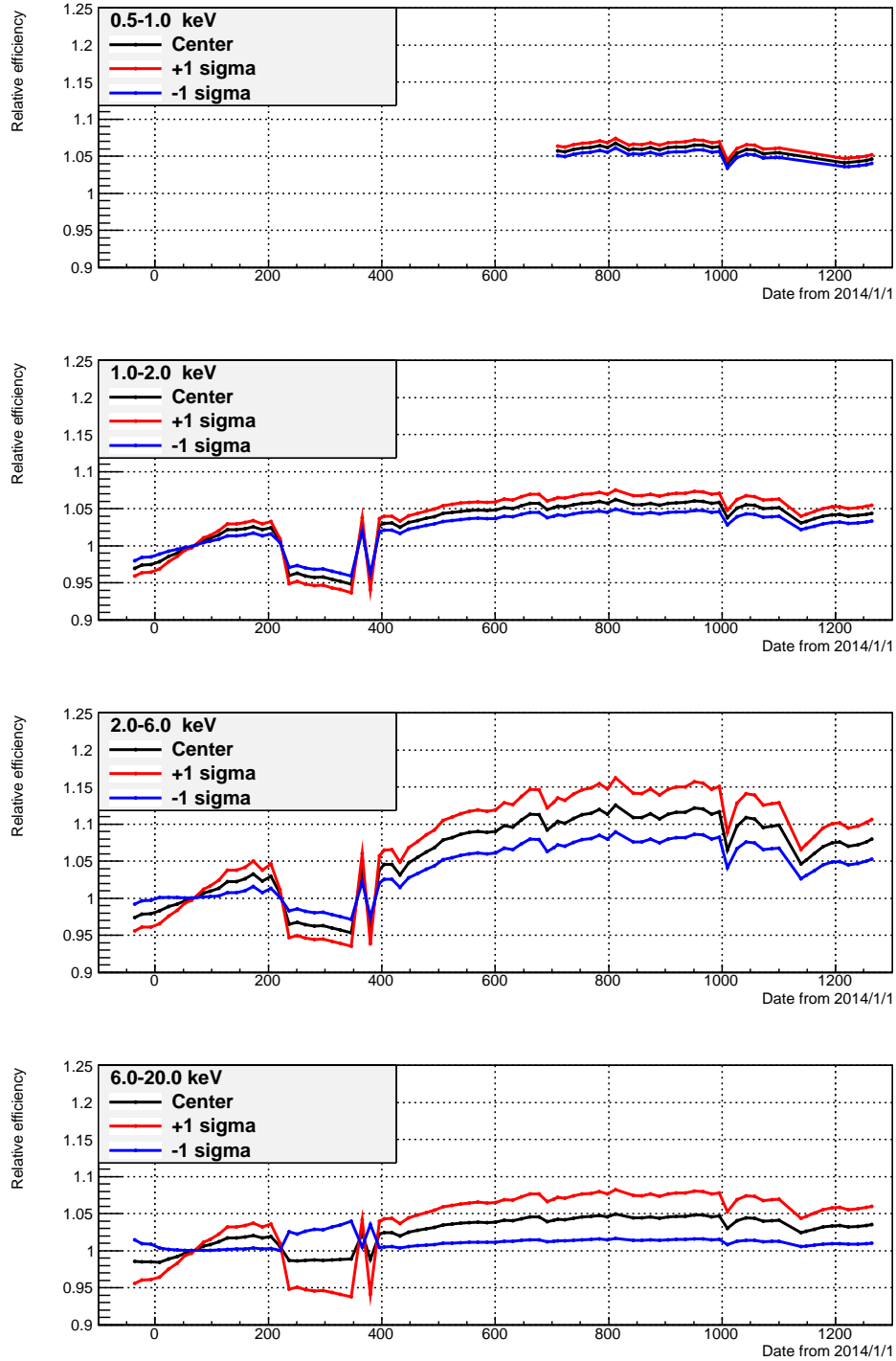


Figure 6.6: Change of relative efficiencies as the function of time with their uncertainties

Change of relative efficiencies as the function of time with their uncertainties.

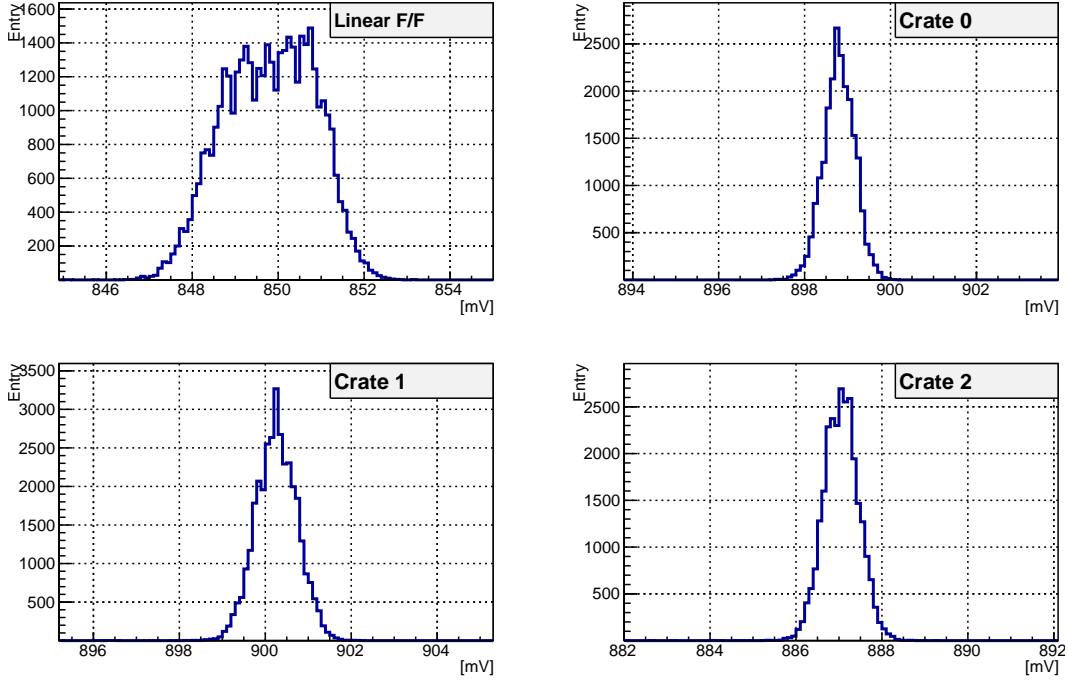


Figure 6.7: Distribution of HITSUM baseline during one run. Calculated for every event, by using recorded waveforms of FADC.

discussed in 4.3, accompanying to the single rate, causes change of event rates because it creates correlated hits. Weak flashing and single rate fluctuation can make fluctuation of event rates especially for three hit event.

Single rate of PMT

Since weak flashing occurs even after a single hit, sometimes three hit events are produced by a dark hit. These events are not produced by scintillation, and can have a correlation with the change of single rate of each PMT. Single rate for each PMT is monitored by using the clock trigger per 1 second. Each clock trigger make 1 μ s time window, and number of pulses for each PMTs during the run is used for calculating single rates. Typical single rate for one PMT is about 5 Hz, but sometimes it increase up to a few hundreds Hz. Expected rate of accidental three hit events can be roughly calculated by using the single rate of each PMT. Using the width of HITSUM w and

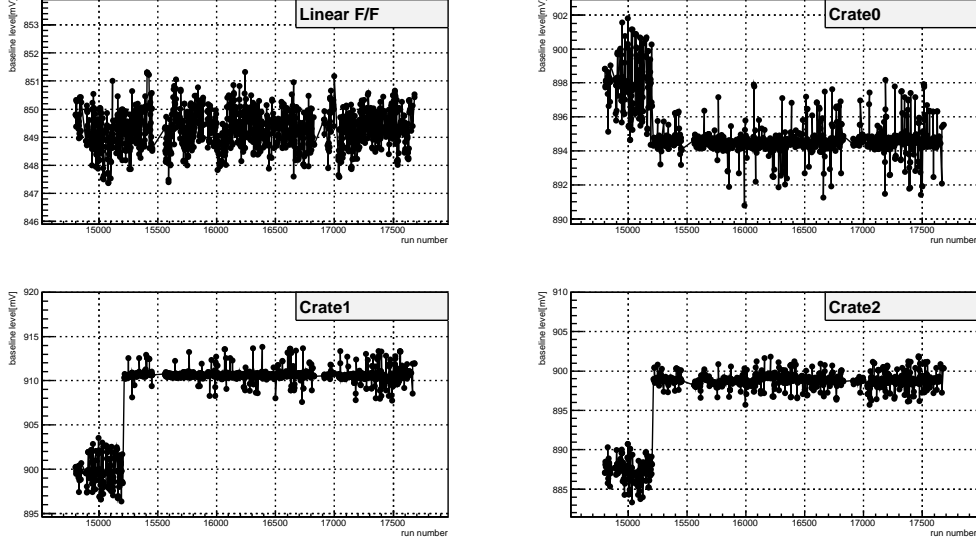


Figure 6.8: Mean of HITSUM baseline distribution for each run. A sudden jump for crate 0, 1, 2 is caused by a channel swapping of FADC channels to record these waveforms.

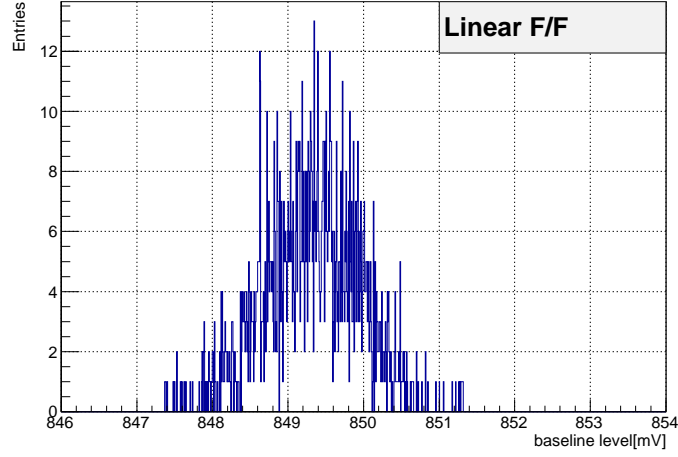


Figure 6.9: Distribution of HITSUM mean for linear F/F. One entry is one run.

single rate of i -th PMT, S_i ,

$$R_{acc} = \frac{1}{2} \sum_{i=0}^{NPMT} \sum_{j \neq i}^{NPMT} \sum_{k \neq i,j}^{NPMT} S_i \cdot S_j \cdot S_k \cdot w^2 \cdot \frac{1}{2} \quad (6.7)$$

$$\approx 0.0007[Hz] \text{ (In the case of 5Hz for all PMTs)} \quad (6.8)$$

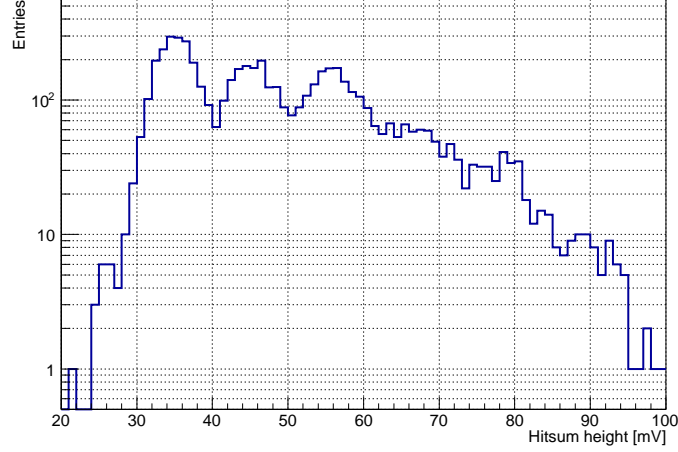


Figure 6.10: distribution of HITSUM height.

assuming of 5 Hz of single rate for all PMTs. In addition to this accidental coincidence events, there are events caused by the correlated hits. Especially, weak flashing of the PMT creates three hit events. For example, 1000 Hz of single rate change can produce $1000 \times 0.003 \times 0.003 = 0.009$ [Hz] of the three hit events 0.3% of single hit causes another hit.

Calculation of the event rate stability after the flasher cut

As discussed in the previous section, the fluctuation of single rate affects the three hit event rate through the flashing of PMT. Most of PMTs used for XMASS have stable and low single rate, but some of them have significant fluctuations. Six periods in Table 6.1 are chosen to examine the impact of the change of three hit event rate. During these periods, some PMTs have significantly larger single rate than usual. Difference of total single rate, summed up single rate for all PMTs, and three hit event rate is evaluated by subtracting the rate in a previous period with lower total rate just before the high rate period. Figure 6.11 shows the relation between the difference of total single rate and three hit event rate without the flasher cut. In this figure, a linear relation between three hit event rate and total single rate can be clearly seen.

Figure 6.12 shows the same relationship after the flasher cut. Even statistical error is large, a weak linear relation can be seen. Figure 6.13 show

Period	livetime [days]	Total single rate of the period [Hz]	Total single rate of previous period [Hz]	Difference of single rate [Hz]
1	1.47	3519.4	2673.9	845.4
2	5.38	4330.9	2700.2	1630.7
3	26.8	3127.1	2982.2	144.9
4	5.96	2547.5	2355.8	191.7
5	12.6	3535.6	2637.1	898.5
6	12.7	3093.3	2684.1	409.2

Table 6.1: Summary of the terms for the calculation of flasher effect.

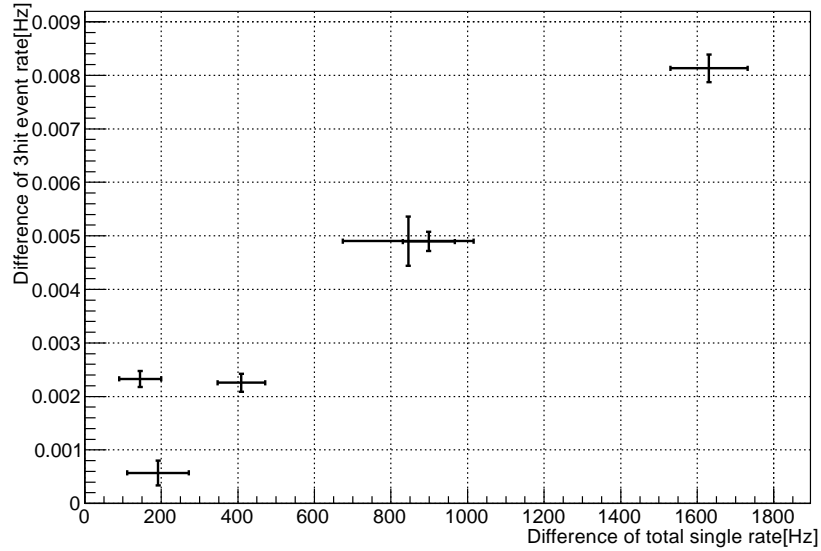


Figure 6.11: Relationship between the difference of single rate and difference of three hit event rate before the flasher cut.

the range of systematic errors calculated based on Fig. 6.12.

6.1.4 Internal gain instability of FADC

The gain uncertainty of FADC has an impact when we estimate the light yield. At the start of each run, FADC is initialized. During the period from April 2015 to September 2015, the internal calibration was additionally performed when the initialization is executed to suppress a sudden changes of baseline observed before. However, it was found that this gain calibration

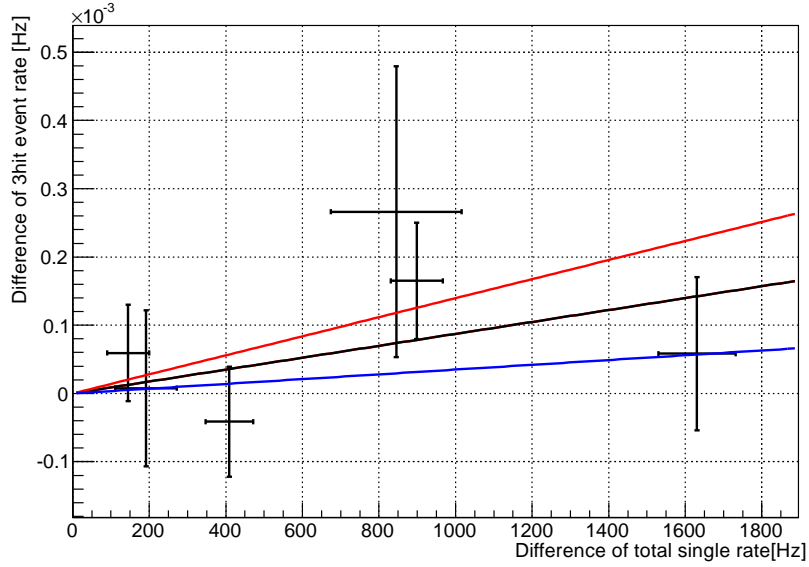


Figure 6.12: Relationship between the difference of single rate and difference of three hit event rate after flasher cut. Black line shows the result of linear fitting. Red and blue lines are showing the $+1$ and -1 σ range of the slope.

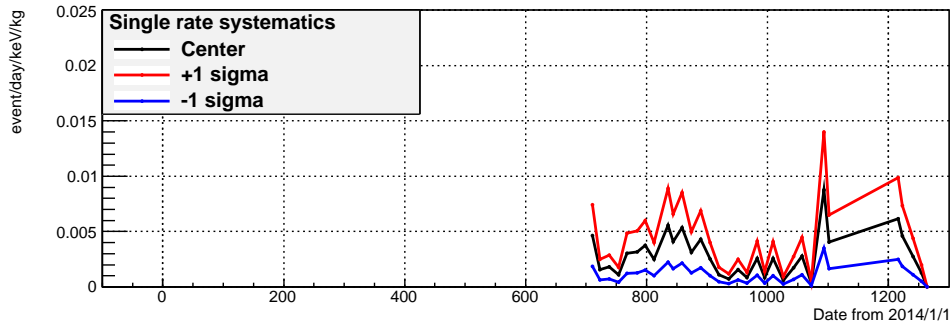


Figure 6.13: Impact on the three hit event rate and its systematic errors.

make small changes of internal gain for all channels about 0.3%. Because of this, the estimation of light yield for this term have a large uncertainty. This introduces 0.3% uncertainty on the event rate at 1 keV, we added this uncertainty to the error for real data by quadrature.

6.2 Systematic errors in evaluation of expected signal

6.2.1 Nuclear recoil energy spectrum of WIMPs

Two systematic errors are considered for the WIMP expected spectrum. The first error is for the decay time of the nuclear recoil (NR) in the simulation. In the simulation for the XMASS-I detector, scintillation emission of each particle has two components of decay time, such as a faster and a slower component. For NR events, standard values are 4.3 ns and 27.5 ns, respectively. The error for scintillation decay time is estimated for the slower component as ± 2 ns, based on the neutron calibration for the XMASS-I detector [51]. The second systematics for the WIMP spectrum is a quenching factor of LXe L_{eff} for the nuclear recoil process. The size of the systematic error shown in the reference is adopted for each corresponding energy bin. Figure 6.14 shows the spectrum of 10GeV WIMPs with systematic errors.

6.2.2 Bremsstrahlung photons energy spectrum

For the energy spectrum of bremsstrahlung, energy calibration error and scintillation decay time error are considered similar to the nuclear recoil spectrum in the previous subsection. The major systematic error is the uncertainty of energy scale for X-ray events discussed in Sec. 4.4. As similar to the quench factor of the nuclear recoil events, an effect of this energy scale is also included as systematic error. Figure 6.15 shows the spectrum of bremsstrahlung photon with systematic errors. For decay time, error was estimated from the measurement by the XMASS-I [52]: uncertainty of +1.5 ns and -1.0 ns.

6.3 Other Systematic errors

6.3.1 Muon induced events

Possible Spallation products in the inner detector

The event rate of muon passing through ID and OD is 0.0014 Hz in the XMASS-I data set. This corresponds to the 0.14 event/day/kg. Assuming spallation products may cause extra background extending around MeV energy range, this roughly corresponds to 1×10^{-4} event/day/keV/kg. This is

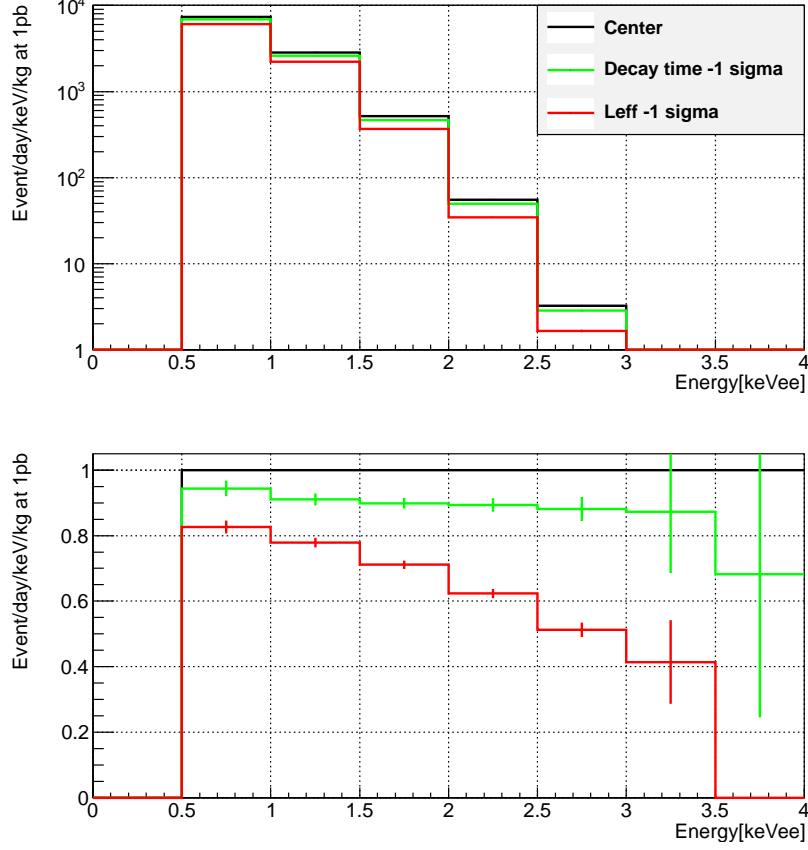


Figure 6.14: Expected spectrum of 10 GeV WIMPs and fraction from center value. Each color shows the each condition of systematic errors.

much smaller than the event rate the data, 1 event/day/keV/kg. This assumes an extreme case, since spallation products may not cause background always. Furthermore, the radiation from the spallation of detector materials within 10 ms are removed by the dt cut in the step of event reduction. Because of these consideration, we recognize the spallation products do not cause any systematic effect in searching for annual modulation.

Neutron flux from outside of the detector

Based on the measurement of neutron flux in the underground laboratory [53], the neutron flux from the rock is estimated to be $10^{-8}\text{n/cm}^2/\text{sec}$, $10^{-9}\text{n/cm}^2/\text{sec}$ for $E > 10\text{ MeV}$ and $E < 10\text{ MeV}$, respectively. Assuming $10^{-8}\text{n/cm}^2/\text{sec}$ as

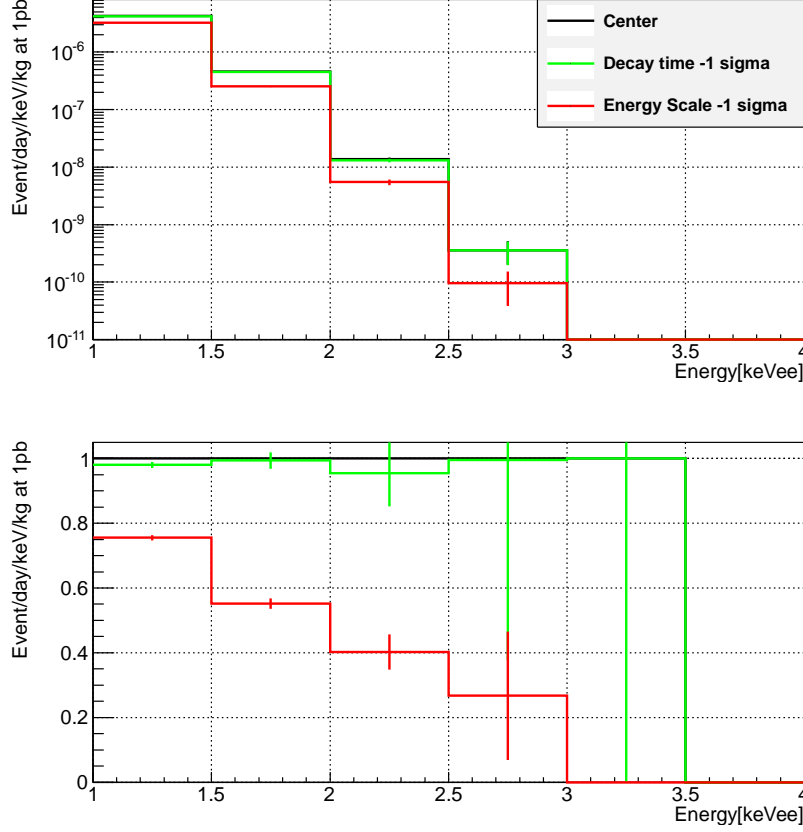


Figure 6.15: Expected spectrum of bremsstrahlung photons from 0.5 GeV WIMPs and fraction from center value. Each color shows the each condition of systematic errors.

the flux, the expected number of neutron in water tank with $4.5 \times 10^6 \text{ cm}^2$ of the surface area, is $10^{-8} \times (4.5 \times 10^6) \times 86400 = 3.9 \times 10^3 \text{ n/cm}^2/\text{day}/\text{watertank}$. From the MC study it was found that the reduction power of 2 m water tank is about 10^{-7} , so the expected number of neutron to the inner detector is $3.9 \times 10^3 \times 10^{-7}/832 = 4.7 \times 10^{-7} \text{ n/cm}^2/\text{day}/\text{detector}$. We concluded this contribution is also negligible.

6.3.2 Rn in the water tank

Radon in the water tank is continuously measured by using the water radon detector. The previous study by MC simulations [54] shows that 1 Bq/m^3

of water radon make the background event rate of 10^{-4} event/day/keV/kg for inner detector. Maximum ^{222}Rn concentration of water radon was $(1.4 \pm 0.2) \times 10^2$ mBq/m³ and this corresponds to $(1.4 \pm 0.2) \times 10^{-5}$ event/day/keV/kg in the XMASS-I detector. This is also negligible contribution to the data.

Chapter 7

Analysis method for annual modulation

7.1 Minimum χ^2 fitting

7.1.1 Definition of χ^2

Extracting annual modulation signal is based on the minimum χ^2 fitting. Actual χ^2 function is defined as follows:

$$\chi^2 = \sum_i^{E_{bin}} \sum_j^{T_{bin}} \frac{(R_{data}^{i,j} - R_{exp}^{i,j}(\alpha, \beta) - R_{SR}^{i,j}(\gamma))^2}{(\sigma_{exp}^{i,j})^2 + (\sigma_{sys}^{i,j})^2} + \alpha^2 + \sum \beta^2 + \gamma^2, \quad (7.1)$$

where $R_{data}^{i,j}$ is the event rate for each energy bin i and time bin j , $R_{exp}^{i,j}$ is expected number of events explained by the following section. $R_{SR}^{i,j}(\gamma)$ is the effect of single rate discussed in Sec. 6.1.3, and only introduced into the lowest energy bin. $\sigma_{exp}^{i,j}$ is statistical error calculated by expected number of events, and $\sigma_{sys}^{i,j}$ is systematic errors for each energy and time bin. In this χ^2 function, some systematic errors are treated as fitting parameters with constraints. They can be optimized to minimize the χ^2 , but fitting of these parameters are constrained within their uncertainties.

The terms containing α , β and γ , the pull terms in the Eq. 7.1, represent the constrains for them. If these parameters changes too much more than their systematical error, the pull terms make χ^2 worse. By using this pull term method, four systematical errors are treated in a proper way;. (1) uncertainty of the efficiency curve of background estimation, (2) uncertainty of the effect

of the single rate fluctuation, (3) uncertainty of the scintillation efficiency of the signal, and (4) uncertainty of the scintillation decay time of the signal.

7.2 Expected event rate

In the following sections, three types of approaches to extract dark matter signal will be discussed. The first one is bremsstrahlung from the nuclei due to the recoil of WIMPs. The second one is nuclear recoil of WIMPs. Hereafter, they will be referred to as the bremsstrahlung analysis and nuclear recoil analysis, respectively. For these models of dark matter interaction, expected mean and residual amplitude of the dark matter can be calculated in Chapter 2. Importantly, modulation of each energy bin is correlated each other in this models. The third one is an analysis without any constraint to the expected energy spectrum. This implies modulation of each energy bin needs to be independently extracted. Hereafter, this analysis will be referred as model-independent analysis.

7.2.1 Bremsstrahlung and Nuclear recoil of standard WIMPs

An expected event rate is expressed as follows;

$$R_{exp}^{i,j}(\alpha, \beta) = \int_{t_j - \Delta t_j}^{t_j + \Delta t_j} \left[E_{bg}(\alpha) \cdot (C_{bg}^i + S_{bg}^i \cdot t) + \sigma \cdot E_{sig}^i \left\{ C_{sig}^i(\beta) + A_{sig}^i(\beta) \cos 2\pi \frac{t_j - t_0}{T} \right\} \right] dt, \quad (7.2)$$

where i indicates each energy bin, and j indicate each time bin. α, β terms are show parameters for the penalty term in χ^2 .

In the analysis of [29], background event rate was assumed to be constant. However in this thesis decrease of the background radioactivity due to natural decay was introduced. The decay of ^{210}Pb , which is the daughter of U chain with 22 years of half life, is one of the major component of background [30]. For the case of bremsstrahlung from WIMP recoil, treatment is same to that for nuclear recoil of WIMPs. The mean and amplitude of spectrum, C, A need to be calculated for the bremsstrahlung from nuclear recoils for a particular cross section and mass of WIMPs. Systematical errors represented by the pull term need to be calculated based on the bremsstrahlung spectrum. Functions of each pull terms are shown as follows.

$$E_{bg}^{i,j}(\alpha) = E_{bg,0}^{i,j} + \alpha \times \Delta E_{bg}^{i,j} \quad (7.3)$$

$$C_{sig}^{i,j}(\beta) = C_{sig}^{i,j}(0) \times \prod_k^{N_{sys}} \text{Eff}_C(\beta_k) \quad (7.4)$$

$$\text{Eff}_C(\beta_k) = C_{sig}(\beta_k)/C_{sig}(0) \quad (7.5)$$

$$A_{sig}^{i,j}(\beta) = A_{sig}^{i,j}(0) \times \prod_k^{N_{sys}} \text{Eff}_A(\beta_k) \quad (7.6)$$

$$\text{Eff}_A(\beta_k) = A_{sig}(\beta_k)/A_{sig}(0) \quad (7.7)$$

$$R_{SR}^{i,j}(\gamma) = R_{SR}^{i,j}(0) + \gamma \times \Delta R_{SR}^{i,j} \quad (7.8)$$

where E_{bg} , ΔE_{bg} are the center, width of relative efficiency curve shown in Fig. 6.6, respectively. $C_{sig}(\beta_k)$, $A_{sig}(\beta_k)$ are the signal spectrum with systematic error k, scintillation efficiency or decay time, and Fig. 6.15 show the case of 0.5 GeV WIMPs. R_{SR} , ΔR_{SR} are the center, width of relative efficiency curve shown in Fig. 6.13, respectively.

7.2.2 Model independent analysis

For the model-independent analysis, there are no constraint on the signal shape. Because of that, only amplitude of signal component is included in the function. Equation 7.9 shows the function to extract modulation signal in the case of the model independent analysis.

$$R_{exp}^{i,j} = \int_{t_j - \Delta t_j}^{t_j + \Delta t_j} \left[E_{bg}^{i,j}(\alpha) \cdot (C_{bg}^i + S_{bg}^i \cdot t) + E_{sig}^i \left\{ A_{sig} \cos 2\pi \frac{t_j - t_0}{T} \right\} \right] dt \quad (7.9)$$

7.3 Sensitivity estimation

7.3.1 Generation of the dummy sample

The expected sensitivity is evaluated using the toy Monte Carlo samples, called dummy sample without any modulation signal embedded. The first step to generate dummy samples is determination of coefficients, E_{bg} , C_{bg}^i , S_{bg}^i in Eq. 7.2. Instead relying on our simulation, these coefficients are obtained by fitting real data with Eq. 7.2 by setting $\sigma = 0$. The blue line in the

Fig. 7.1 shows the linear fit result of data. The second step is a correction of the event rates using the efficiency curve based on the light yield of each period. In this step, systematic uncertainty of efficiency curve is introduced by fluctuating the efficiency curve by a gaussian distribution for generation of one set of dummy sample. Thousand of dummy samples are calculated with this method, and each sample has different efficiency curve from gaussian distributions and systematical error discussed in Sec. 6.1.1. The red lines in the Fig. 7.1 show an expected event rate for each period by considering the efficiency curve for this dummy sample. The third step is to give statistical fluctuation for each energy and each period based on corresponding livetime. Black points of Fig. 7.1 show one of the dummy samples. Since these dummy samples do not have modulation amplitude by dark matter, by using these samples, sensitivity with null amplitude case can be evaluated.

7.3.2 Calculation of sensitivity for the case of bremsstrahlung and nuclear recoil of WIMPs

For bremsstrahlung and nuclear recoil signal from WIMPs, expected spectrum for each mass and each cross section can be calculated as in Sec. 7.2.1. By the equation (7.2), only cross section is the fitting parameter for each mass of WIMPs. Since other parameters are used to minimize χ^2 set as free and fitted. Although dummy samples have null amplitude, each sample has its best fit point of cross section for WIMPs with their error. Figure 7.2 shows the distribution of best fit cross sections assuming mass of WIMPs indicated in each figure.

By using the shape of χ^2 as a function of the cross section, 90% C.L. upper limit was for each sample is calculated and total distribution of expected 90% C.L. upper limit is calculated as the function of WIMPs mass. 90% C.L. upper limit a_{lim} for each sample is calculated to satisfy the equation 7.10 below.

$$\frac{\int_0^{a_{lim}} e^{-\frac{\chi^2}{2}}}{\int_0^{\inf} e^{-\frac{\chi^2}{2}}} = 0.9 \quad (7.10)$$

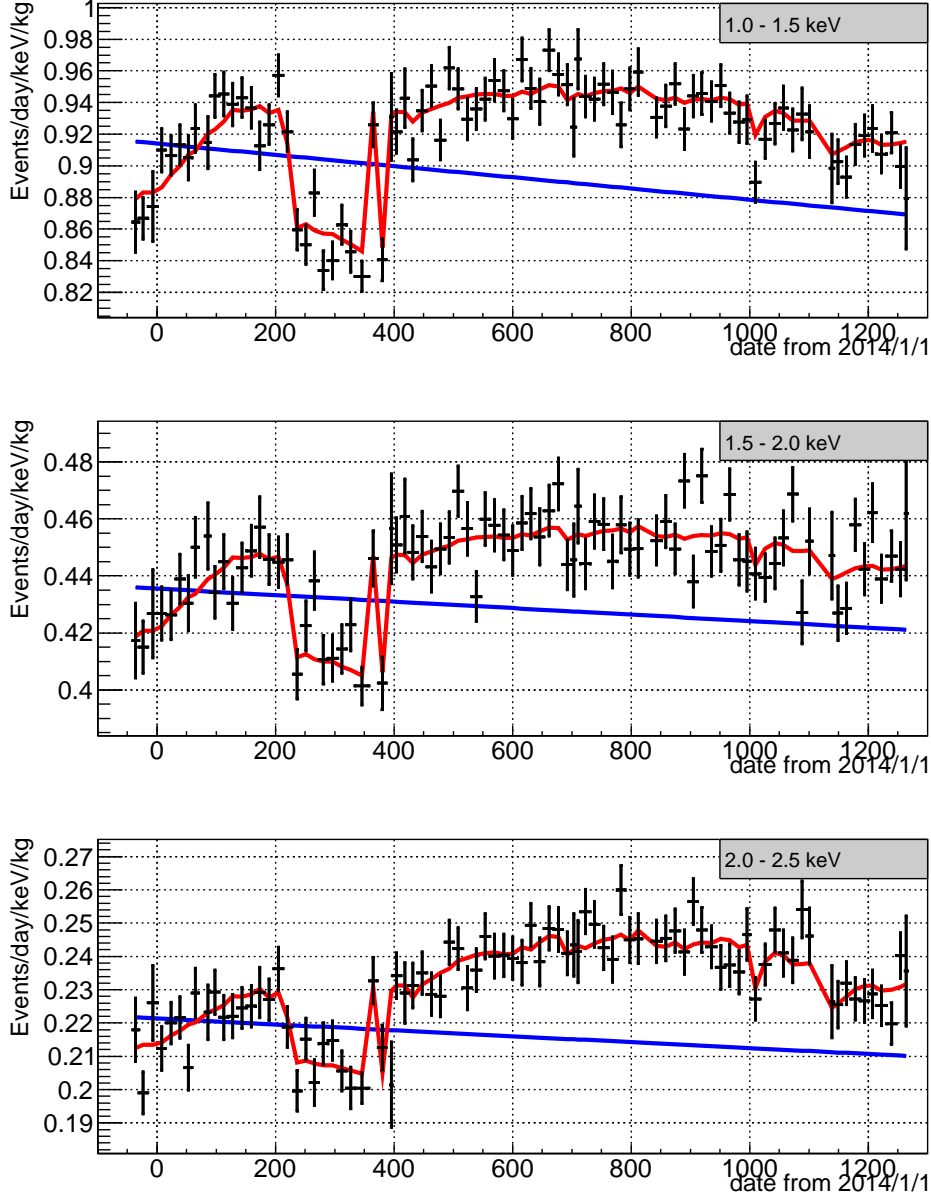


Figure 7.1: Example of Dummy sample at 1.0-2.5 keV. Blue and red line shows the expected event rate with and without the efficiency curve correction for each period. Black points are calculated by Poisson fluctuations based on the livetime and expected event rate of each period.

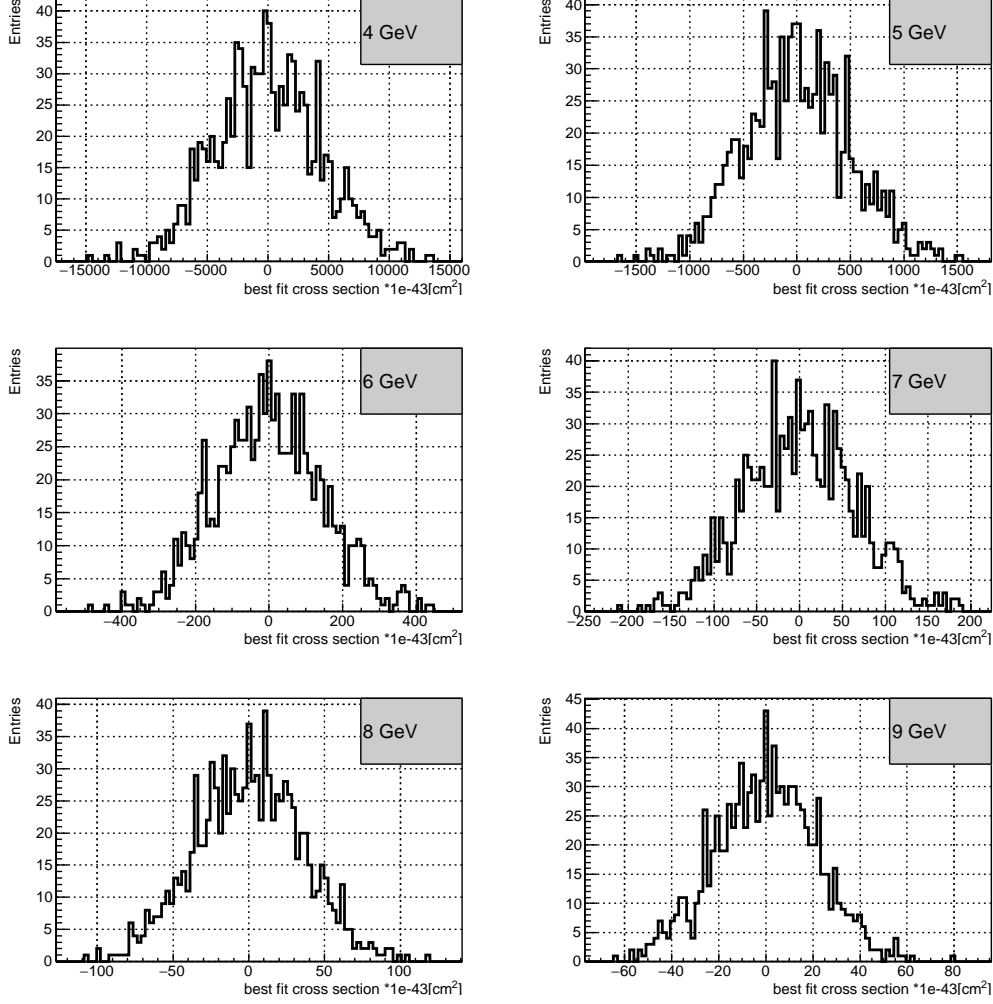


Figure 7.2: Distribution of the best fit position of cross section for each mass of WIMPs.

7.3.3 Demonstration of analysis using sample with significant amplitude

To demonstrate the validity of this analysis, a dummy sample with finite amplitude was used to analyze. For this analysis, an amplitude based on 6 GeV WIMP with a cross section of $9.2 \times 10^{-41} \text{ cm}^2$ ($+2 \sigma$ edge of 90% confidence level upper limits from null amplitude samples) was added for a dummy sample. The 90% confidence intervals (CI) are calculated for 1000 samples, and 901 samples of them gave results covering true cross section

$9.2 \times 10^{-41} \text{ cm}^2$ within 90% CI. This shows that the method of analysis gave a correct coverage and working as expected.

Chapter 8

Result of modulation analysis

8.1 Result of the sub-GeV WIMP search

Result of the sub-GeV WIMPs search based on the bremsstrahlung effect is shown in the Fig. 8.1 to Fig. 8.4. Black points are data including statistical and systematic errors. Red brackets are showing systematic error only. Green curves are showing the best fit result for 0.5 GeV WIMPs. Since live-time of the period 28 at day 395 is shorter than others, that period have larger statistical fluctuation than others. This short livetime is because of the special operation of detector related to the maintenance of cryocooler. From the fitting result, no significant signal was found in the data. Because of that, a 90% confidence level limit is drawn. Figure 8.5 shows the result. The horizontal axis is the mass of WIMPs in GeV, and the vertical axis is the elastic cross section between WIMP and nucleon, $\sigma_{\chi-n}$, in cm^2 . The search is performed from 0.32 GeV to 1.0 GeV. The lower limit of mass is chosen not to rely on only a tail of an energy resolution. Blue line is the upper limit obtained from data. Green and yellow bands are expected sensitivity calculated using null amplitude dummy sample. More than 0.32 GeV, bremsstrahlung γ ray give more than 1 keVee signal even at the winter. The higher limit is chosen based on the validity of assumption for the spectrum calculation. Since the reference [33] assumes the form factor of xenon nucleus always unity, the author indicated their calculation is valid for the WIMP mass less than 1 GeV.

p-value for null amplitude hypothesis assuming certain mass definition is

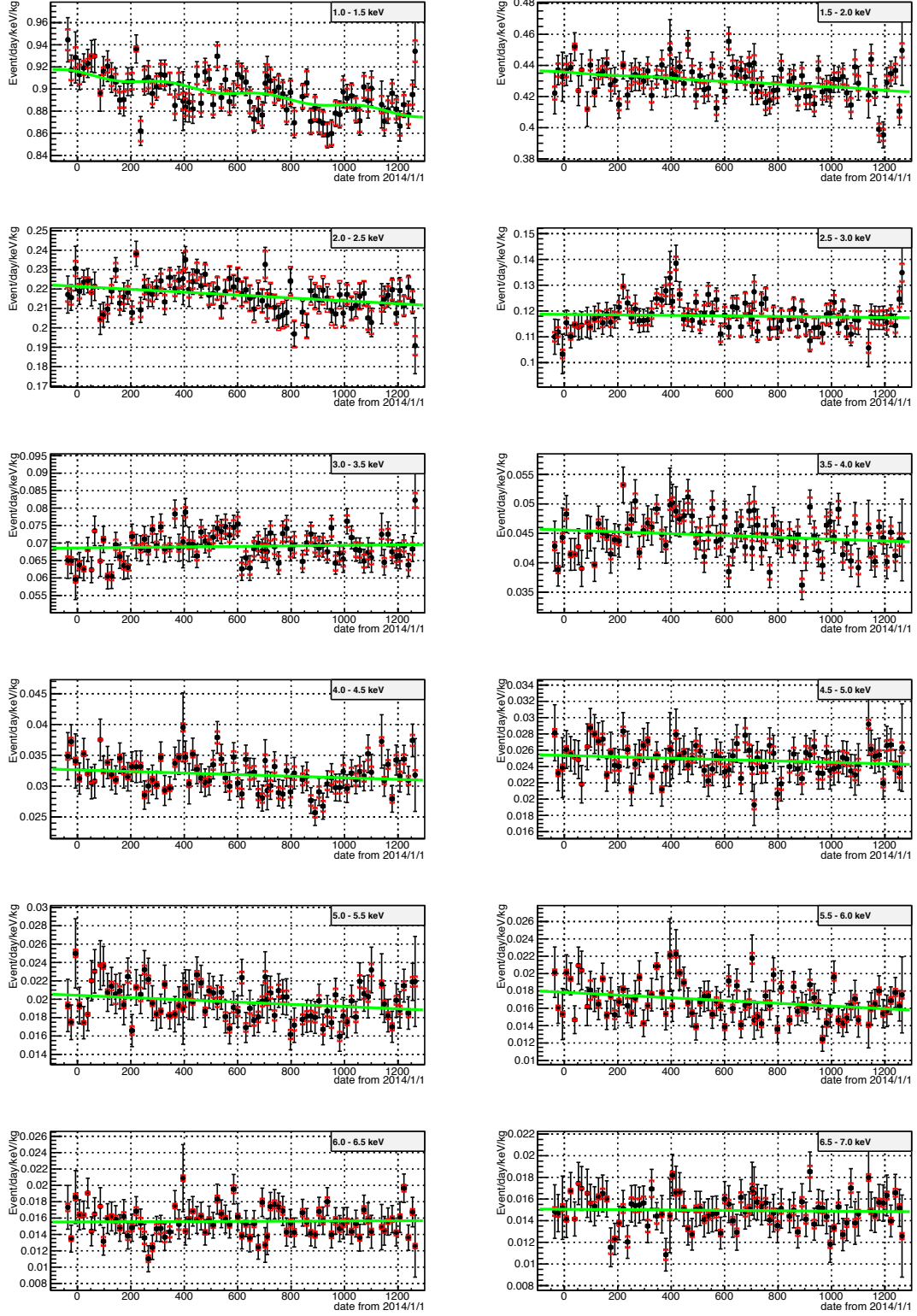


Figure 8.1: The result of fit with bremsstrahlung signal of 0.5 GeV WIMPs. Black points are data including statistical and systematic errors. Red brackets are showing systematic error only. Green curves are showing the best fit result for 0.5 GeV WIMPs.

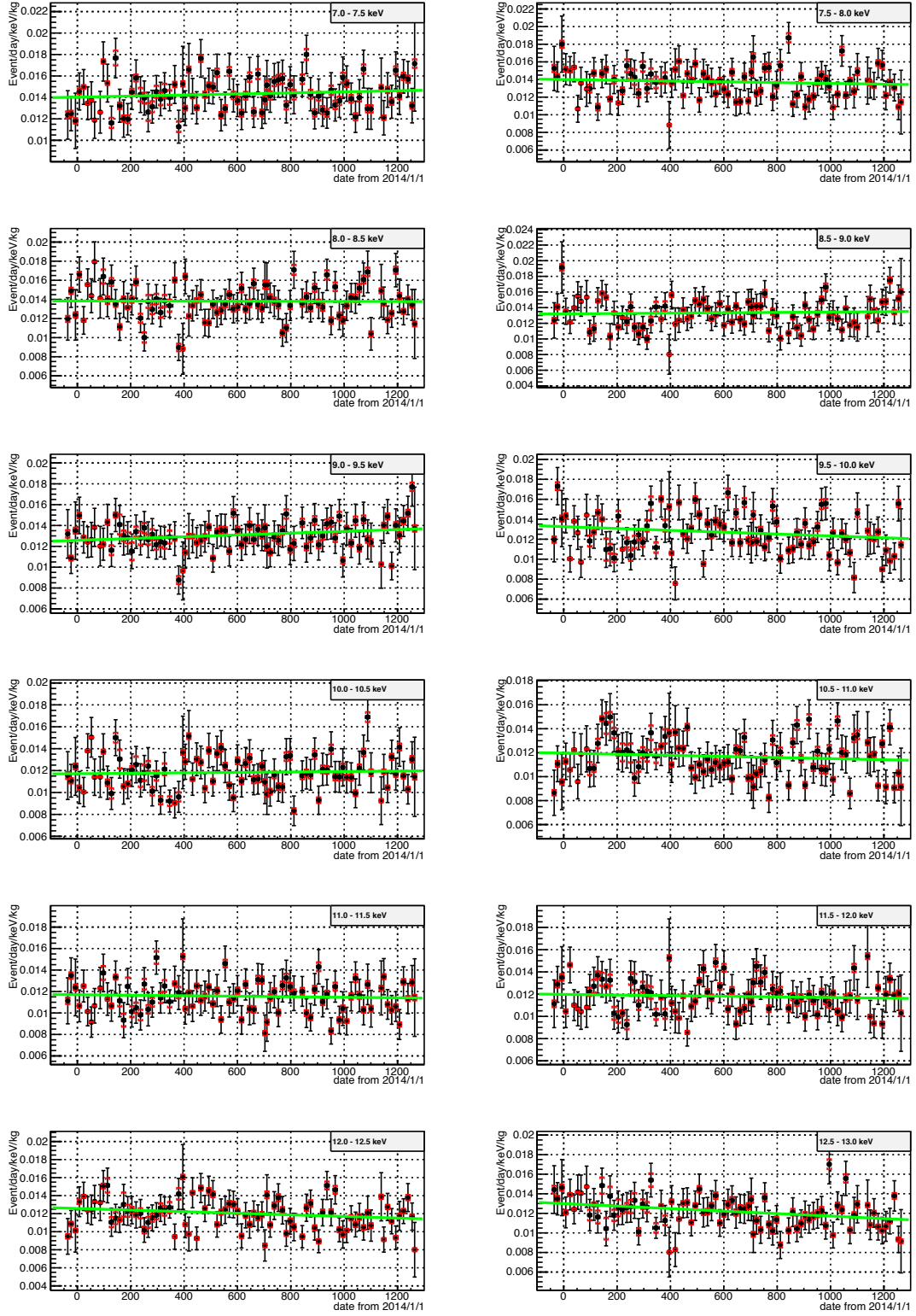


Figure 8.2: The result of fit with bremsstrahlung signal of 0.5 GeV WIMPs. Black points are data including statistical and systematic errors. Red brackets are showing systematic error only. Green curves are showing the best fit result for 0.5 GeV WIMPs.

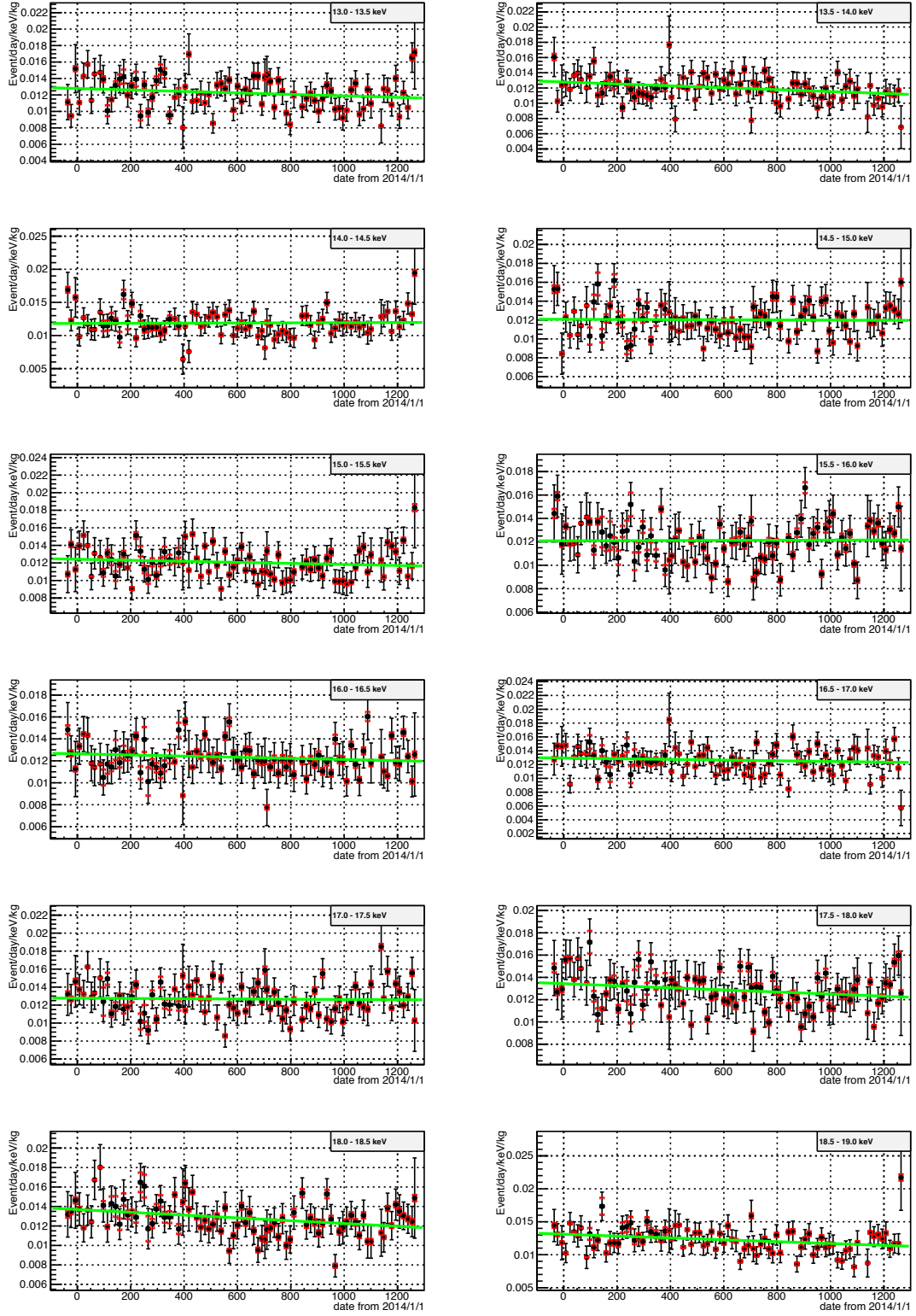


Figure 8.3: The result of fit with bremsstrahlung signal of 0.5 GeV WIMPs. Black points are data including statistical and systematic errors. Red brackets are showing systematic error only. Green curves are showing the best fit result for 0.5 GeV WIMPs.

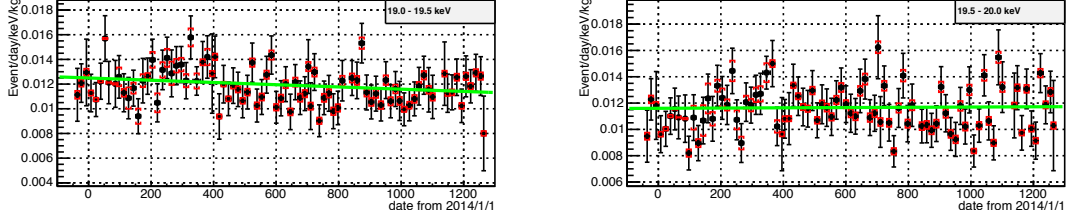


Figure 8.4: The result of fit with bremsstrahlung signal of 0.5 GeV WIMPs. Black points are data including statistical and systematic errors. Red brackets are showing systematic error only. Green curves are showing the best fit result for 0.5 GeV WIMPs.

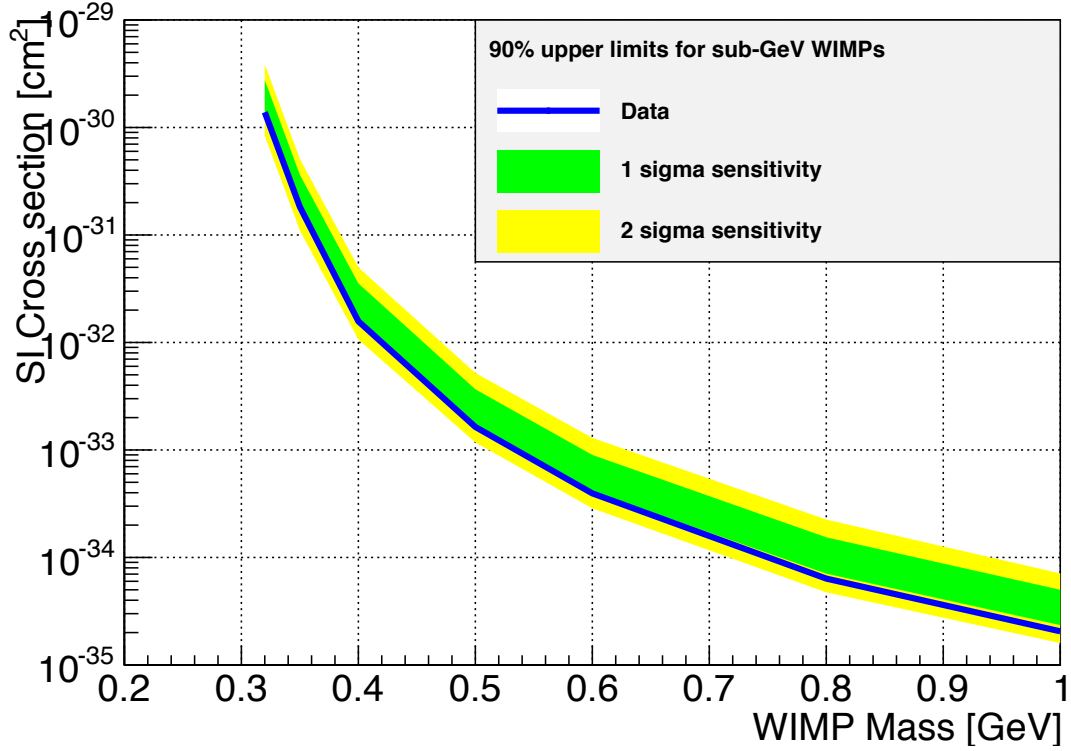


Figure 8.5: 90 % C.L. upper limits of data and the sensitivity band for null amplitude utilizing the bremsstrahlung effect.

calculated using a $\Delta\chi^2$ defined as

$$\Delta\chi^2 = \chi_{\sigma=0}^2 - \chi_{\sigma=\text{BestFit}}^2, \quad (8.1)$$

where $\chi_{\sigma=\text{BestFit}}^2$ and $\chi_{\sigma=0}^2$ are χ^2 at the best fit cross section and zero, respectively. The $\chi_{\sigma=\text{BestFit}}^2$ is calculated including the negative value of cross

section. By using the distribution of $\Delta\chi^2$ prepared by dummy samples, p-value is defined as

$$p = \frac{\text{Number of samples with } \Delta\chi^2 > \text{data}}{\text{Total number of samples}}. \quad (8.2)$$

Figure 8.6 shows the distribution of $\Delta\chi^2$ the for 0.5 GeV WIMPs. Each entry is each sample, and the red line represents the $\Delta\chi^2$ of the data. Table 8.1

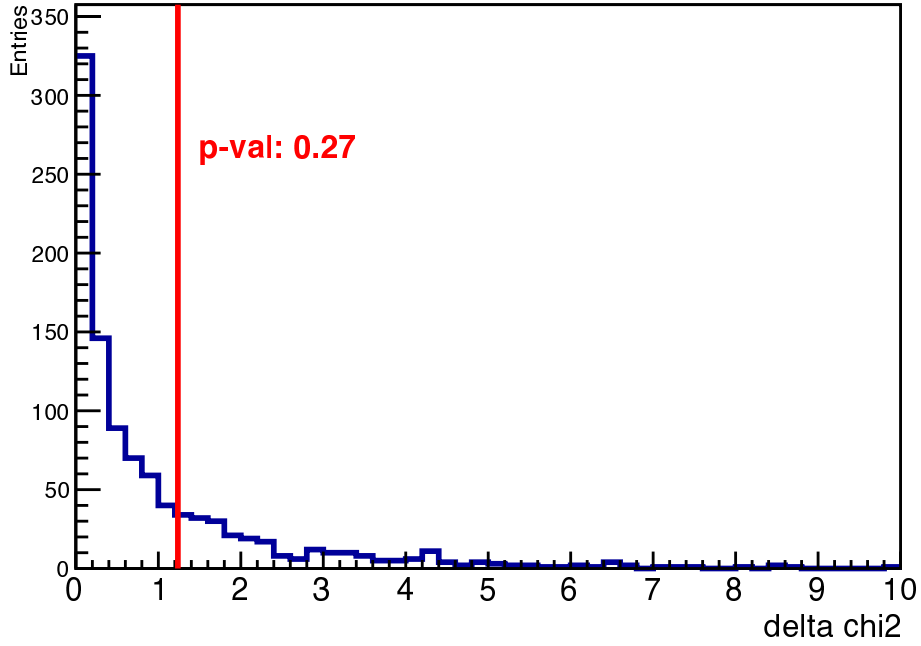


Figure 8.6: The distribution of $\Delta\chi^2$ for 0.5 GeV WIMPs. Each entry is one dummy sample, and red line represents the $\Delta\chi^2$ of the data.

shows the numerical results. p-value for null amplitude case is larger than 0.05 for all searched mass. All pull terms for relative efficiency, efficiency and signal estimation at best fit are locating within 1σ . The p-value for absolute χ^2 is also calculated using dummy samples. For null modulation hypothesis, it is 0.034.

8.2 Result of the light WIMP search

Same as in the previous section, no significant signal of WIMPs were found and 90% C.L. upper limit is calculated. Result of the WIMPs search based

WIMP mass[GeV]	best fit $\sigma[\text{cm}^2]$	p-value	90%C.L. $\sigma[\text{cm}^2]$	χ^2	α	β_1	β_2
0.32	-5.5e-31	0.47	1.4e-30	3334.48	0.61	0.05	-0.002
0.35	-7.5e-32	0.46	1.9e-31	3334.47	0.61	0.05	-0.002
0.40	-1.1e-32	0.29	1.6e-32	3333.90	0.60	0.08	-0.002
0.50	-1.4e-33	0.27	1.6e-33	3333.76	0.60	0.09	-0.002
0.60	-3.8e-34	0.23	3.9e-34	3333.60	0.60	0.09	-0.001
0.80	-7.7e-35	0.19	6.4e-35	3333.31	0.60	0.06	-0.001
1.00	-2.6e-35	0.17	2.1e-35	3333.19	0.59	0.03	-0.001

Table 8.1: Summary of the fit result for bremsstrahlung analysis.

on the nuclear recoil is shown in the Fig. 8.7. The lower mass end, 4 GeV, was chosen which have nuclear recoil signal more than 1 keVnr even in December. The higher mass end, 20 GeV, was chosen which is same with previous modulation analysis by XMASS [29]. Table 8.2 shows the numerical results. All pull terms for data efficiency, single rate effect, and signal estimation at best fit are locating within 1σ .

WIMP mass[GeV]	best fit $\sigma[\text{cm}^2]$	p-value	90%C.L. $\sigma[\text{cm}^2]$	χ^2	α	γ	β_1	β_2
4	-3.2e-40	0.17	6.6e-39	3367.54	0.62	0.48	0.08	0.006
5	-3.9e-41	0.16	1.9e-40	3367.48	0.62	0.48	0.07	0.005
6	-1.3e-41	0.15	2.3e-41	3367.34	0.62	0.49	0.04	0.007
7	-6.3e-42	0.12	6.4e-42	3367.10	0.62	0.49	0.03	0.009
8	-3.8e-42	0.11	2.9e-42	3366.80	0.61	0.49	0.03	0.009
9	-2.6e-42	0.09	1.6e-42	3366.50	0.61	0.48	0.03	0.005
10	-1.9e-42	0.09	1.1e-42	3366.28	0.60	0.47	0.00	-0.004
12	-1.1e-42	0.08	5.7e-43	3366.20	0.59	0.44	-0.01	-0.007
14	-7.2e-43	0.10	3.8e-43	3366.61	0.59	0.42	-0.06	-0.018
16	-4.7e-43	0.16	3.3e-43	3367.33	0.59	0.40	-0.07	-0.018
18	-2.9e-43	0.25	2.8e-43	3368.09	0.59	0.39	-0.08	-0.017
20	-1.7e-43	0.42	2.6e-43	3368.71	0.60	0.38	-0.08	-0.013

Table 8.2: Summary of the fit result for nuclear recoil analysis.

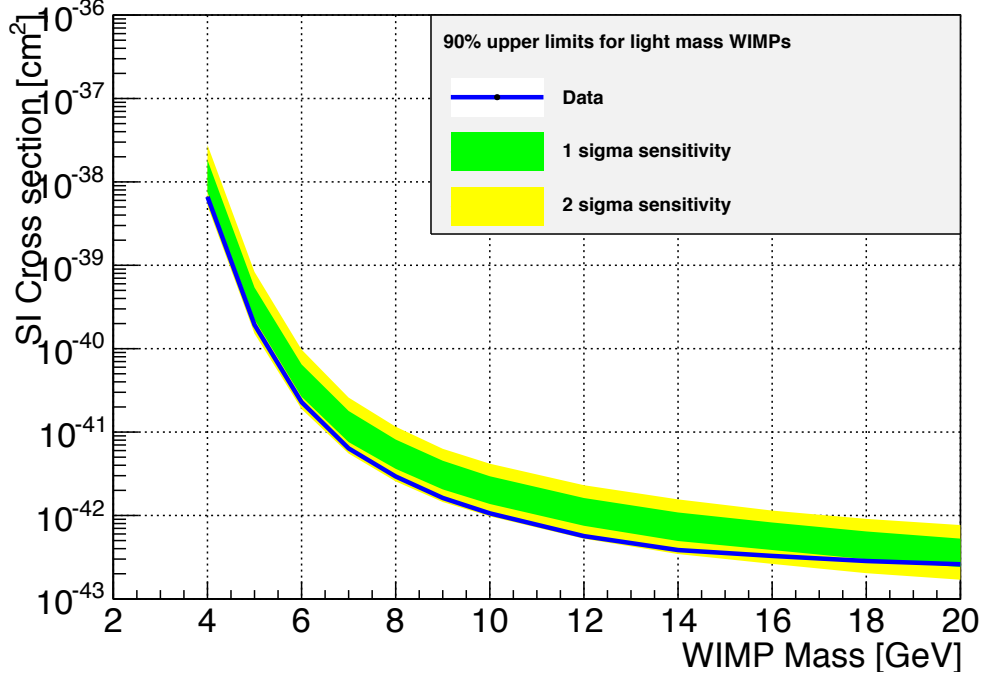


Figure 8.7: 90 % C.L. upper limits of Data and the sensitivity band for null amplitude utilizing the nuclear recoil.

8.3 Result of the Model-independent modulation search

The distributions of data and the best fit function for each energy are shown in Fig. 8.8 - 8.11. The result of the model-independent modulation search is shown in the Fig. 8.12. The lower horizontal axis is the energy of an electron, upper horizontal axis is the energy of a nuclear recoil, and the vertical axis is the amplitude of the fitted result. The blue boxes are showing the range of ± 1 and $\pm 2 \sigma$ from null amplitude samples for each energy. The amplitude is obtained by correcting with the signal efficiency calculated based on the electron MC shown in Fig. 8.13. The efficiency for energy bin i is calculated as

$$\frac{\text{Number of entries after all reduction in } i \text{ th energy bin}}{\text{Number of entries with at least 1 hit in } i \text{ th energy bin}}. \quad (8.3)$$

Only the result more than 1 keVee is shown, because of the accuracy of the energy scale for electron discussed in Sec. 4.4. As the result, p-value of the

data for null amplitude hypothesis is 0.34. No significant amplitude was seen from the data.

8.3.1 Comparison with the result of WIMP analysis and model independent analysis

In the Fig. 8.14, observed amplitude for each energy bin without the correction of efficiency is shown. The red line in the figure is showing the 0.4 GeV WIMP signal with the best fit cross section, which is $1.1 \times 10^{-32} \text{cm}^2$. As this figure shows, two results are consistent with error bar of model independent amplitude for each energy bin.

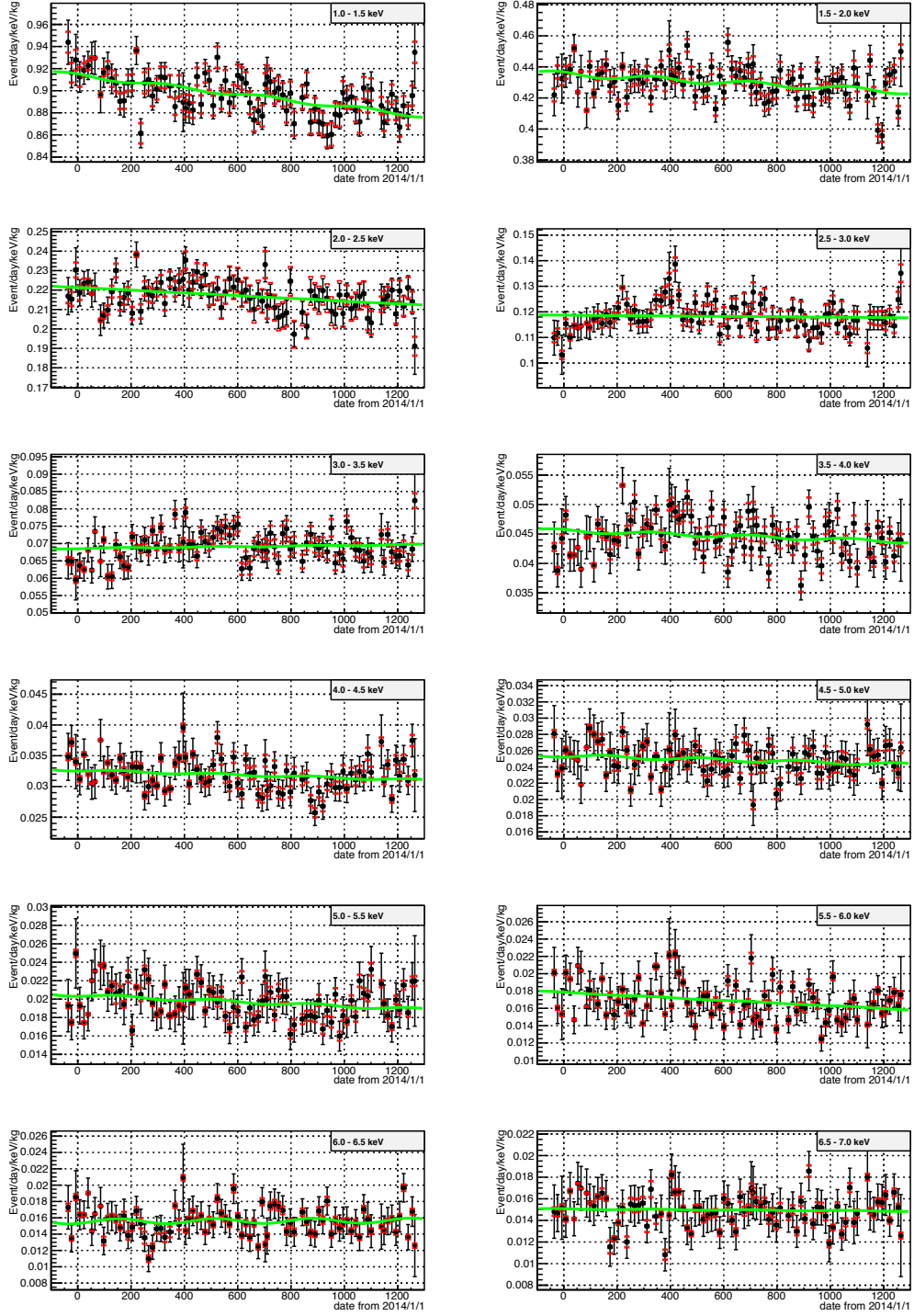


Figure 8.8: Distribution of data with correction of efficiency for each energies. Green line is the best fit for model independent analysis.

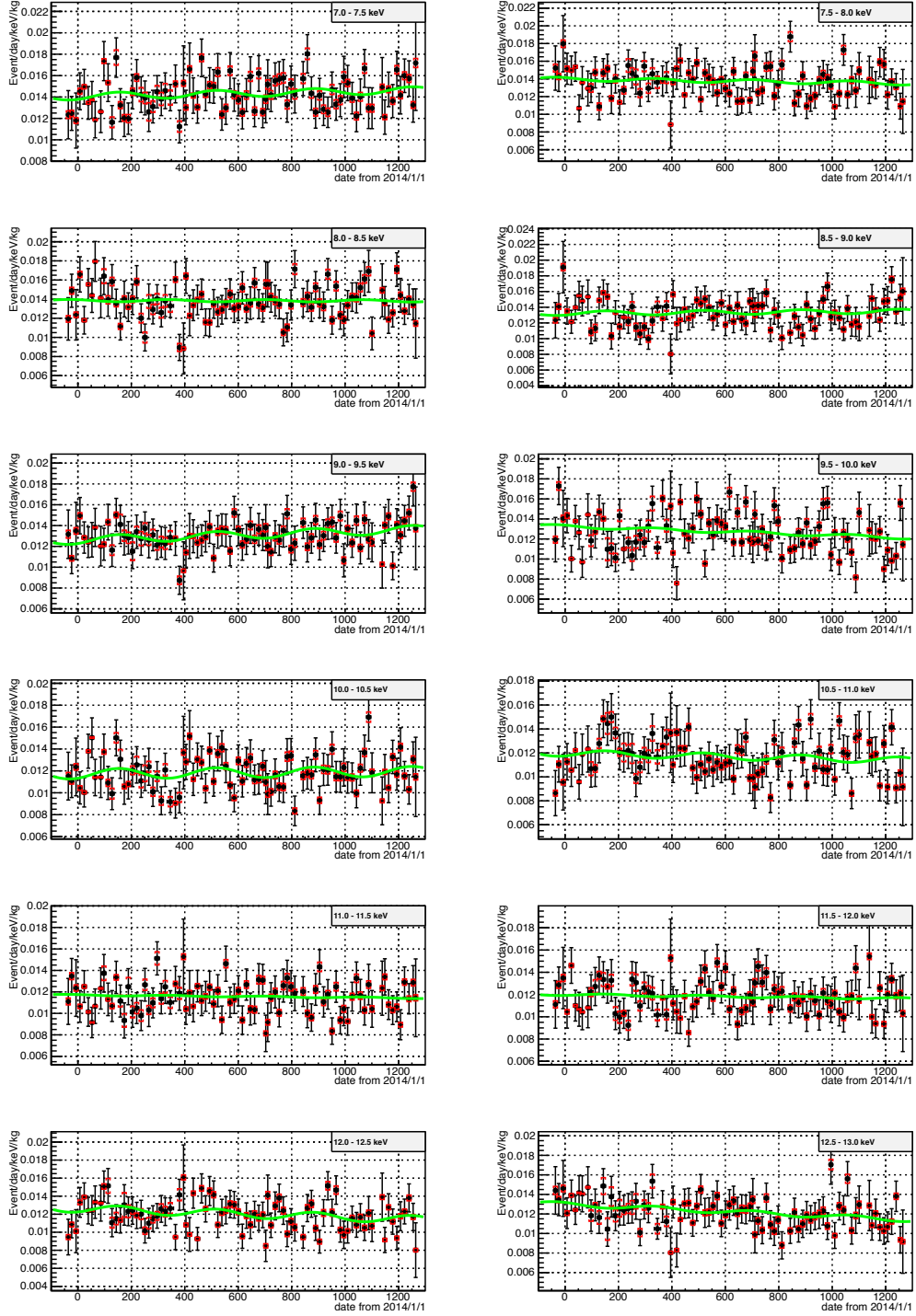


Figure 8.9: Distribution of data with correction of efficiency for each energies. Green line is the best fit for model independent analysis.

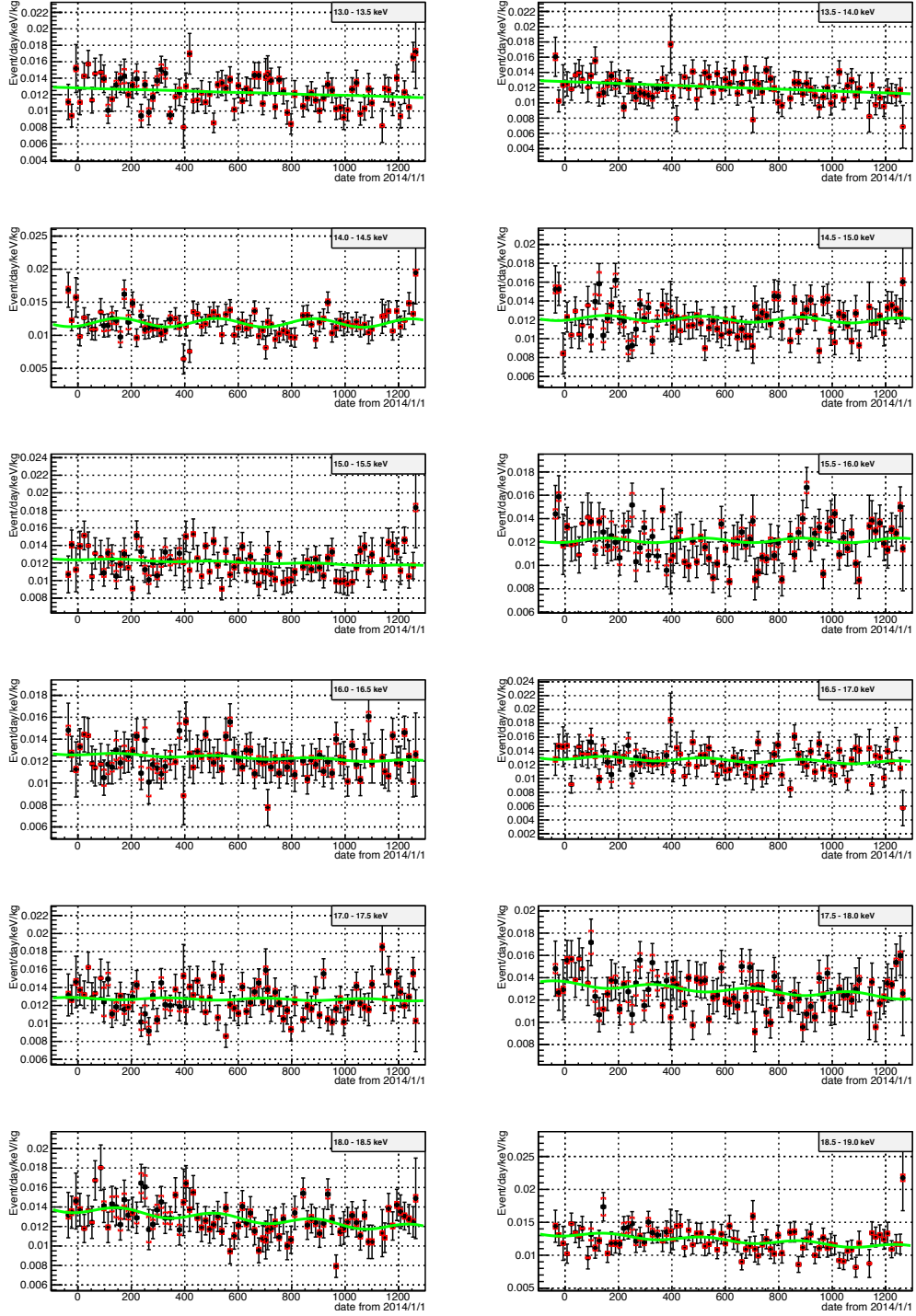


Figure 8.10: Distribution of data with correction of efficiency for each energies. Green line is the best fit for model independent analysis.

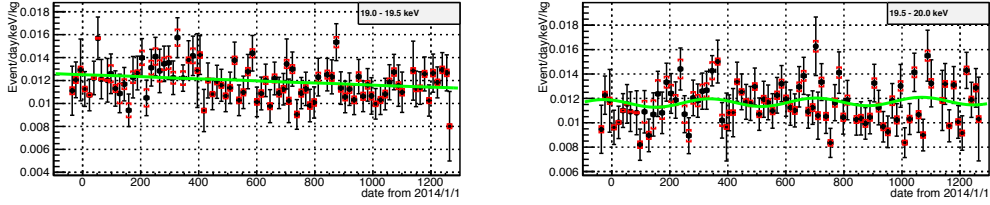


Figure 8.11: Distribution of data with correction of efficiency for each energies. Green line is the best fit for model independent analysis.

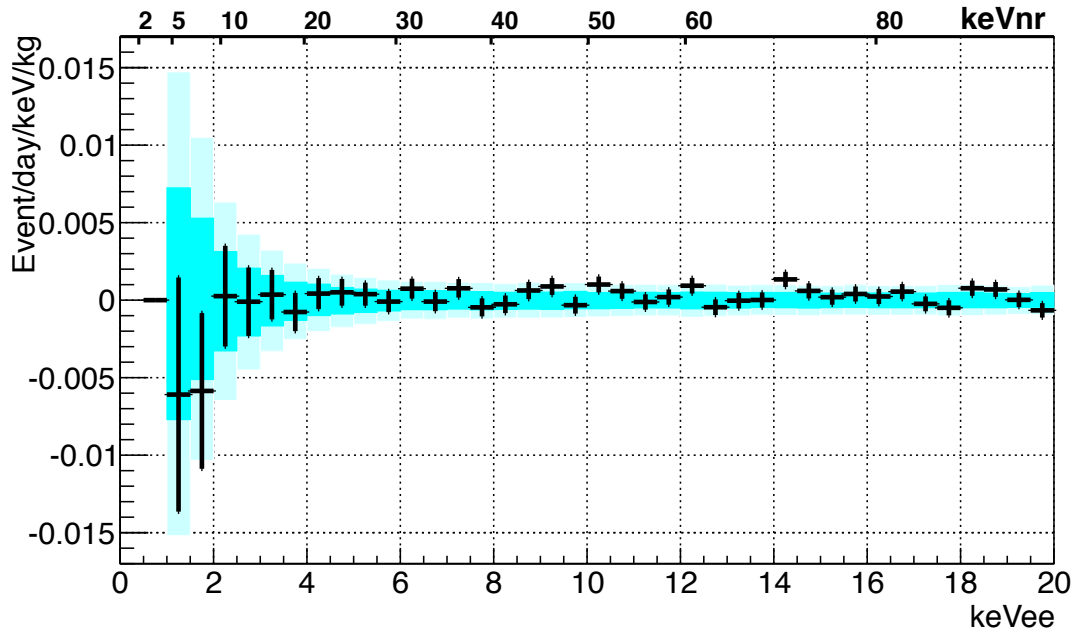


Figure 8.12: Result of the model independent analysis. Black points are amplitude from data. Bottom energy scale is showing the electron recoil energy, upper energy scale is showing the nuclear recoil energy. Cyan boxes are showing the ± 1 , $\pm 2 \sigma$ sensitivity from null amplitude dummy samples.

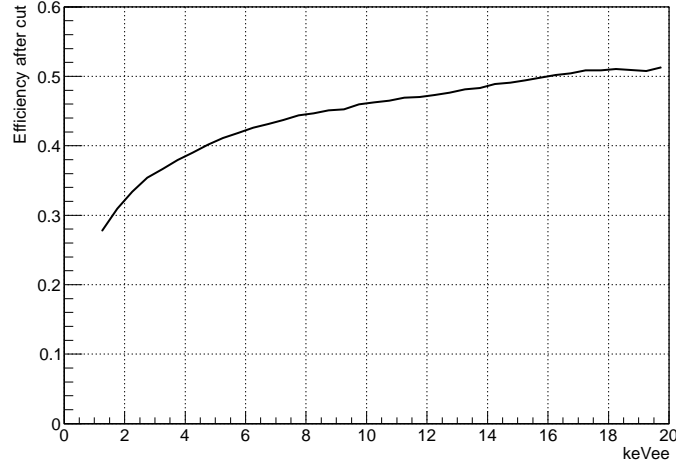


Figure 8.13: Efficiency curve for signal evaluated by uniform electron MC

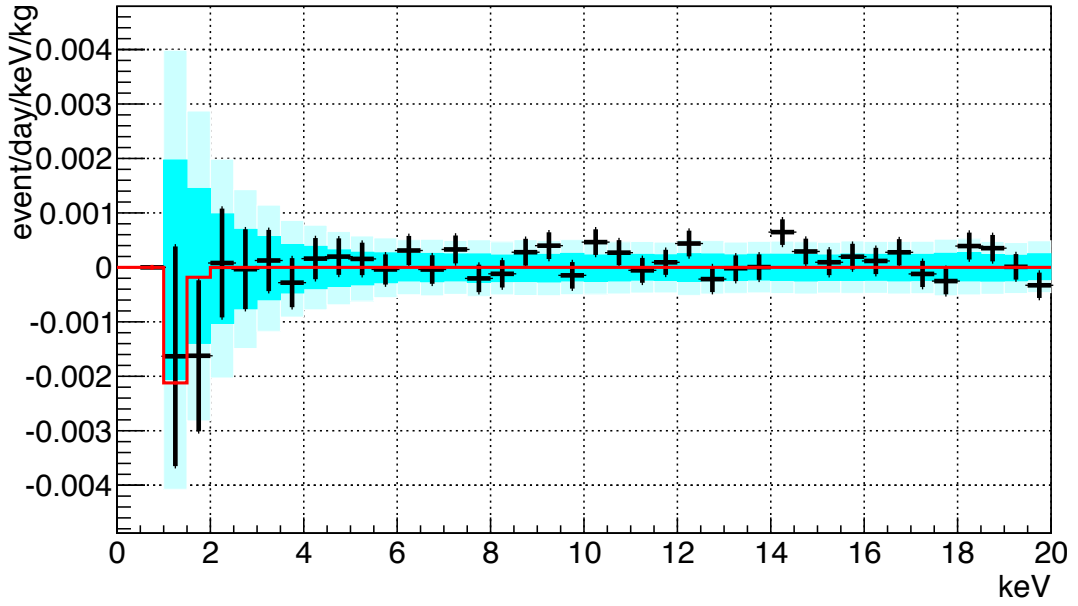


Figure 8.14: Comparison of the model independent result and bremsstrahlung analysis. Black points are the result of model independent analysis. Cyan boxes are $\pm 1, 2\sigma$ sensitivity from dummy samples. Red line is the result of bremsstrahlung analysis.

Chapter 9

Conclusion

9.1 Summary of the results of the WIMPs search

The unique feature of this study is the first experimental test for sub-GeV WIMPs using annual modulation and bremsstrahlung in a liquid xenon detector. It is pointed out that even small energy of nuclear recoil leads electron recoil signals through bremsstrahlung of a γ ray [33]. Since the spectrum of this bremsstrahlung emission relies on the relative velocity of dark matter to the detector, annual modulation of the spectrum can be obtained based on the earth's revolution. The analysis using the bremsstrahlung effect enabled us to perform the investigation of Sub-GeV WIMPs by liquid xenon detector. This is the first time to calculate the annual modulation of the bremsstrahlung spectrum, and obtain the result for WIMPs based on the bremsstrahlung effect experimentally. Previously, in the region of sub-GeV, WIMPs has been searched for by using low temperature bolometers. From this study, the WIMPs cross section to an nucleon at 0.4 GeV was constrained lower than $1.6 \times 10^{-32} \text{ cm}^2$ at 90% confidence level upper limit. The considerable candidate of remaining BG is mainly RIs contained in the alminum seal of PMTs, especially ^{238}U and ^{210}Pb , discussed in Sec. 3.4.1. The uncertainty of the shape of alminum seal is taken into account as discussed in Sec. 6.1.1. In Fig. 9.1, time variation of the data and expected signal of 0.5 GeV WIMPs with $3 \times 10^{-32} \text{ cm}^2$ cross section is shown.

In addition to the result for bremsstrahlung effect, WIMPs with mass of 4-20 GeV are searched for with lower threshold (2.3 keVnr) than previous

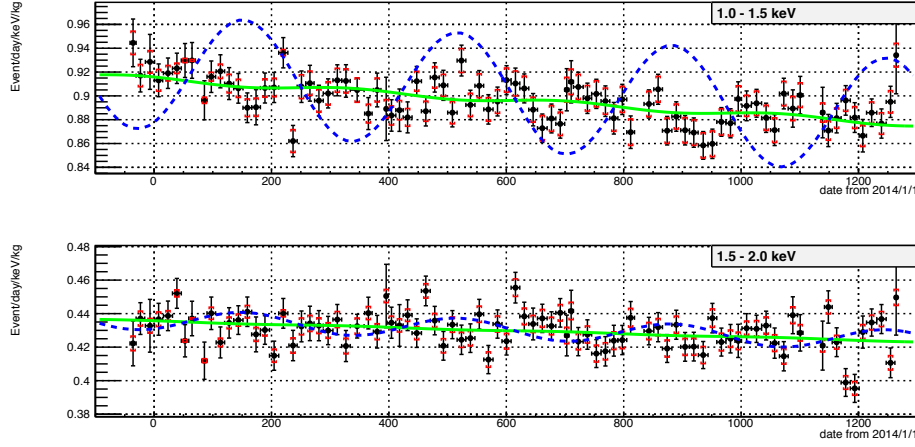


Figure 9.1: Time variation for 0.5 GeV WIMPs. 1.0-1.5 and 1.5-2.0 keV are shown. Black points are data, red brackets are size systematical error added by quadrature. Green and Blue curves are the best fit and $3 \times 10^{-32} \text{ cm}^2$ for 0.5 GeV WIMPs.

analysis (4.8 keVnr). The data with three hit coincidence are used, and the effect of systematics, especially the weak flasher effect, is understood. From this study, the WIMPs cross section to a nucleon at 8 GeV was constrained lower than $2.9 \times 10^{-42} \text{ cm}^2$ at 90% confidence level upper limit. In Fig. 9.2, time variation of the data and expected signal of 8 GeV WIMPs with $8 \times 10^{-41} \text{ cm}^2$ cross section is shown.

In Fig. 9.3, the summary of the result for the WIMPs searches in this thesis is shown. Lines in Fig. 9.3 are results from other experiments based on their analysis. Some of theorists are calculating the upper limits using the published data of experiments [33]. Brown line is CRESST sapphire surface detector [23], orange line is CRESST-II [11], green line is DAMIC [24]; These experiments are using crystals and achieved the low threshold. They are observing the nuclear recoil signal caused by WIMPs, not bremsstrahlung effect. Cyan line is CDMSLite [27], and blue line is SuperCDMS [12]. These experiments are using semi conductor such as Ge or Si. Blue purple line is LUX [17], dark green line is XENON1T [16], gray line is PANDAX [31]. They are dual-phase LXe detector, with nuclear recoil PSD. Magenta line is showing the previous analysis by XMASS [29]. For two hatched regions, brown region is DAMA/LIBRA [10, 25, 26] and gray region is CDMS-Si [28]. DAMA/LIBRA is the experiment with NaI(Tl) crystal. CDMS-Si is using Si semiconductor for its detector.

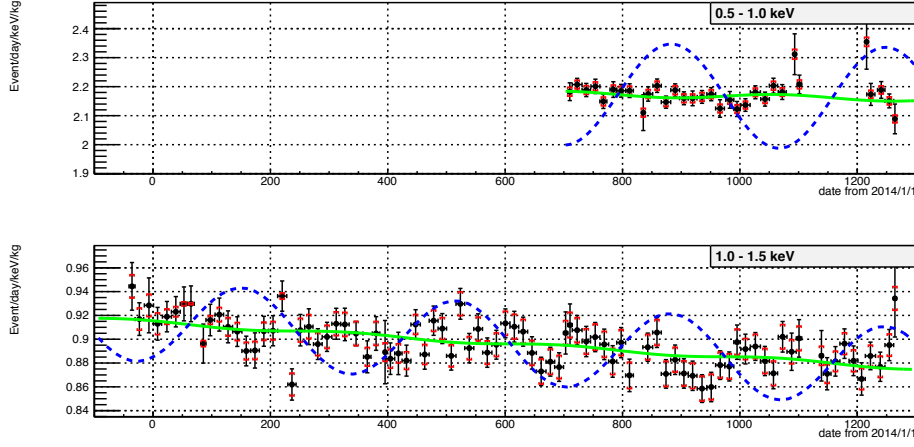


Figure 9.2: Time variations for 8 GeV WIMPs in 0.5 - 1.0 and 1.0-1.5 keV are shown. Black points are data, red brackets are size systematic error added by quadrature. Green and Blue curves are the best fit and $8 \times 10^{-40} \text{ cm}^2$ for 8 GeV WIMPs, which is the upper edge of CDMS-Si region.

9.2 Discussion for future analysis

In this analysis, about 3.5 years of normal threshold data is used. In the case of low threshold data, 1.5 years of data are used. Larger exposure makes it possible to search for sub-GeV WIMPs dark matter with higher sensitivity. In this thesis, sub-GeV region of WIMPs are searched for by annual modulation considering the bremsstrahlung effect. Recently the Migdal effect is suggested to be utilized [55]. This is another interesting effect introducing strong enhancements of WIMP search in the sub-GeV mass range. In the Migdal effect, a shell electron is emitted through the inelastic scattering, and then characteristic X-ray, or Auger electrons are emitted from the remaining holes in the shell. The energy of K-shell X ray is around 30 keV, and that of L-shell is around 4 keV. This enables us to search for sub-GeV WIMPs with better sensitivity. Similar analysis developed in this thesis is useful for the search.

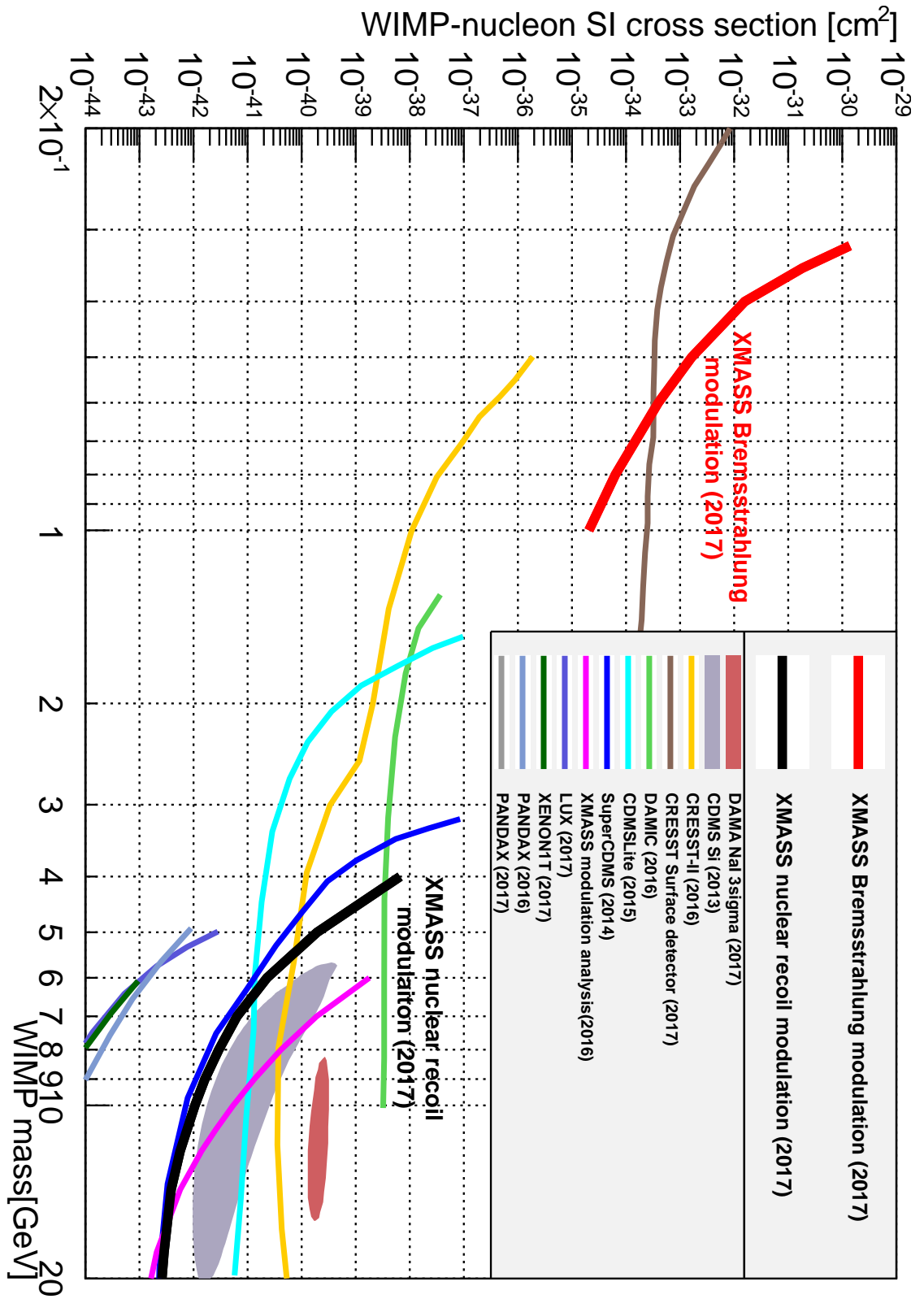


Figure 9.3: Summary of WIMP searches. Both of searches utilizing bremsstrahlung effect and nuclear recoils are shown.

Bibliography

- [1] F. Zwicky, *Helv. Phys. Acta.*, 6, 110-127 (1933).
- [2] F. Zwicky, *ApJ*, 86 (1937) 217.
- [3] K. G. Begeman, A. H. Broeils and R. H. Sanders, *Mon. Not. Roy. D, Aston. Soc.*, 249, 523 (1991).
- [4] <http://hubblesite.org/gallery/album/pr2001032b/>.
- [5] <http://chandra.harvard.edu/photo/2006/1e0657/>.
- [6] Planck collaboration, *A&A*, 571, A1, (2014).
- [7] V. Springel et al. *Nature*, 435, 629636, (2005).
- [8] C. Alcock et al. (The MACHO collaboration), *ApJ.*, 542, (2000), 281-307.
- [9] P. Tisserand et al., *Astron. Astrophys.*, 469:387-404, (2007).
- [10] R. Bernabei et al., *Eur. Phys. J. C*, 56:333-355, (2008).
- [11] G. Angloher et al. (The CRESST collaboration), *Eur. Phys. J. C*, (2016), 76:25.
- [12] R. Agnese et al. (The SuperCDMS collaboration), *Phys. Rev. Lett.*, 112, 241302 (2014).
- [13] P. A. Amaudruz et al. (The DEAP collaboration), *arXiv:1707.08042*.
- [14] P. Agnes et al., *Phys. Lett. B*, 743, 456 (2015).
- [15] K. Abe et al. (The XMASS collaboration), *Nucl. Instr. and Meth. in Phys. Res. A*, 716, (2013), 78-85.

- [16] E. Aprile et al. (The XENON collaboration), Phys. Rev. Lett., 119, 181301, (2017).
- [17] D. S. Akerib et al. (The LUX collaboration) Phys. Rev. Lett., 118, 021303, (2017).
- [18] A. Tan et al. (The PandaX-II collaboration), Phys. Rev. Lett., 119, 181302 (2017).
- [19] ATLAS collaboration, J. High Energy Phys., 01, (2016), 172. K.
- [20] CMS collaboration, J. High Energy Phys., 02, (2017), 135. K.
- [21] O. Adriani et al., Phys. Rev. Lett., 111, 081102, (2013).
- [22] K. Choi et al. (The Super-Kamiokande collaboration), Phys. Rev. Lett., 114, 141301, (2015).
- [23] G. Angloher et al. (The CRESST collaboration), Eur. Phys. J. C, (2017), 77:637.
- [24] A. Aguilar-Arevalo et al. (The DAMIC collaboration), Phys. Rev. D, 94, 082006.
- [25] R. Bernabei et al., Eur. Phys. J. C, 73, (2013), 2648.
- [26] J. Kopp et al., JCAP, 03, (2012), 001.
- [27] R. Agnese et al. (The SuperCDMS collaboration), Phys. Rev. Lett., 116, 071301, (2016).
- [28] R. Agnese et al. (The CDMS collaboration), Phys. Rev. Lett., 111, 251301, (2013).
- [29] K. Abe et al. (The XMASS collaboration), Phys. Lett. B, 759, (2016), 272-276.
- [30] K. Abe et al. (The XMASS collaboration), In preparation.
- [31] A. Tan et al. (The PandaX-II collaboration), Phys. Rev. Lett., 117, 121303, (2016).
- [32] J. D. Lewin and P. F. Smith, Astroparticle Phys., 6, (1996), 87.

- [33] Chris Kouvaris and Josef Pradler, Phys. Rev. Lett., 118, 031803, (2017).
- [34] "Classical electrodynamics 3rd edition", written by J. D. Jackson, translated by M. Nishida.
- [35] <https://physics.nist.gov/PhysRefData/Xcom/html/xcom1.html>.
- [36] E. Aprile et al. (The XENON collaboration), Phys. Rev. Lett., 107, 131302.
- [37] E. Aprile et al. (The XENON collaboration), Phys. Rev. Lett., 115, (2015), 091302.
- [38] E. Aprile et al. (The XENON collaboration), Science, 349, 6250, (2015), 851.
- [39] E. Aprile et al. (The XENON collaboration), Phys. Rev. Lett., 118, (2017), 101101E.
- [40] Laura Baudis et al., Phys. Rev. D, 87:115015, (2013).
- [41] E. Aprile et al. (The XENON collaboration), Phys. Rev. Lett., 107, 131302, (2011).
- [42] Super-Kamiokande official homepage, <http://www-sk.icrr.u-tokyo.ac.jp/sk/>.
- [43] A.Hitachi and T. Takahashi, Phys. Rev. B, 27, (1983), 5279.
- [44] S. Kubota, M. Hishida, J. Raun, J. Phys. C., 11, (1978), 2645.
- [45] Kota Ueshima, PhD Thesis, University of Tokyo.
- [46] K. Kobayashi, the 69th annual meeting of Japan physical society, March, 2014, 30aTE-6.
- [47] <http://www.caen.it/csite/HomePage.jsp>.
- [48] N.Y. Kim et al. (The XMASS collaboration), Nucl. Instr. and Meth. in Phys. Res., A784, (2015), 499-503.
- [49] D.S. Akerib et al. (The LUX collaboration), arXiv:1608.05381.

- [50] H. Uchida, the 67th annual meeting of Japan physical society, March, 2012, 27aGK-4.
- [51] K. Abe et al. (The XMASS collaboration), In preparation.
- [52] H.Takiya et al. (The XMASS collaboration), Nucl. Instrum. Meth.A, 834, (2016), 192-196.
- [53] E.J. Jeon and Y.D.Kim., Astropart. Phys., 73:2833, (2016).
- [54] Y. Onishi, Master thesis, Kobe University, (2015).
- [55] M. Ibe et al., arXiv:1707.07258.